UT-BATTELLE
Oak Ridge National Laboratory

ORNL/TM-2013/555

Fusion Materials Research at Oak Ridge National Laboratory

Progress during Fiscal Year 2013
October 1, 2012 through September 30, 2013

Compiled by:

F.W. Wiffen
L.L. Snead
E.B. Mecherle

November 2013

OAK RIDGE National Laboratory

U.S. DEPARTMENT OF ENERGY

Materials Science and Technology Division

Fusion Materials Research at Oak Ridge National Laboratory
Progress during Fiscal Year 2013
October 1, 2012 through September 30, 2013

Compiled by:

F.W. Wiffen
L.L. Snead
E.B. Mecherle

November 2013

Prepared by
OAK RIDGE NATIONAL LABORATORY
Oak Ridge, Tennessee 37831-6283
managed by
UT-BATTELLE, LLC
for the
U.S. DEPARTMENT OF ENERGY
under contract DE-AC05-00OR22725

CONTENTS

LIST OF FIGURES

LIST OF TABLES

1.0 INTRODUCTION

Lance Snead (sneadll@ornl.gov), Yutai Katoh, and Bill Wiffen

The realization of fusion energy is a formidable challenge with significant achievements resulting from close integration of the plasma physics and applied technology disciplines. Presently, the most significant technological challenge for the near-term experiments such as ITER, and next generation of fusion power systems, is the inability of current materials and systems to withstand the harsh fusion nuclear environment. The overarching goal of the ORNL fusion materials program is to provide the applied materials science support and understanding to underpin the ongoing DOE Office of Science fusion energy program while developing materials for fusion power systems. In doing so the program must be integrated both with the larger U.S. and international fusion materials communities, and with the international fusion design and technology communities. The overall ORNL program on materials development continues to actively develop low activation structural materials such as the Reduced Activation Ferritic/Martensitic Steels, the higher strength/higher creep resistance Nano Composted Ferritic steels, and Silicon Carbide Composites. A significant change over the past two years is the increased emphasis on high heat flux testing and the development of refractory metals. This includes the use of an ORNL Plasma Arc Lamp facility adapted for the thermal testing of irradiated materials, the development and evaluation of new tungsten materials, and the study and understanding of the irradiation performance of tungsten through coupled modeling and experiment. In each case the materials are being developed in a design-informed fashion where properties improvements are led by the latest fusion-relevant designs and directed at advancing the Technology Readiness Level of the materials systems. A limited effort within the ORNL program is directed towards diagnostic materials and high-temperature superconductors. In the area of diagnostics, ORNL continues to develop irradiation-hardened dielectric mirrors and to support basic irradiation materials science of ceramics for diagnostic systems. For high-temperature superconductors the ORNL program has undertaken a limited program to quantify the irradiation sensitivity of the most recently developed tape materials. Finally, this work scope integrates fundamental modeling into the development efforts as much as practicable.

This program makes heavy reliance on neutron irradiation in HFIR, the High Flux Isotope Reactor at ORNL. This is complemented by use of the newly commissioned ORNL-University of Tennessee ion irradiation facility when that facility is better suited to explore fundamental aspects of materials behavior under irradiation. In the longer term, we are looking forward to using the proposed FMITS facility that will allow irradiation in the neutron field on the ORNL Spallation Neutron Source.

This document provides a summary of FY-13 activities supporting the Office of Science, Office of Fusion Energy Sciences Materials Research for MFE (AT-60-20-10-0) carried out by the Oak Ridge National Laboratory. The organization of this report is mainly by material type, and then with sections on specific technical activities. The four projects selected in the Funding Opportunity Announcement solicitation of late 2011 and first funded in late FY 2012 are identified by "FOA" in the titles. A new activity, "Materials Engineering in Support of the ARIES Program," is reported in Chapter 10.0. The fusion materials effort consists of a wide array of tasks and collaborations both within the US and with international partners. The major continuing international collaborating partners include the Japan Atomic Energy Agency (the US-JAEA collaboration), the Japanese National Institute for Fusion Sciences (the TITAN/PHENIX collaboration) and the Karlsruhe Institute of Technology in Germany. The later collaboration, now in its second year, focuses on high heat flux materials and refractory metals.

Milestones for the ORNL program were listed in the five FWPs for the program. All 18 milestones, listed in Table 1, were completed as scheduled.

Table 1. FY 2013 Milestones from ORNL Fusion Materials Program FWPs

ERAT725 – Base Program	**month/y**	**PI**
1. Complete PIE of 10 dpa silicon carbide irradiation creep experiment	3/13	Katoh
2. Complete initial mechanical characterization unirradiated RAFMS	4/13	Byun
3. Demonstrate fabrication graded tungsten-to-steel transition structure by e-beam AM.	6/13	Ohriner
4. Complete optical property measurement of high dose irradiated dielectric mirrors	6/13	Leonard
5. Publish the atomistic-based equation of state for helium in iron	7/13	Stoller
6. Complete one high-heat flux test of irradiated tungsten specimen using the PAL	9/13	Sabau
7. Complete evaluation of effects of first round irradiation of Hi T superconductors	9/13	Leonard
8. Complete construction first FS thermal convection loop for Pb-Li compatibility testing	9/13	Pint
9. Carry out preliminary expt. verification strengthening mechanisms in NCF alloys	9/13	Stoller
10. Start HFIR irradiation of new high dose SiC/SiC rabbit experiments	9/13	Katoh
11. With PHENIX, develop thermo-fluid/thermo-stress model for component test in PAL	9/13	Katoh/ Sabau
12. Develop materials engineering approach to support ARIES lifetime component design	9/13	Snead/ Rowcliffe
ERAT752 – FOA – Friction Stir Welding		
13. Develop baseline FSW processes to produce defect free joints of ODS/NFAs alloys	9/13	Feng
ERAT754 – FOA – Unique Materials		
14. Complete fab. & characterize bulk metallic glass, high-entropy alloy, and MAX-phase	4/13	Zinkle
15. Initiate ion beam and HFIR neutron irradiation experiments	6/13	Zinkle
16. Report initial results on radiation stability of three materials systems	11/13	Zinkle
ERAT762 – FOA – SiC Joining		
17. Report on current status and prospects of joining technology development for SiC	6/13	Katoh
ERAT763 – FOA – High Cr ODS Alloys		
18. Produce candidate heats Al, Zr containing ODS alloys and high-Cr reference alloy	9/13	Pint

2.0 FUSION MATERIAL IRRADIATION TEST FACILITY (FMITS) AT SNS

Mark Wendel (wendelmw@ornl.gov) and Phil Ferguson

SUMMARY

The Fusion Materials Irradiation Test Station (FMITS) is a design concept (completed in FY 2012) for installation at the Spallation Neutron Source (SNS) Facility. This previously completed design study showed that the first SNS high-energy irradiations on fusion materials specimens could occur in less than 3 years at a cost of $10 M. Follow-on experiments would have costs similar to HFIR in-core experiments.

PROJECT DESCRIPTION

Fusion materials program samples would be located in the SNS target zone within two horizontal tubes in front of the mercury target. For these specimen locations, the back-scattering neutron flux spectra will be close to the ITER fusion spectrum. The PKA spectra at the FMITS samples were also compared to those for ITER, and the results show good agreement. Damage rates will be 1.6–5.5 dpa/y for steel, and 1.8–3.4 dpa/y for SiC, with the desirable feature that the helium-to-dpa production ratios are close to those expected in D-T fusion. Figure 1 compares calculated FMITS materials response rates to other facilities used by the fusion materials program.

The test station will be water-cooled with a variable inert-gas blanket for temperature control. Thermal analysis shows that the sample temperatures can be maintained at 600°C or higher even if average beam power varies by 50%. The FMITS assembly is designed to be installed over a target module and can be reused with multiple targets.

A reliable target at SNS is a prerequisite for the development and deployment of FMITS.
The SNS run cycle was interrupted by two premature target failures in the fall of 2012. These issues were studied and identified as inadequate weld penetration on the same weld seam on both targets. A new target without the weld defect has operated successfully for more than 3700 MW-h, a record for the SNS. Nine more targets are in the process of fabrication as confidence in the target design has increased. The accelerator was briefly operated at 1.4 MW for the first time just after midnight on September 29, 2013 as a demonstration immediately prior to a scheduled outage and target change-out.

Funding for the conceptual design of the FMITS was received late in the fiscal year, and the first planning meetings to initiate this work were held in September. The main deliverables of this one-year activity are:

- Conceptual Design Report
- Conceptual Design Review
- Safety Assessment

The plan going forward is to develop the FMITS design and remote handling logistics so that it will be smoothly integrated with neutron science activities performed at the SNS. The Safety Assessment will define in detail the risks and consequences of the FMITS at SNS. By including potential users in the design process, the benefit of FMITS to fusion materials research will also be increased. Finally, a cost estimate with reduced contingency will be produced and delivered at the Conceptual Design Review.

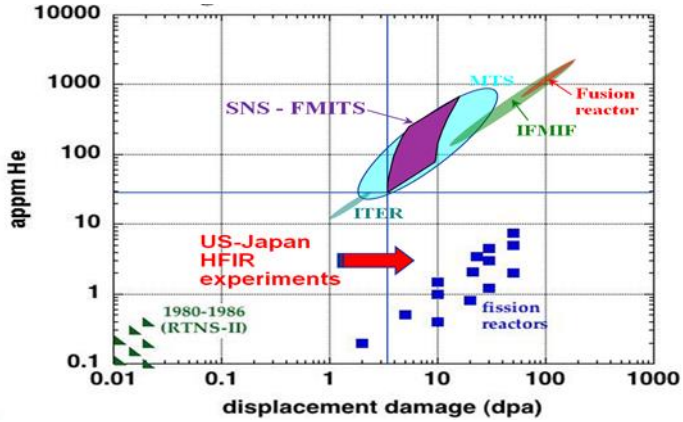

Figure 1. Comparison of the 2-4 year helium and displacement damage levels for ferritic steels in candidate irradiation facilities.

3.0 FOA - STRUCTURAL MATERIALS WITH POTENTIALLY UNIQUE IRRADIATION RESISTANCE

S.J. Zinkle (zinklesj@ornl.gov), A.G. Perez-Bergquist, N.A.P. Kiran Kumar, H. Bei, Y. Katoh, K.J. Leonard and Yanwen Zhang

OBJECTIVES AND BACKGROUND

This project is exploring the basic radiation resistance of three unique classes of structural materials that may have the potential for very good resistance to neutron-induced property degradation: high entropy alloys (HEAs), bulk metallic glasses (BMGs), and MAX phase ceramic materials.

SUMMARY

A new initiative is addressing the baseline properties, including the effects of ion and neutron irradiation, of novel materials that may potentially possess exceptional radiation tolerance. The materials for this investigation include bulk metallic glasses, crystalline high configurational entropy alloys, and MAX phase ceramics including polycrystalline Ti_3SiC_2 and Ti_2AlC ceramics. Microstructural and mechanical property characterization of the unirradiated materials was completed, and a series of scoping ion irradiations were performed on the BMG and HEA materials near room temperature and at elevated temperatures. Companion neutron irradiations have been completed for all three classes of materials and will be characterized in FY14.

EXPERIMENTAL

A single FCC phase high entropy alloy of composition 27%Fe-27%Mn-28%Ni-18%Cr, and a bulk metallic glass, BAM-11, of composition Zr-17.9%Cu-14.6%Ni-10%Al-5%Ti, both manufactured at ORNL, were chosen for the present study. HEA samples were ion irradiated with 3 MeV Ni ions to fluences of 4.2×10^{13}, 4.2×10^{14} and 4.2×10^{15} ions/cm^2 (0.1, 1.0 and 10 dpa at a depth of 1.07 μm) at room temperature and 500°C in the newly commissioned ORNL/University of Tennessee ion beam laboratory. BMG samples were ion irradiated to 0.1 and 1.0 dpa at room temperature and 200°C. Hardness examination using an MTS XP nanoindenter and detailed microstructural characterization using scanning electron microscopy (SEM) and transmission electron microscopy (TEM) have been performed on both unirradiated and irradiated specimens.

SUMMARY OF RESULTS

High entropy alloys

The hardness in the ion irradiated region of the HEA samples increased rapidly with increasing dose at room temperature, from ~40% higher than the unirradiated value at 0.1 dpa to approximately double the unirradiated hardness at 1 dpa. The increase in the irradiated hardness was less pronounced for irradiations at 500°C, with values of 15-20% increase at 1 dpa and ~20% increase at 10 dpa. Radiation induced microstructures were made up of network dislocations, dislocation loops and unresolved "dark spot" defect clusters. The loop density increases with dose and saturates after 1 dpa irradiation (see Table 2). Small defect clusters after room temperature irradiation and larger defect clusters after 500°C irradiation were observed. Voids, which are one of the major concerns in conventional Fe-Ni-Cr alloy, were not observed in present HEA at any irradiation condition.

The grain boundary composition of the HEA specimens subjected to high temperature irradiation was altered due to radiation-induced segregation. Evidence of significant solute segregation (Cr and Mn enrichment) was observed at grain boundaries and discrete precipitates were observed. However,

precipitation was not observed in the room temperature irradiated samples. The grain bound precipitates were enriched in Cr and Mn and depleted in Fe and Ni. In addition, as the radiation dose increases, the chromium and manganese becomes more enriched and the iron and nickel become progressively more depleted along the grain boundary. Overall, the behavior of the high entropy alloy following irradiation at 500°C appears to be significantly different from the behavior observed in irradiated Fe-Cr-Ni austenitic alloys.

Table 2. Dislocation loop density of ion irradiated HEA

Ion irradiation condition	Dislocation loop density (m^{-3})
0.1 dpa, RT	0.7×10^{23}
1 dpa, RT	4.7×10^{23}
1 dpa, 500°C	4.4×10^{23}
10 dpa, 500°C	5.6×10^{23}

Bulk Metallic Glasses

Nanoindentation results (Table 3) show hardness in the ion irradiated region of the BMG samples decreased by about 12% due to irradiation at room temperature to 0.1 and 1 dpa, but remained roughly unchanged following irradiation at 200°C. The elastic modulus of the irradiated samples decreased by ~7% for irradiation at room temperature, but actually increased by ~1% and ~4%, respectively, due to irradiation at 200°C to 0.1 and 1 dpa. TEM examination of the irradiated BMG samples displayed displacement damage-free, fully amorphous material with no evidence of recrystallization (Fig. 2). Fast Fourier Transform, FFT, analysis indicated a small amount of densification following irradiation, however. These results suggest that BAM-11 BMG may have uses in irradiation environments, especially in situations at elevated temperatures below the glass transition temperature, T_g. Further investigation of irradiated samples at higher dose is planned.

Table 3. Summary of nanoindentation results on BAM-11 specimens

	Unirrad	0.1 dpa, RT	1 dpa, RT	0.1 dpa, 200°C	1 dpa, 200°C
Avg. Hardness* (GPa)	6.6	5.8	5.7	6.4	6.7
Std. Dev. Of Hardness (GPa)	0.6	0.4	0.2	0.9	0.7
Avg. Young's Modulus* (GPa)	101.8	95.3	94.3	102.7	106.4
Young's Mod. Std. Dev. (GPa)	4.6	4.0	2.8	9.9	5.9

* At depth of 200 nm

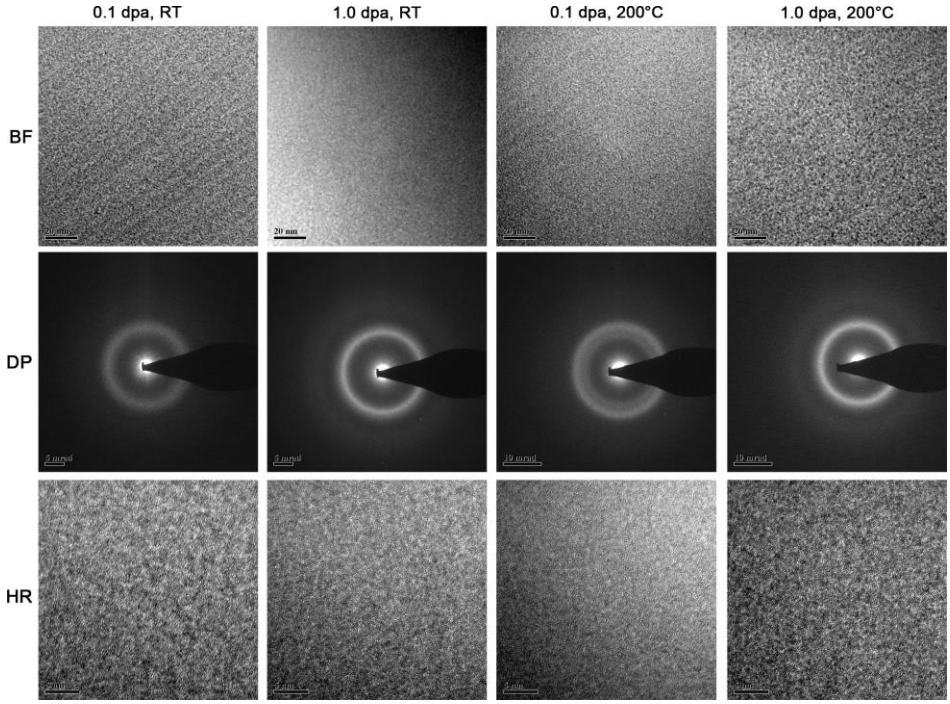

Figure 2. TEM bright field images, diffraction patterns, and high-resolution images of irradiated BAM-11 showing no morphological changes as a result of ion irradiation.

Ti_3SiC_2 MAX Phase

Ti_3SiC_2 MAX phase joints were prepared in two ways. A titanium diffusion bonding process involving hot pressing at 1170°C at 20 MPa for 3 hours resulted in Ti_3SiC_2/Ti_5Si_3 joints, and a tape calendaring process using organic binders, plasticizers, and a mixture of TiC and Si powders heated at 1425°C at 30-40 MPa for 2 hours resulted in Ti_3SiC_2/SiC joints. Joints varied from 15 to 27 um in thickness. Samples were then neutron irradiated in HFIR to 3.4 and 5.0 dpa at temperatures of 500 and 800°C, respectively.

Shear tests showed a 16% drop in shear strength from the unirradiated to the irradiated condition (5.0 dpa, 800°C) in the Ti_3SiC_2/SiC joints, with a change in failure type from base material failure to flat failure in the joint plane. Ti_3SiC_2/Ti_5Si_3 joints retained full strength following irradiation, with failure consistently either fully or partially in the joint. SEM examination also revealed microcracking within the joints in both materials. TEM examination of the sample irradiated to 3.4 dpa at 500°C revealed the development of large amounts of displacement irradiation damage in the Ti_3SiC_2 grains and also showed microcracking to be primarily transgranular, though some cracking at grain boundaries was observed (Fig. 3). No cracking was observed at Ti_3SiC_2/Ti_5Si_3 interfaces.

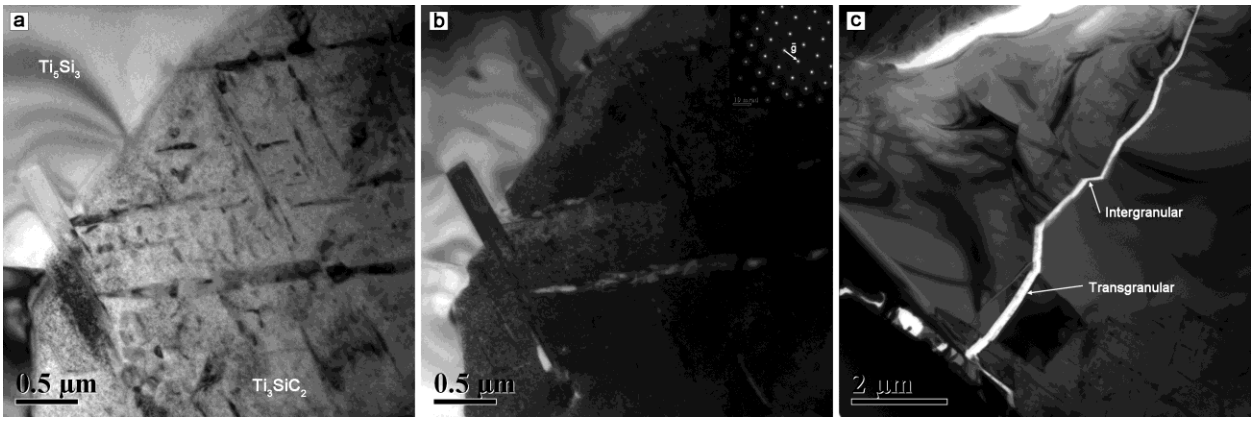

Figure 3. a) Ti_3SiC_2 grain shown at an arbitrary diffraction condition, showing dislocation loops and planar defects. b) The same grain shown in a 2-beam condition (diffraction pattern shown in insert), showing extensive dislocation damage. c) Microcracking seen both through and at some grain boundaries.

FUTURE PLANS

Microstructural, mechanical and physical property measurements will be performed on neutron-irradiated BMG, HEA and MAX phase samples to better interrogate irradiation effects in these materials. BMG specimens have been irradiated in HFIR to 0.1 dpa at 70 and 200°C, and HEA samples have been irradiated to 0.1 and 1 dpa at 70°C and 1 dpa at 500°C. Characterization is expected to begin in late CY2013 or early CY2014. Additional BMG specimens will be irradiated to 0.1 dpa at 200°C, and HEA samples will irradiated to 1 dpa at 500°C in order to obtain some scoping information on temperature dependence. Rabbit capsules containing MAX phase specimens began irradiation in HFIR during Cycle 449 at the end of July 2013. A total of three rabbit capsules, plus an additional six capsules that are part of a Japanese collaboration are being neutron irradiated at 400, 700, and 1000°C up to 2, 6, and 10 $x10^{25}$ n/m^2, E>0.1 MeV (~2-10 dpa). The MAX phase materials included in the HFIR irradiation capsules are sintered Ti_3SiC_2 and Ti_2AlC purchased from 3-ONE-2 LLC (Willow Grove, PA). A variety of specimen geometries including CTE beam, thermal diffusivity discs, and equi-biaxial flexural strength coupons are being irradiated.

4.0 ADVANCED STEELS

4.1 FOA - Development of ODS FeCrAl for Fusion Reactor Applications

B. A. Pint (pintba@ornl.gov), D. T. Hoelzer and K. A. Unocic

OBJECTIVE

The dual coolant (He and Pb-Li) system is the leading U.S. blanket concept for DEMO. Oxide dispersion strengthened (ODS) ferritic alloys are candidate structural materials due to their superior high-temperature mechanical properties and radiation tolerance. However, conventional ODS Fe-Cr alloys have not shown good corrosion resistance in Pb-Li. The objective of this project is to develop an ODS Fe-Cr-Al alloy with improved compatibility with Pb-Li above 550°C, while retaining the inherently attractive properties of ODS alloys.

SUMMARY

The first year of this project focused on defining the composition of the FeCrAl matrix and the oxide dispersion. To define the Cr and Al contents, cast model FeCrAlY alloys were exposed to Pb-Li in a 1000h capsule test at 700°C. These experiments identified 4.5-5%Al with the best compatibility. For the oxide stability, the thermodynamic model of HfO_2-Y_2O_3 was combined with the other two constituent pseudo-binaries of Al_2O_3-Y_2O_3 and Al_2O_3-HfO_2. Diffusion couple experiments at 1250 and 1650°C showed that Ti was very reactive with Al_2O_3 and Y_2O_3. Much less reaction occurred with HfO_2 and ZrO_2. The information learned in the compatibility experiments was used to select Fe-12Cr-5Al and Fe-13Cr-4.5Al for the first ODS compositions. Powder was purchased and batches have been milled and are awaiting consolidation by extrusion in early FY14.

PROGRESS AND STATUS

Figure 4 summarizes the compatibility information generated on cast FeCrAlY alloys. The mass change was strongly dependent on the Al content and less dependent on the Cr or Y contents. Alloys with 3%Al all exhibited mass losses similar to 9Cr steel under these conditions while 5%Al was needed to achieve little or no mass change after exposure. Based on these results, four powder compositions were purchased for fabrication. The initial milling has focused on the Fe-12Cr-5Al composition and three batches are awaiting extrusion in early October at ORNL.

Compared to the highly stable Y-Ti-O nano-oxide dispersion in Fe-(9-14)Cr, the Al addition presents serious challenges to the choice of oxide dispersion since Al_2O_3 is thermodynamically more stable than TiO_2 and readily reacts with Y_2O_3 to form a number of stable compounds. Ideally, another addition would react with Y_2O_3 to form a nano-dispersion in FeCrAl. Computational work focused on the Al_2O_3-Y_2O_3-HfO_2 system where there was disagreement between the experimental and predicted phase diagrams. Isothermal and isoplethal data from the experimentally assessed phase diagram of Al_2O_3-Y_2O_3-HfO_2 were used to adjust the ternary model parameters. For validation, ternary diffusion couples were aged at 1250 and 1650°C. By far, TiO_2 was the most reactive with Al_2O_3, diffusing millimeters into the substrate. Both ZrO_2 and HfO_2 were more stable, with limited solubility in Al_2O_3 and <1μm thick reaction layer at 1650°C. Figure 5 shows EDS analysis of the Al_2O_3-Y_2O_3-HfO_2 and Al_2O_3-Y_2O_3-ZrO_2 couples annealed at 1650°C. In the reaction zone in each case, there appears to be less Hf present in the Y_2O_3 phase while Zr appeared to form a complex $(Al,Y,Zr)O_x$ phase, Figure 5b. Powder batches were milled with Y_2O_3, Y_2O_3 and ZrO_2, and Y_2O_3 and HfO_2 to investigate the effect on the resulting oxide dispersion in the consolidated Fe-12Cr-5Al alloy.

FUTURE PLANS

In year two of the project, the milled FeCrAl powders will be consolidated followed by tensile, creep and Pb-Li compatibility testing and characterization of the resulting microstructure. Of particular interest will be the mass change in Pb-Li and the composition of the nano-dispersed oxides in the FeCrAl matrix.

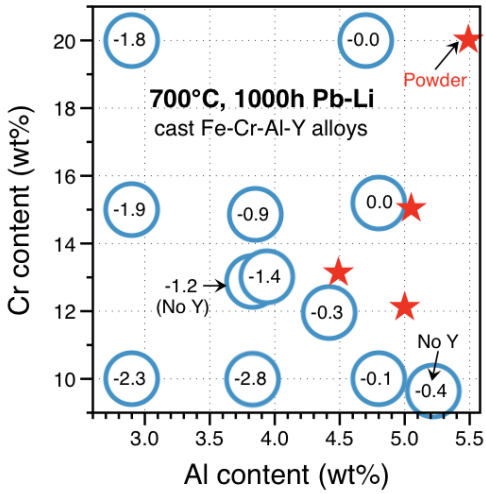

Figure 4. Specimen mass change for the cast FeCrAlY alloy coupons after exposure to Pb-Li for 1,000h at 700°C as a function of Cr and Al contents. The stars mark the composition of four powder batches.

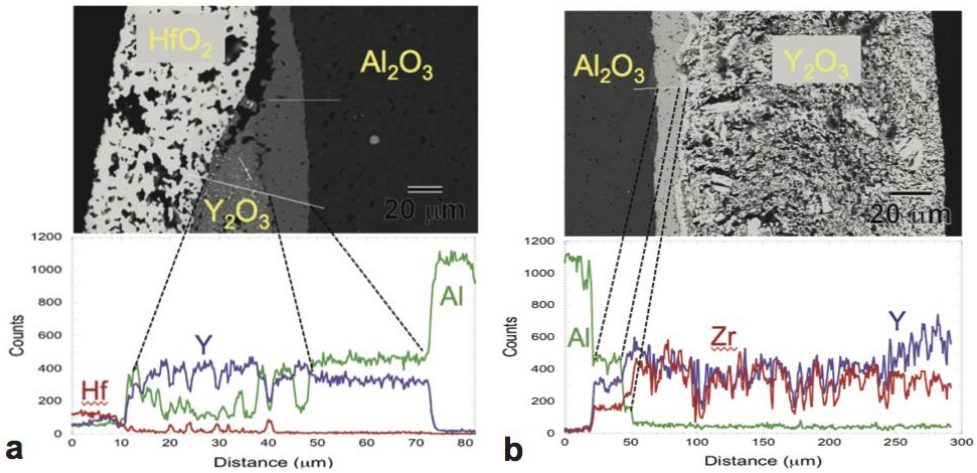

Figure 5. SEM images and EDS profiles for diffusion couples after 1h at 1650°C (a) Al_2O_3-Y_2O_3-HfO_2 and (b) Al_2O_3-Y_2O_3-ZrO_2.

4.2 Development of Advanced Reduced-Activation Ferritic-Martensitic (RAFM) Steels

L. Tan (tanl@ornl.gov), T.S. Byun, Y. Katoh, L.L. Snead

PROGRESS IN ADVANCED RAFM STEEL DEVELOPMENT

Reduced-activation ferritic-martensitic (RAFM) steel ORNL 9Cr-2WVTa, developed in the late 1980s, exhibit greater strength and adequate Charpy impact resistance than other grades. Based on the approach for RAFM steels with improved creep strength outlined recently by R.L. Klueh, a new version of RAFM steel ORNL 9Cr-1WVTa has been developed, together with thermomechanical treatment (TMT) to optimize the properties. Computational thermodynamics has been employed to evaluate alloy microstructure, guiding alloy composition adjustment and TMT temperature selection.

The new RAFM steel has shown enhanced strength without sacrificing ductility, improved creep creep strength and life at 600°C, adequate Charpy impact resistance (ductile-brittle transition temperature and upper shelf energy), fracture toughness at temperatures up to 700°C, and thermal aging resistance at 650°C. Figure 6 shows the temperature-dependent yield stress and total elongation of the newly developed ORNL 9Cr-1WVTa in two TMT conditions. Except for F82H, the other alloys were tested using the same type of miniature specimens with a gage section of 1.52 mm wide by 0.76 mm thick. Thus, F82H is not included in the total elongation comparison. The newly developed ORNL 9Cr-1WVTa has either comparable (T1 version) or superior (T2 version) strength compared to ORNL9Cr-2WVTa, HT-9, PM2000, and F82H. More importantly, the new alloys also exhibited comparable or greater total elongation.

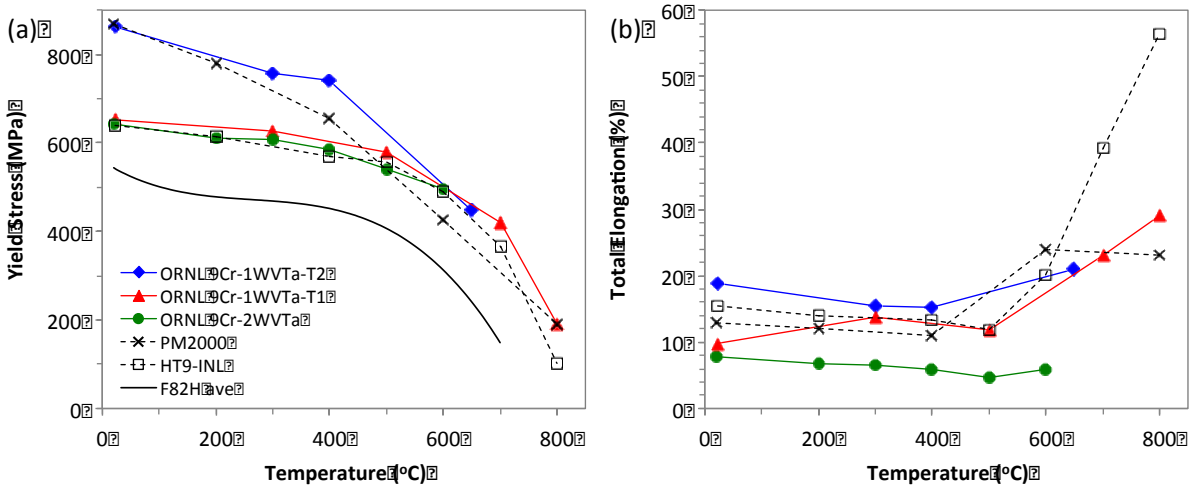

Figure 6. Temperature-dependent (a) yield stress and (b) total elongation of the new ORNL 9Cr-1WVTa compared to literature data of ORNL 9Cr-2WVTa, F82H, HT-9, and PM2000.

The FM steels in Fig. 6 show significant weakening at temperatures above 500-600°C. The ORNL 9Cr-1WVTa-T1 exhibited the greatest resistance to the strength loss at high temperatures. The occurrence of softening results from the reduced pinning effectiveness of coarsened or dissolved precipitates leading to recovery of dislocation substructures. MX-type nanoprecipitates, with M = metals and X = C/N, are believed to be key element for retaining high-temperature strength and creep resistance of FM steels due to their significantly lower coarsening rate than $M_{23}C_6$ and Laves phase in 9-12Cr FM steels. Additionally, it is believed that a high density of MX nanoprecipitates can serve as sinks for radiation-induced defects, leading to improved radiation resistance. Therefore, it is essential to examine the stability of MX-type nanoprecipitates under thermal, stress, and irradiation conditions. The results will

benefit not only the understanding of the degradation mechanism of current RAFM steels, but also the development of advanced RAFM steels with superior high temperature performance and radiation resistance.

STABILITY OF MX-TYPE STRENGTHENING NANOPRECIPITATES

TaC, TaN, and VN are common MX-type nanoprecipitates present in RAFM or conventional FM steels. A few studies had shown the instability of these nanoprecipitates under thermal and/or stress conditions. Approximately complete dissolution of TaC was reported for a model alloy after Fe^{3+} ion irradiation to 20 dpa (displacement per atom) at 500°C, as well as for ORNL 9Cr-2WVTa and JLF-1 RAFM steels after fast neutron irradiation to 5 dpa at 300°C. These observations suggest that TaC in RAFM steels would be unstable under irradiation, resulting in softening of the steels at relatively low temperatures such as 300-500°C. This is detrimental to use of RAFM steels. Therefore, a systematic study has been pursued using model alloys favoring the formation of TaC, TaN, and VN nanoprecipitates, to develop a clear picture of the stabilities of these nanoprecipitates.

Three types of experiments, i.e., thermal aging at 600 and 700°C for up to 5000 h, creep at 600°C and ~70% yield strength, and Fe^{2+} ion irradiation at 500°C for a nominal dose of ~20 dpa with a dose rate in the range of $(1.2 – 7.6)\times10^{-4}$ dpa s^{-1}, have been conducted on the TaC/TaN/VN alloy samples. The microstructures of the samples were primarily characterized using transmission electron microscopy (TEM) and scanning TEM (STEM) techniques on a FEI CM200 field-emission-gun TEM/STEM equipped with an EDAX energy dispersive X-ray spectroscopy (EDS) detector. TEM specimens of the ion-irradiated samples were lifted out from a specimen depth greater than the irradiated zone and thinned to electron-transparent using focused ion beam (FIB) on a Hitachi NB5000. TEM disks with 3-mm diameter were also thinned for some bulk samples using a Struers Tenupol electro-polishing unit with a methanol-nitric acid (3:1) solution at ~10 V and -16°C. Specimen thickness of the characterized regions was estimated using the convergent beam electron diffraction (CBED) technique. The detailed sample conditions that have been characterized are listed in Table 4.

Table 4. Sample conditions that have been characterized to evaluate the stability of the nanoprecipitates

Condition		**TaC**	**TaN**	**VN**
Initial		As fabricated	As fabricated	As fabricated
Thermal aging	600°C	100 h	100 h	100 h
		1000 h	1000 h	1000 h
		5000 h	5000 h	5000 h
	700°C	100 h	100 h	100 h
		1000 h	1000 h	1000 h
		5000 h	5000 h	5000 h
Creep at 600°C		170 MPa	170 MPa	100 MPa
Fe^{2+} irradiation		500°C for ~20 dpa	500°C for ~20 dpa	500°C for ~20 dpa

Statistical measurement of the size and density of the nanoprecipitates under different conditions has been conducted based on the TEM characterization results. The nanoprecipitates showed coarsening with reduced density during aging at 600°C. In contrast, the aging at 700°C primarily resulted in dissolution and reprecipitation, with some coarsening. TaC and TaN exhibited the greatest and poorest resistance to the aging-induced degradation, respectively. The resistance to aging-induced degradation of VN was comparable or inferior to TaC. The observations are approximately consistent with the available literature data. The applied stress during creep testing broke TaN platelets into smaller pieces, leading to increased density and reduced size of the platelets. In contrast, the stress only introduced dislocations in the TaC and VN nanoprecipitates. The stress had the least effect on TaC nanoprecipitates with slight dissolution, but accelerated the growth of VN with density reduction. The Fe^{2+} irradiation resulted in different levels of radiation-induced degradation and mechanisms for the nanoprecipitates. TaC exhibited the greatest resistance to radiation-induced degradation with moderate reprecipitation and slight dissolution. VN showed significant growth during low dose irradiation with reprecipitation and possible dissolution primarily occurred at higher doses. In contrast, irradiation primarily resulted in significant dissolution of TaN. The observations are not consistent with the significant dissolution of TaC reported in literature. Detailed description and discussion on the radiation resistance of the nanoprecipitates has been reported in a paper, entitled "Stability of the strengthening nanoprecipitates in reduced activation ferritic steels under Fe^{2+} ion irradiation", submitted to Journal of Nuclear Materials.

In general, TaC exhibited the greatest degradation resistance, followed by VN, then TaN. TaC can help retaining microstructure stability, and thus strength, of RAFM steels at temperatures up to ~600°C. TaN would destabilize the microstructure of RAFM steels and thus alloy nitrogen content should be controlled to a minimum to limit TaN but favor TaC formation for RAFM steels, resulting in superior performance at elevated temperatures.

In addition to the stability study described above, TaC/TaN/VN samples, together with some alloy samples, have recently completed neutron irradiation in HFIR. The TaC/TaN/VN samples have been irradiated to $(0.1 – 20)\times10^{25}$ n m^{-2} at 300, 500, and 650°C. Similar neutron irradiation conditions have been achieved in other alloy samples such as the new ORNL 9Cr-1WVTa and modified Grade 92 type steels.

FUTURE PLANS

The knowledge learned from the stability study will be used to develop advanced RAFM steels that favor the formation of a high density of MX nanoprecipitates with superior degradation resistance at elevated temperatures. Additionally, some of the neutron-irradiated samples will be characterized to evaluate neutron irradiation effects and to compare the MX stability under neutron irradiation to the ion-irradiated results.

4.3 RADIATION EFFECTS ON MECHANICAL & PHYSICAL BEHAVIOR OF REDUCED ACTIVATION FM STEELS

T.S. Byun (byunts@ornl.gov), D. Hamaguchi (JAEA), and Y. Katoh

OBJECTIVE

This research is to evaluate the post-irradiation mechanical properties of the reduced activation ferritic-martensitic steel F82H and to develop necessary small specimen testing and evaluation techniques. The focus is on the radiation effects on the fracture resistance of the steel.

SUMMARY

Post-irradiation examination (PIE) has been continued for the ferritic-martensitic (FM) steel specimens from the HFIR capsule RB15J irradiated to about 4 or 6 dpa at 300 and 400°C. The majority of specimens were the miniature precracked Chevron-V notch (PCCVN) and disk-compact tension (DCT) specimens of the Japanese FM steel F82H and its tungsten inert gas (TIG) weld variants. Fracture tests for the PCCVN specimens were completed in FY 2012. In FY 2013 new fracture resistance (J-R) testing and evaluation technology has been established for the miniature DCT specimens. A cradle type grip assembly was also developed and used. These new techniques were successfully implemented in the tests in hot cells and radiation-free areas and in data analysis: (a) Testing and analysis for non-irradiated DCT specimens were completed using the newly developed technology. (b) Fracture tests of irradiated DCT specimens at room temperature and irradiated temperatures were also performed and J-R analysis for those data is underway. (c) Preparation of equipment and testing techniques for low temperature (below room temperature) fracture testing was also completed and testing is underway. The PIE campaign also included low-cycle fatigue testing and thermal expansion measurements. An electromagnetic machine was successfully installed in the 3025 hotcell facility and low cycle fatigue tests using dog-bone type miniature specimens has been attempted. The coefficient of thermal expansion (CTE) was measured on selected neutron irradiated F82H specimens.

PROGRESS

Fracture testing and evaluation technology

Fracture toughness testing in a high radiation area (hot cell) using miniaturized specimens has become a major challenge in the evaluation of high dose materials as it requires high precision recording of load-displacement data, including loading-unloading cycles, often in vacuum or a controlled environment. A modified procedure for fracture testing and J-R curve construction has been developed to test miniature disk-compact tension (DCT) specimens in high radiation areas. The fracture testing procedure was simplified by eliminating any externally-attached displacement gage and by using a cradle type grip assembly, Figure 7.

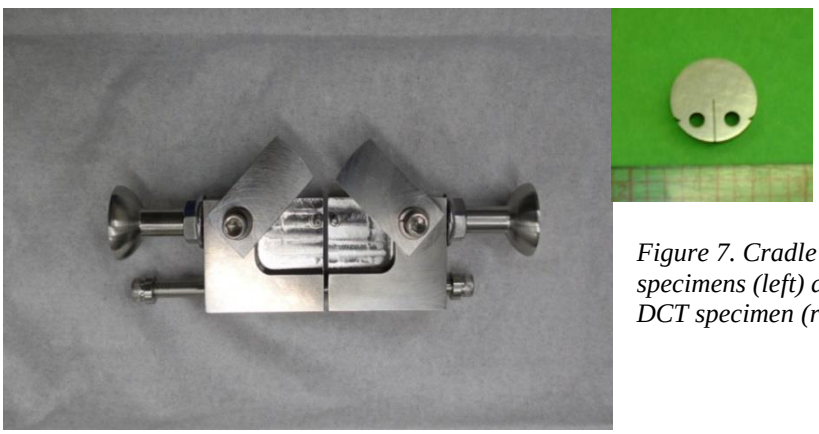

Figure 7. Cradle type fracture test grip for small DCT specimens (left) and a 4.7 mm thick 12.5 mm diameter DCT specimen (right).

In the J-integral evaluation procedure, the load-displacement curve normalization method for calculation of crack lengths was modified to accommodate the experimental simplification. As displayed in Figure 2, the baseline tests for the F82H ferritic-martensitic steels confirmed that the newly established procedure can produce correct J-R curves with good repeatability. Fracture toughness (J_Q or K_{JQ}) can be obtained from these J-R curves: the initial linear portion of the curves, usually called the crack blunting lines, are extended and shifted by 0.2 mm, and the intercepts between the shifted linear lines and corresponding J-R curves are defined as fracture toughness. For the cases displayed in Figure 8, the J_Q values determined are in the range of 250–320 N/mm; these can be converted to K_{JQ} values, which are in the narrower range of 240–270 MPa√m.

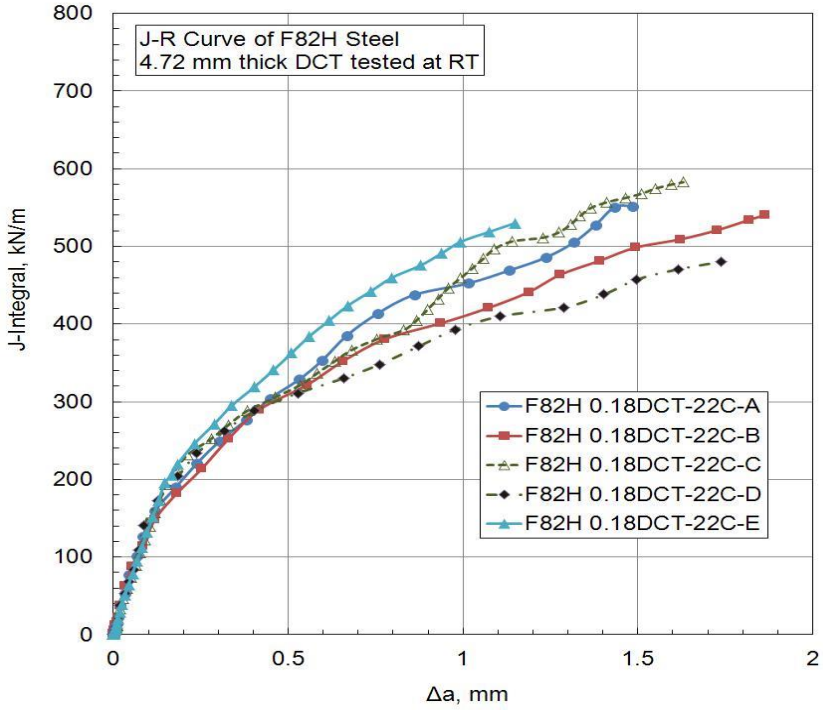

Figure 8. J-R curves for F82H 4.7 mm thick DCT specimens.

Tests of irradiated DCT specimens

Static fracture tests are carried out for irradiated F82H DCT specimens in 3025E hotcell facility using the newly developed techniques described above. So far, six irradiated base and weld metal specimens have been tested and the raw data are analyzed for fracture characteristics and calculated J-R curves. Testing of remaining specimens is continuing. Figure 9 displays two examples of fracture surfaces obtained using a remote-controlled microscope. The photograph in the left shows a heat-tinted band in the necked middle region, which has been formed by stable crack growth during the test. However, the one on the right shows no stable crack growth marking as the specimen broke in brittle mode in the linear loading region. Also shown are the small yellow markings that were made for crack length measurement.

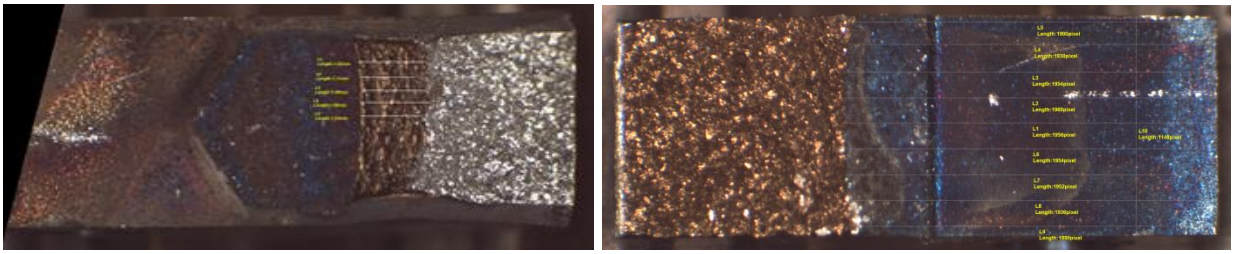

Figure 9. Fracture surfaces taken with an optical microscope and used for measurement of crack length in the hot cell: OWEa (left) and OVXb (right).

The appearances of fracture surfaces, which can reflect specimen fracture mode, are summarized in Table 5, along with irradiation and test conditions. The two F82H base metal specimens irradiated at 384 and 396°C (OWEa and OWEe, respectively), demonstrated highly stable crack growth. The next two specimens, OVXB and OVAG, failed in brittle or semi brittle mode as their irradiation temperature was lower, 316 °C. Both of the weld specimens failed in brittle mode regardless of the different test temperatures.

Table 5. Irradiation and testing conditions and fracture behavior of irradiated F82H base and weld metal.

ID	Material	Specimen Type	Irrad. Temp. [^{o}C]	Dose [dpa]	Test Temp. [^{o}C]	Fracture Behavior
OWEa	F82H IEA	0.18" DCT	384	5.6	22	Stable & ductile crack growth
OWEe	F82H IEA	0.18" DCT	396	5.7	22	Stable & ductile crack growth
OVXB	F82H IEA	0.14" DCT	316	4.5	22	Brittle fracture
OVXG	F82H IEA	0.14" DCT	316	4.5	300	Pop-in & ductile cracking
1VXA	F82H TIG WM	0.14" DCT	315	3.2	22	Brittle fracture
1VXG	F82H TIG WM	0.14" DCT	315	3.2	300	Brittle fracture

Thermal expansion measurements

The coefficient of thermal expansion (CTE) was measured on a few reduced activation ferritic steels neutron irradiated in the HFIR RB position. The materials used for examination were F82H IEA, F82H-mod3, and Eurofer97 base metals plus F82H TIG weld metal, which were irradiated to 2.7 dpa at 300˚C. The coupon specimens with dimensions of 4x16x0.5 mm were employed in CTE measurement using dilatometer DIL 402 C (NETZSCH GmbH) from RT up to 450˚C except for Eurofer97, which was tested up to 550˚C. The measured CTE and hardness tests on Eurofer97 confirmed that the damage recovery takes place from 450˚C or above; which led to the decision to test F82Hs at temperature up to 450˚C. The irradiated materials showed lower CTE than the nonirradiated materials in the test temperature range, but

the deviation was quite small and tended to decrease with temperature above the irradiation temperature of 300˚C. This result leads to the conclusion that overall the radiation effect on CTE is quite small for F82H at this dose level.

FUTURE PLANS

PIE for the remaining RB15J irradiated material will continue in FY 2014. The J-R fracture testing at high temperatures and the cryogenic fracture testing for master curve methods will be completed, and all related fracture mechanics analyses will be completed. Also, the majority of low-cycle fatigue tests will be completed in 2014.

4.4 FRICTION STIR WELDING OF ODS STEELS - FOA PROJECT

Zhili Feng (fengz@ornl.gov), Zhenzhen Yu, David T. Hoelzer, Lizhen Tan, and Mikhail A. Sokolov

OBJECTIVES

This project addresses the critical technology gap in the development of fusion energy structural materials – joining of oxide dispersion strengthened (ODS) steels, nanostructured ferritic alloys (NFAs), reduced-activation ferritic/martensitic (RAFM) steels, and dissimilar metal joining between ODS/NFAs and RAFM steels through friction stir welding technology, to eliminate or minimize property degradation in the weld region associated with conventional welding processes and meet the stringent operation requirement of a fusion reactor. The research focuses on understanding the stability of the strengthening phases in the weld region, and the bonding mechanisms between dissimilar structural steels as a function of FSW process conditions.

PROGRESS

A major project milestone for FY13 was to develop baseline FSW process conditions to produce defect free joints of ODS/NFAs alloys.

In FY13, friction stir welding experiments were conducted on ODS alloy MA965, two RAFM steels (EUROFER97 and an experimental RAFM steel with composition Fe-9Cr-1.48W-0.13Ta-0.09C), and between MA956 and EUROFER97 (dissimilar weld). Polycrystalline boron nitride was chosen as the welding tool material, due to its excellent hardness and thermal stability.

Defect free friction stir welds have been successfully made for the above same materials and dissimilar material combinations. Optical microstructure examination of the similar and dissimilar weld regions showed that consistent defect-free welds were obtained. It was also observed that the microstructures in the stir zone (SZ), thermo-mechanically affected zone (TMAZ), and heat-affected zone (HAZ) were significantly different from those in the base metal (BM), leading to the variation in mechanical properties within the welds. Fig. 10 summarizes the four different types of welds made in FY13 and the corresponding hardness mapping results.

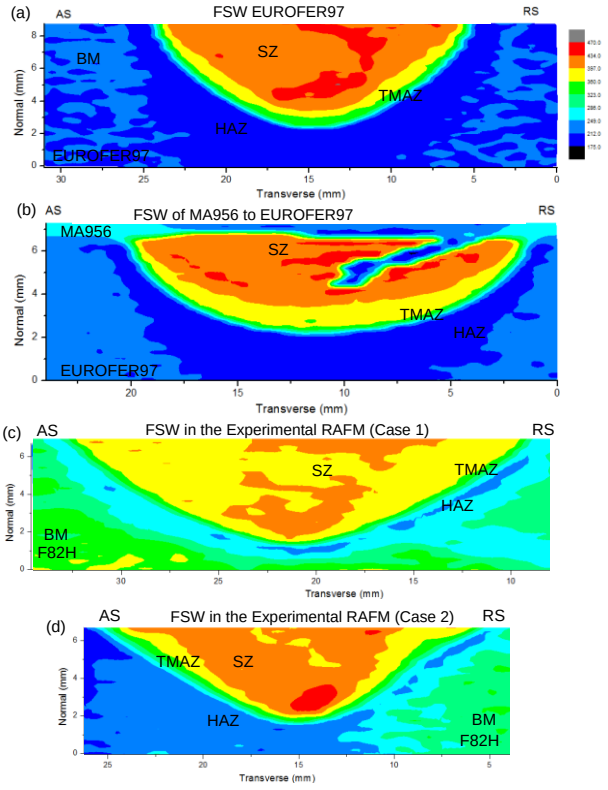

Figure 10. Hardness mappings of the similar and dissimilar FSW welds. AS and RS represent

In the same-metal welds made on both RAFM steels (EUROFER97 and the experimental RAFM steel), as in Fig. 10 (a), (c) and (d), significant hardness increase in SZ and a slight hardness decrease in HAZ were observed. Electron backscatter diffraction (EBSD) examination of the experimental RAFM steel welds (Fig. 11) indicates that FSW led to grain refinement in SZ (~2 μm), comparing to ~4 μm in base metal. No significant change in the micro-texture distribution was observed. By comparing Fig.10 (c) to (d), it was found that faster travel rate (Case 2), i.e., less heat input during FSW, resulted in higher overall hardness within SZ.

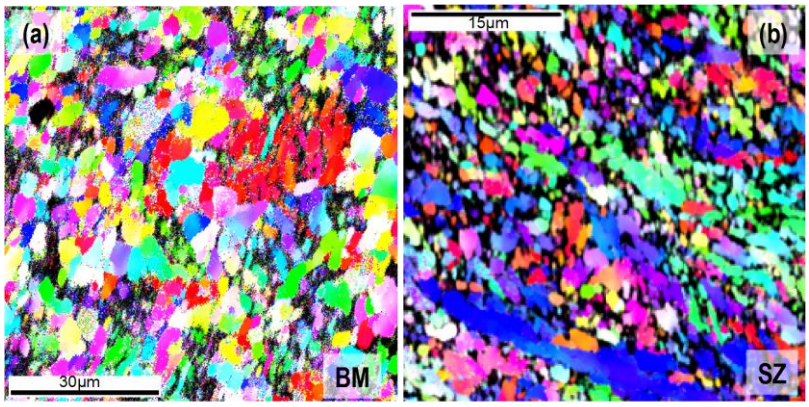

Figure 11. EBSD results of the base metal and stir zone in advancing side of the experimental RAFM steel FSW weld with a rotation speed of 400 rpm and a travel rate of 2.5 in/min.

In the dissimilar FSW of MA956 to EUROFER97, MA956 sheet (~1 mm thick) was placed on top of the EUROFER 97 plate (~25 mm thick). As shown in Fig. 10 (b), the regions with the dark blue color in the top layer and the orange color in the bottom layer represent the shape of SZ. A significant amount of the MA956, which is originally on top of the EUROFER97, is stirred down to the bottom of the stir zone by the downward stirring motion, as demonstrated by the dark blue color region surrounded by the orange color region within the bottom layer. A successfully bonded interface between EUROFER97 and MA956 was observed within the SZ, as shown in Fig. 12, without any evidence of cracks or defects. Sever grain coarsening was observed in the SZ of MA956, by comparing its micrograph in Fig. 13(b) to that of the BM in Fig. 13 (a). Note that although FSW process does not involve melting, the inevitable thermal input still may lead to the aggregation of nano-sized strengthening particles in MA956. Small angle neutron scattering (SANS) measurements were performed in the base metal and welded region to compare the dispersion of nano-scale features. Fig. 14 summarizes the SANS results and the calculated probability of nano particles size in a previous FSW trail in 14WT. SANS data of the MA956 FSW welds is being analyzed. Further investigation on the microstructure will be performed to identify the observed drastic decrease in hardness of MA956 SZ in Fig. 10 (b). Moreover, in order to characterize the influence of FSW on the strengthening mechanisms, high-energy synchrotron x-ray measurement was conducted to measure the localized dislocation density, size of coherent crystalline domains (e.g., sub-grain size) as a function of distance away from the weld center. Experiment results are currently being further analyzed.

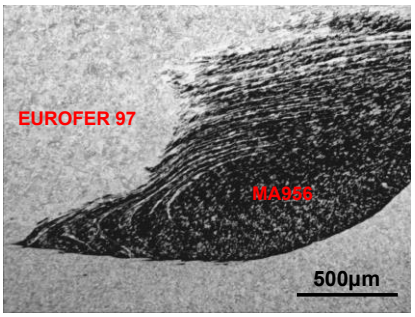

Figure 12. Optical micrograph of the dissimilar FSW weld of MA956 to EUROFER97

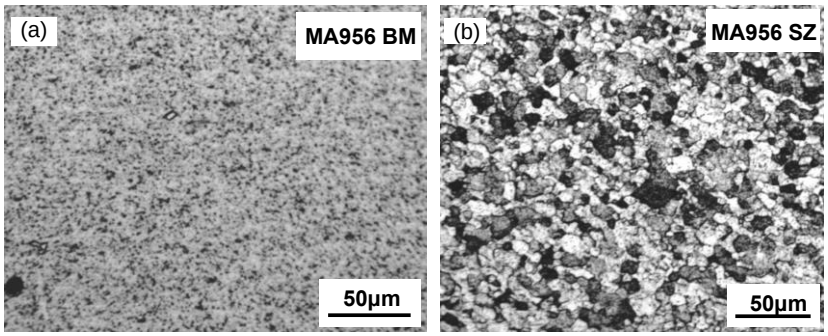

Figure 13. Optical micrographs of (a) the base material and (b) stir zone of MA956 in the case of dissimilar FSW weld of MA956 to EUROFER97.

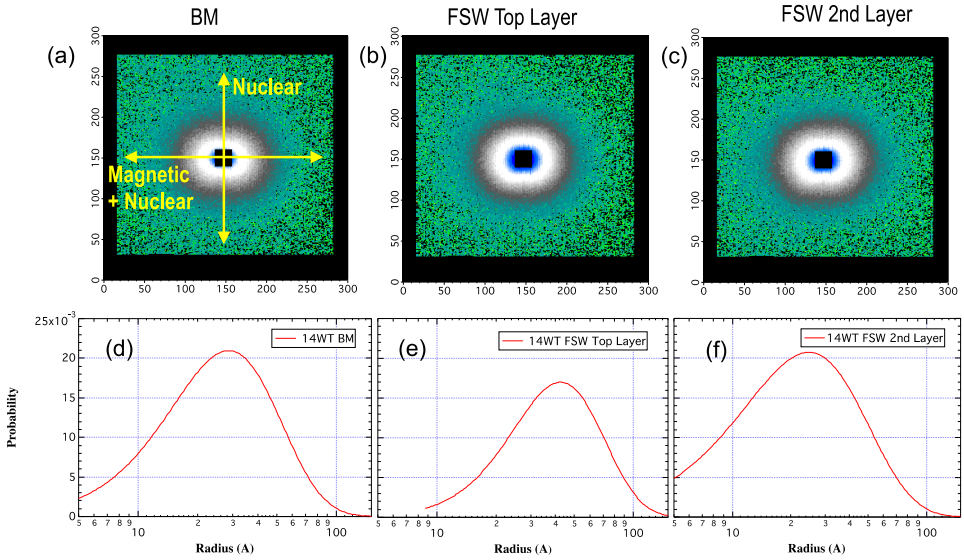

Figure 14. Small angle neutron scattering images (a)-(c) and the analyzed probability of nano particle size (d)-(f) in the BM, top layer and 2nd layer of friction stir welds in 14WT.

FUTURE PLANS

FSW with a wider range of parameter values will be performed in FY14 to develop a complete baseline condition. Post weld heat treatment (PWHT) with different conditions will be performed to minimize the property degradation introduced by FSW in the welds. Computational modeling will simulate the temperature and deformation history experienced by the ODS and RAFM alloys.

4.5 LIQUID METAL COMPATIBILITY – A THERMAL CONVECTION LOOP FOR Pb-Li COMPATIBILITY TESTING

S. J. Pawel (pawelsj@ornl.gov), A. W. Willoughby, M. S. Stephens, Z. M. Burns, B. A. Pint, J. D. McNabb

SUMMARY

This task will develop structural materials having compatibility with flowing Pb-Li eutectic that allows the maximum temperature for operation to be increased. Fabrication of the first Pb-Li thermal convection loop has been completed. The loop uses dispersion strengthened FeCrAl (Kanthal APMT) tubing, anticipated to have excellent resistance to Pb-Li. The loop will be used for compatibility tests in FY 2014.

INTRODUCTION

Currently, the maximum allowable wall temperature for the dual coolant lead-lithium (DCLL) blanket concept is set at 475˚C based primarily on corrosion limitations of the structural containment materials. To increase overall system efficiency, potential structural materials are being sought with a combination of high strength and creep resistance with simultaneous resistance to dissolution in eutectic Pb-Li at temperatures > 500˚C. Preliminary research using static capsule exposures has indicated that dispersion strengthened FeCrAl (Kanthal APMT) may be resistant to dissolution in eutectic Pb-Li at temperatures in the range of 600-800˚C, at least in part due to the stability of an Al-rich oxide film. However, corrosion data in a flowing system must be generated to analyze the potential for issues associated with thermal gradient mass transfer – relatively high dissolution in hotter portions of the flow system with concomitant deposition in the colder portions – which has been known to disrupt heat transfer and even plug flow paths completely in some temperature gradient – material combinations.

Thermal convection flow loops (TCLs) are planned as the follow-on step to capsule testing for evaluation of liquid metal compatibility. The initial testing will utilize a TCL fabricated of Kanthal APMT with APMT specimens for post-exposure evaluation in each of the hot and cold legs. Fabrication of the first TCL utilizing APMT tubing (26.7 mm OD, 3.1 mm wall), which evaluated welding and heat treatment procedures to be used in subsequent TCL construction with this alloy, was successfully completed.

RESULTS

Figures 15-17 depict key aspects of the fabrication process. The loop was fabricated in two major steps – completion of all saddle welds to join tubing sections, and then completion of all welds to insert the thermowells – with each step followed by post weld heat treatment (PWHT) of the entire loop within a large box furnace at 850˚C (1 h in air, slow cool). Heat tapes were used to maintain pre-heat temperatures (250˚C) at all weld locations prior to PWHT. After each PWHT event, welds were inspected with a combination of visual examination (borescope for loop internals), radiography, and dye-penetrant. A helium leak check of the final assembly revealed one small pinhole in the weld of a thermowell insert, which was repaired and followed by PWHT. Subsequently, the entire loop was subjected to pre-oxidation treatment (1050˚C in air, 8 h, slow cool) to prepare it for service in Pb-Li. The completed loop passed the final inspection and leak check.

FUTURE PLANS

The loop is expected to be used for compatibility tests in FY 2014.

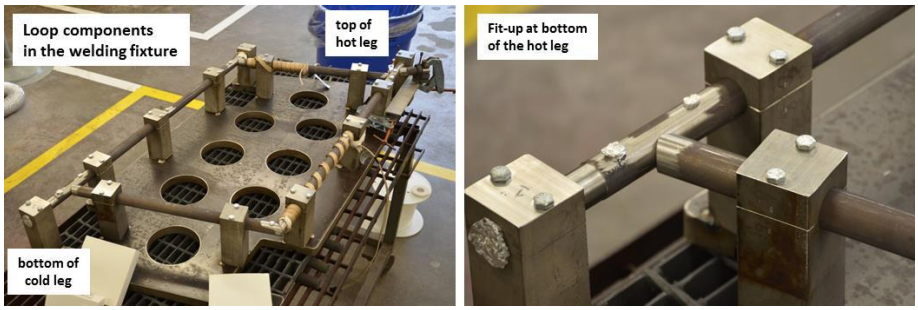

Figure 15. Initial loop fabrication. At left, the sections of loop tubing are shown positioned within the support fixture, with the first of several heat tapes already in place (for maintenance of pre-heat requirements). At right, detail of a saddle weld fit-up prior to welding.

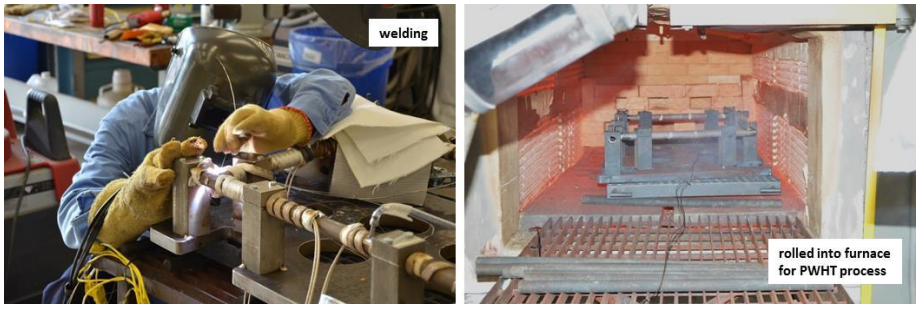

Figure 16. Welding and heat treatment. At left, completion of a saddle weld at the bottom of the loop. At right, the loop is shown within the box furnace for post-weld heat treatment (PWHT).

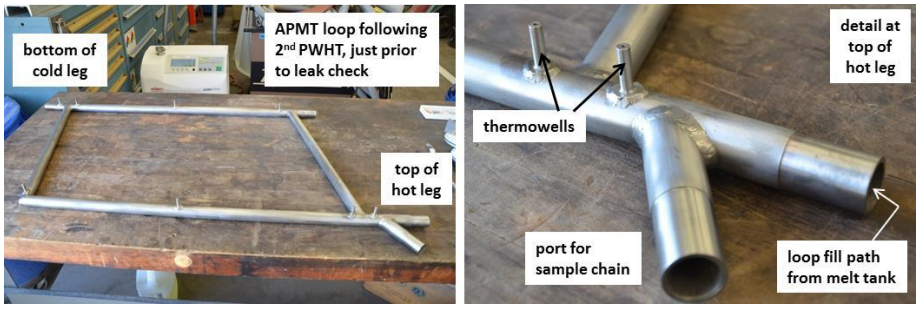

Figure 17. Completed thermal convection loop. At left, the loop is shown with all saddle welds and thermowell inserts in place after completion of PWHT (approximate dimensions are 120 cm tall and 60 cm wide). At right, detail at the top of the hot leg is shown. After final pre-oxidation heat treatment (not shown here), the loop developed a uniform dull straw-brown discoloration.

5.0 COMPOSITE MATERIALS

5.1. FOA - DEVELOPMENT OF SILICON CARBIDE JOINING TECHNOLOGIES FOR FUSION

Y. Katoh (katohy@ornl.gov), J.O. Kiggans, C. Shih, T. Koyanagi, L.L. Snead, T. Hinoki (Kyoto University), M. Ferraris (Politecnico di Torino), and C.H. Henager, Jr. (PNNL)

OBJECTIVE

Joining is a key technology for integration of silicon carbide (SiC) composite-based fusion blanket components. This work develops robust methods for joining SiC (or SiC composite) to itself, develops dependable test methods to determine the strength of those ceramic joints, and evaluates the stability of the candidate joining technologies under neutron irradiation.

PROGRESS

Process development for joining silicon carbide

Significant progress was achieved during this year in the SiC joining process development task, including: 1) detailed understanding of the relationship between the processing condition and the resultant microstructures that was achieved for titanium diffusion bonding, leading to identification of the processing conditions for a robust near-single phase bonding layer of Ti_3SiC_2, 2) a process for molybdenum diffusion bonding for very high strength was established, 3) an ultrasonic spray coating proved to be a useful technique to prepare the SiC joints through transient eutectic phase processes; the NITE (nano-infiltrated transient eutectic-phase) SiC joining and the yttria-alumina-garnet (YAG) joining demonstrated adequate strength, and 4) the pressureless NITE SiC joining process showed promise. Figure 18 shows the microstructures of two active metal diffusion-bonded joints that exhibited high strength.

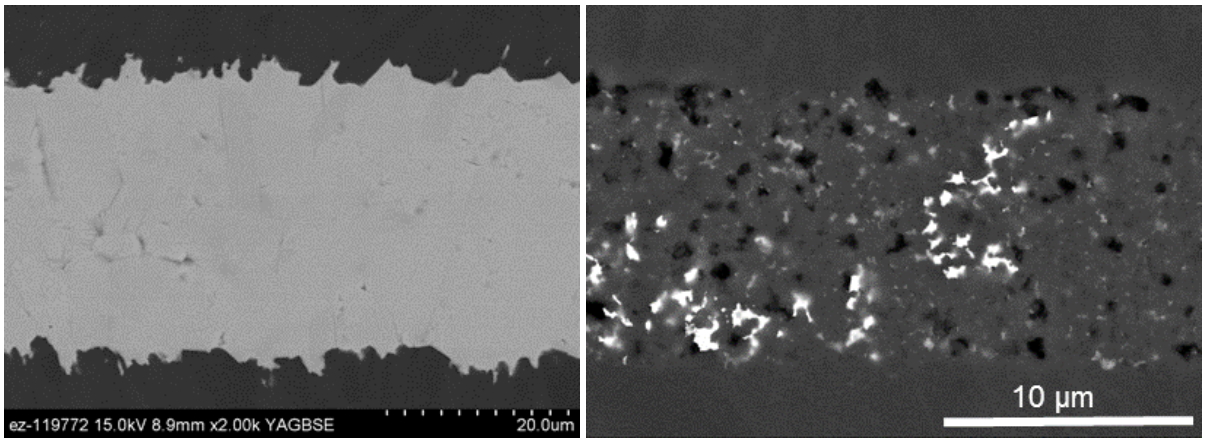

Figure 18. Backscattered electron micrographs of selected SiC joints showing near-single phase Ti_3SiC_2 bond layer in titanium diffusion-bonded SiC (left) and SiC-based bond layer produced through nano-infiltration and transient eutectic-phase process employing ultrasonic spray coating technique (right).

Test method development

A torsional shear test using solid hourglass type specimens with the square grip sections that had been developed in this study was proposed as a new work item for standard development in ASTM Committee C28 on Advanced Ceramics. This new test standard has been drafted and reviewed by the C28 task group.

In parallel with this standard development, work on alternative test methods that potentially provide advantages in time required for machining and/or minimum volume required for testing was pursued. The double-notch shear (DNS) test was utilized for providing a rough estimate of the strength of fabricated joints. While this method has the appeal of a quick and convenient test, it is known to be unable to provide a true shear load on the test specimens. Moreover, the sharp stress concentration around the notch tips causes inaccurate measurement of shear strength, as confirmed in the present study. As an alternativ, development of an asymmetric four-point bend (A4PB) test using a small notched specimen with bonded metallic extenders was initiated. This approach enables the use of specimens as small as the miniature torsion hourglass specimen developed in the present study without requiring time-consuming machining. The setups for the DNS and A4PB tests are shown in Figure 19Figure .

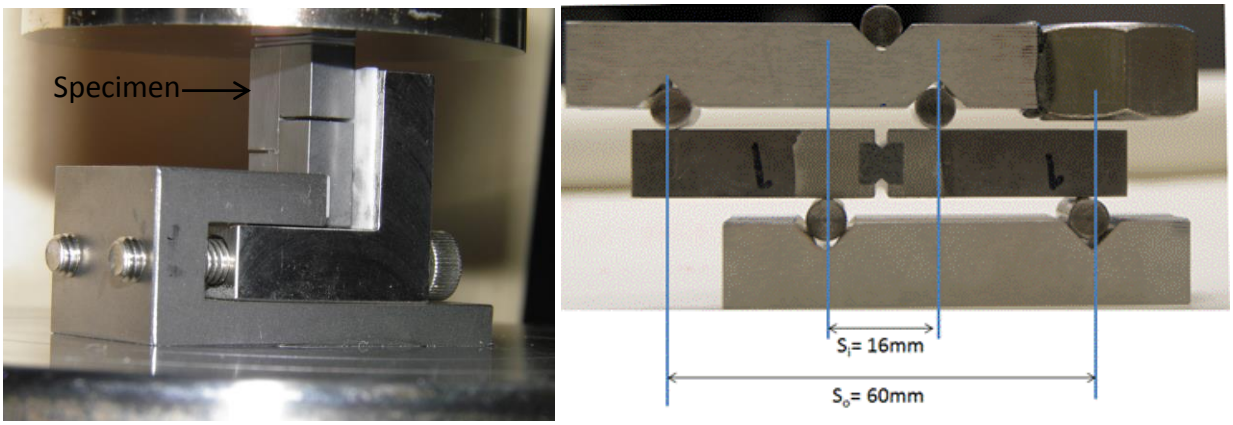

Figure 19. Double-notch shear test used for estimation of joint shear strength (left) and developmental asymmetric four-point bending test being developed for determination of shear strength of small joint specimens (right).

Irradiation effects on SiC joints

A series of irradiation experiments was carried out in the target region of HFIR with rabbit irradiation capsules. Using a capsule design developed specifically for the miniature solid hourglass torsion specimens, sixteen test specimens, typically four replicate specimens for each for four material variations, were irradiated in a single capsule. Each capsule contained post-irradiation SiC thermometry to ensure accurate reporting of irradiation temperature. Irradiation was carried out to approximately 3 to 5 x 10^{25} n/m^2 (E>0.1 MeV) at 500 and 800°C. This is equivalent to approximately 3 to 5 dpa. Testing showed striking results, with a general lack of significant degradation in shear strength after irradiation for all the joint test articles that had been tested, namely the titanium diffusion bonded, calcia alumina glass-ceramic bonded, Ti_3SiC_2 MAX-phase-bonded, and NITE-bonded (slurry or tape) CVD SiC, NTIE-SiC, or NITE-SiC/SiC -- all shown in Figure 20 . The conclusion is that selected methods of joining appear to produce a joined structure of SiC ceramics and composites of adequate strength that is maintained during irradiation at 500 to 800ºC to at least a few dpa.

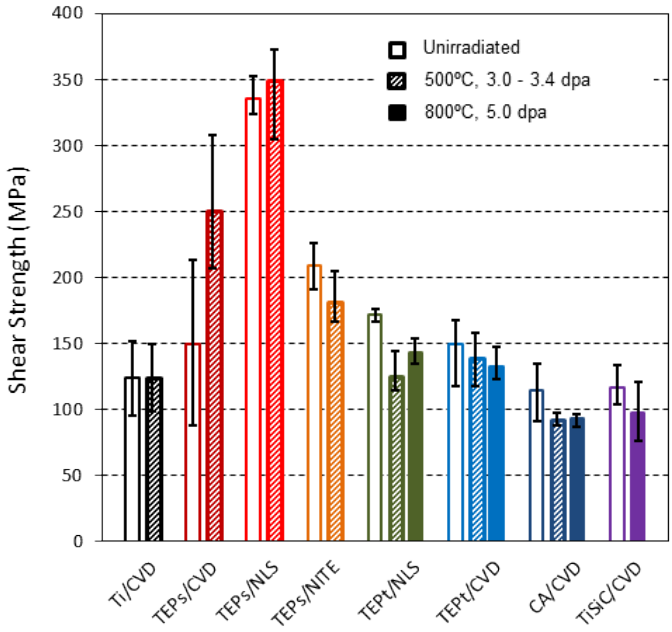

Figure 20. Shear strength of torsional shear test articles prepared by joining of chemically vapor-deposited SiC (CVD), NITE-like SiC (NLS), or NITE SiC composite (NITE) by titanium diffusion bonding (Ti), transient eutectic-phase SiC process with slurry (TEPs) or green tape (TEPt), calcia-alumina glass-ceramics (CA), or Ti_3SiC_2 MAX-phase.

FUTURE WORK

Processing: Identification of processing conditions that provide optimum joint properties will be pursued for the candidate joining methods for SiC and SiC composites, including the pressureless NITE process, and NITE and YAG processes with advanced coating technologies.

Test methods: Standard test methods for torsional shear strength of solid hourglass joint test articles will be developed in ASTM C28 on Advanced Ceramics. Development of alternative test methods that potentially offer significant advantage over the torsional shear test will be pursued.

Irradiation effects: The joint materials that demonstrated low dose irradiation stability at 500 and 800°C will be irradiated to higher doses (>10 dpa at 500°C) and at a higher temperature (1000°C). The newly developed joints will be subjected to screening irradiation testing to ~3 dpa at 500°C.

5.2 RADIATION EFFECTS IN SILICON CARBIDE CERAMICS AND COMPOSITES

Y. Katoh (katohy@ornl.gov), C. Shih, T. Koyanagi, L.L. Snead

OBJECTIVE

The overarching goal of this task is to advance fundamental understanding of the effects of neutron irradiation on silicon carbide (SiC) ceramics and SiC-based ceramic composites. The FY-2013 emphasis was on irradiation creep of SiC beyond the initial transient and the effects of high-fluence and/or high temperature irradiation on SiC fiber – SiC matrix (SiC/SiC) composites.

SUMMARY

1) The irradiation creep experiment on SiC up to intermediate fluence levels was completed successfully, revealing very small irradiation creep compliance values for steady-state creep of high quality SiC.
2) The effects of neutron irradiation to >70 dpa on SiC/SiC composite were examined in detail with the main focus on microstructural stability in the Hi-Nicalon™ Type-S fiber and the SiC-pyrocarbon interphase.
3) Extensive data on properties and irradiation effects for the near-stoichiometric nuclear grade SiC/SiC composites were compiled and published as a journal article.

PROGRESS

Irradiation creep of silicon carbide

Based on the ORNL successful development of the in-pile bend stress relaxation (BSR) technique for ceramics and composite, BSR creep samples of SiC ceramics and composites have been irradiated in HFIR at various elevated temperatures to the highest target dose of ~30 dpa. Following the completion of the initial set of experiments revealing the low dose irradiation creep behavior of these materials, test specimens irradiated to ~10 dpa were examined for creep strain. This lead to several new findings regarding the irradiation creep behavior of various SiC materials, including the lack of major stress relaxation even at a dose of ~10 dpa before which metallic alloys would have lost the stress (Figure 21), the progressive decrease in instantaneous creep compliances in the dose regime well beyond the initial transient, and the linear-averaged creep compliances in the order of 10^{-7} dpa^{-1} MPa^{-1} in a broad temperature range of ~300 - ~800°C.

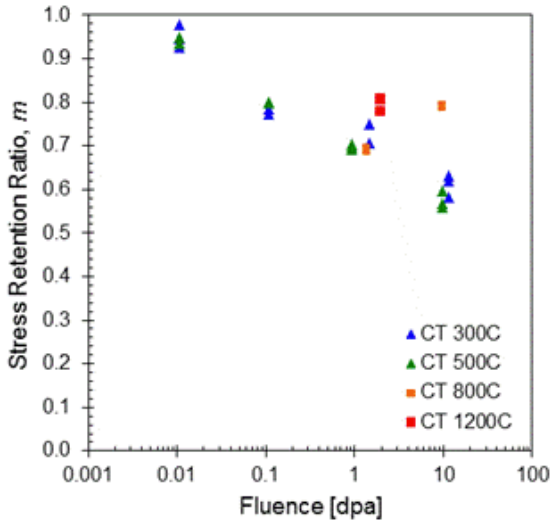

Figure 22. Bend stress relaxation behavior for Coorstek ultra-high purity chemically vapor-deposited SiC during neutron irradiation at elevated temperatures. The stress retention ratios appeared independent of the initial stress level that ranged from ~100 to ~300 MPa.

High dose neutron irradiation effects

The reference radiation-resistant grade silicon carbide composite, Hi-Nicalon™ Type-S fiber-reinforced chemically vapor-infiltrated silicon carbide matrix composite, was previously examined for mechanical and thermal properties following completion of neutron irradiation in HFIR to fluences greater than 70 dpa at 300, 500, and 800°C . Detailed examination and analysis were performed with these test specimens with X-ray diffraction (XRD) spectrometry analysis, dilatometry analysis, and transmission electron microscopy. The XRD spectra indicated substantial broadening of the diffraction peaks, to a greater extent for lower irradiation temperatures; however, substantial recovery of lattice strains that had been reported for lower dose irradiations were indicated. Interestingly, the dilatometry analysis in Figure 22 shows that the very clear recovery of macroscopic swelling takes place above the irradiation temperature even with the lack of XRD lattice expansion.

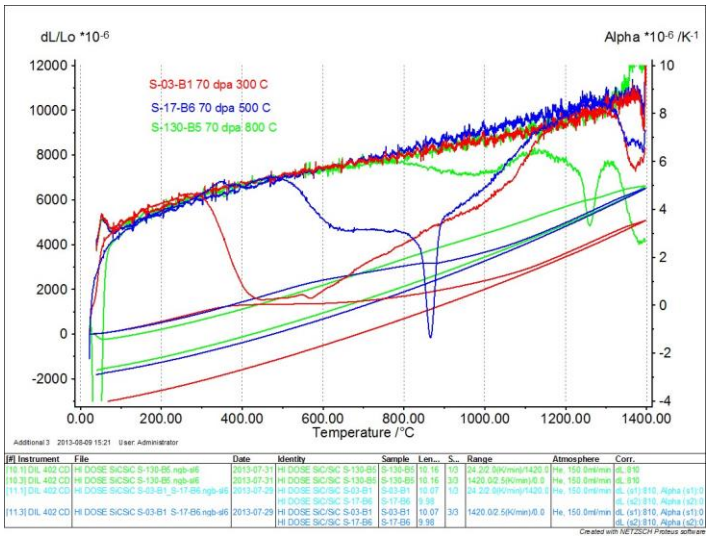

Figure 23. Dilatometry for SiC/SiC composite samples irradiated to >70 dpa at three different temperatures, showing recovery of irradiation strain starting at the irradiation temperatures of ~300, ~500, and ~800°C.

The main objectives of the TEM study included the examination of microstructural stability of the SiC-pyrocarbon multilayer interphase and the determination of the likely cause for degradation of mechanical properties of the Hi-Nicalon Type S fiber. The multilayer interphase, consisting of repeating layers of ~20 nm-thick pyrocarbon and ~200 nm-thick CVD SiC, appeared to have been significantly altered by irradiation to 71 dpa at 300°C as shown in Figure 23, whereas no noticeable change was observed after irradiation to a similar dose at a higher temperature of 800°C. The 300°C irradiation caused a transition of the turbostratic carbon layer into an amorphous carbon-SiC layer with increased thickness. The observation explains the more drastic change in mechanical properties of this composite due to irradiation at lower temperatures. On the other hand, no significant modification in microstructures was observed for the fibers, leaving the reason for the obvious radiation-induced fiber strength degradation unresolved.

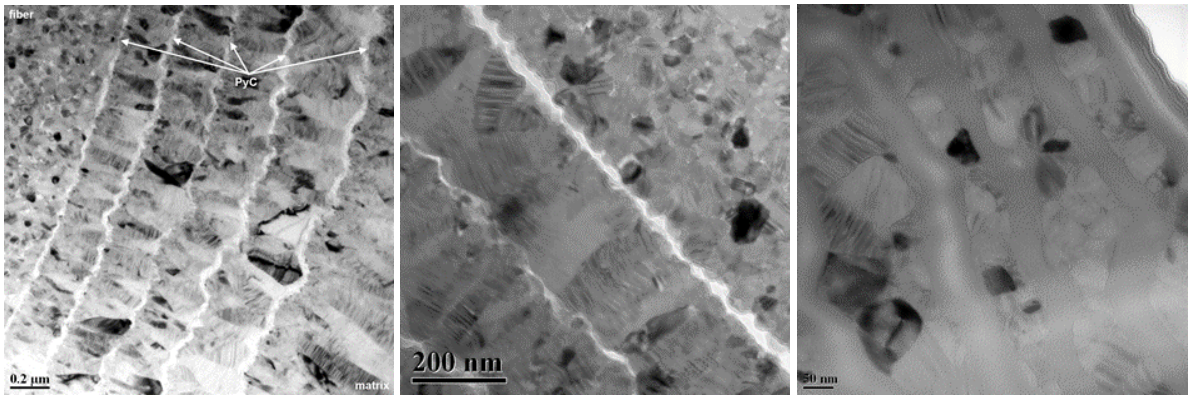

Figure 24. Microstructures of the SiC – pyrocarbon multilayer interphase before irradiation (left) and after irradiation to 71 dpa at 800°C (center) and to 71 dpa at 300°C (right).

Handbook of SiC/SiC composite properties

A comprehensive handbook of the properties of radiation-resistant, chemically vapor-infiltrated SiC/SiC composites was submitted and published online in Journal of Nuclear Materials. The handbook defines the SiC/SiC composite materials for high radiation applications and compiles physical, thermal, and mechanical properties, and the effects of neutron irradiation on those properties, making the first public document collecting the comprehensive properties of the nuclear grade SiC/SiC composites. The publication also summarized the six-year effort in the fusion/TITAN HFIR RB-18J irradiation experiment. Two examples of the new data included in the handbook are presented in Figure 24.

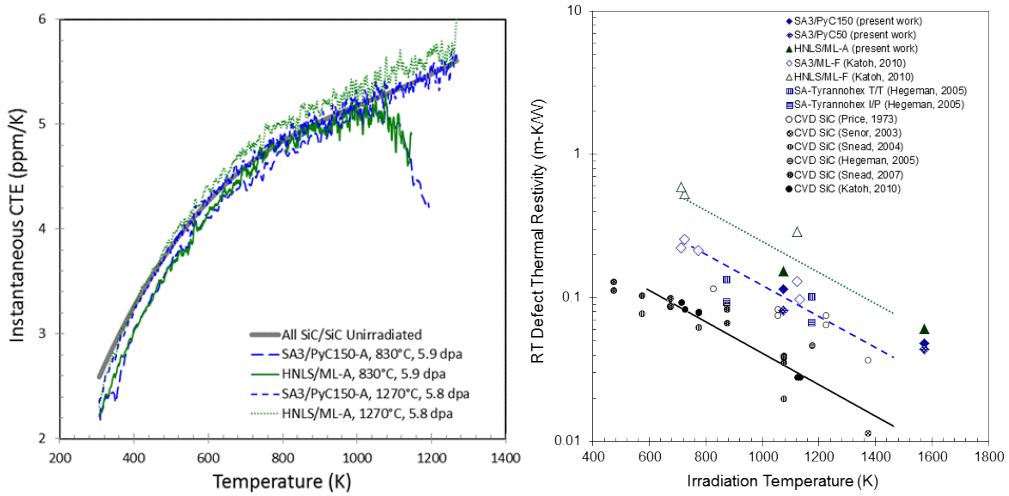

Figure 25. Effect of neutron irradiation on the thermal expansion and thermal recovery of irradiation-induced swelling (left) and effect of fiber grade and irradiation temperature on the defect thermal resistivity for radiation-resistant grade SiC/SiC composites.

FUTURE WORK

The BSR irradiation creep task will conclude after the set of capsules currently being irradiated in HFIR to the target dose of 30 dpa completes irradiation and the test specimens are examined for irradiation creep strain. Following these, the microstructural examination and analysis will be performed for understanding the effect of neutron irradiation under stress on the radiation defect evolution in silicon carbide. The high dose irradiation effects task continues with additional test specimens completing neutron irradiation to >100 dpa. Clarification of the origin for the mechanical properties degradation of this early nuclear grade Hi-Nicalon Type S composite due to very high dose irradiation is anticipated. Meanwhile, neutron irradiation of newer composite materials including those with the Tyranno-SA3 SiC fiber will continue to achieve intermediate to high fluences.

6.0 HIGH HEAT FLUX AND PLASMA FACING MATEIALS

6.1 ELECTRON-BEAM ADDITIVE MANUFACTURING OF TUNGSTEN MATERIALS FOR FUSION

E.K. Ohriner (ohrinerek@ornl.gov), R. Dehoff, and L.L. Snead

SUMMARY

The objective of this work is to produce graded tungsten-iron layers on a steel substrate using the ARCAM electron beam melting (EB) additive manufacturing system now under development at ORNL.

Initial experiments were performed with the ARCAM A2 electron beam additive manufacturing unit using standard beam deflection conditions. Local regions were observed with the desired microstructure of a solid tungsten surface layer and a liquid phase sintered boundary layer of tungsten particles in a steel matrix. A new ARCAM unit is currently being installed for use in future experiments.

PROGRESS AND STATUS

Single layers of tungsten powder 0.8 and 1.6 mm thick have been deposited on steel and EB melted. A steel coupon with melted tungsten powder is shown in Fig. 25. Tungsten powder bed depths of about 1 mm result in substantial melting of the steel substrate. A powder bed depth of 1.6 mm resulted in melting of the top surface of the tungsten powder bed, no melting of the steel substrate, and little adherence of the melted tungsten layer to the steel. A powder bed depth of 1.4 resulted in a nearly continuous fully melted tungsten powder with a porous subsurface region of liquid phase sintered tungsten particles in a steel matrix. A powder bed depth of 1.2 mm produced in some local areas the desired microstructure of a surface layer of essentially pure tungsten bonded to the steel substrate by a subsurface layer of steel infiltrated tungsten particles (Fig 26.) The phases present near the boundary region, as identified by SEM, are shown in Figure 27.

Since the melting is accomplished by deflection of the electron beam across the surface of the powder bed in an arbitrary and non-optimal pattern, the melting of the surface is not uniform. An example of this can be seen in Fig. 28 on the surface of a melted tungsten powder layer of 1.4 mm thickness. It is increasingly apparent that a much more sophisticated beam deflection pattern that accounts for thermal cycles, with localized in-process changes in thermal conductivity, is needed to obtain consistent uniform surface layers with the desired structure such as in Figure 26.

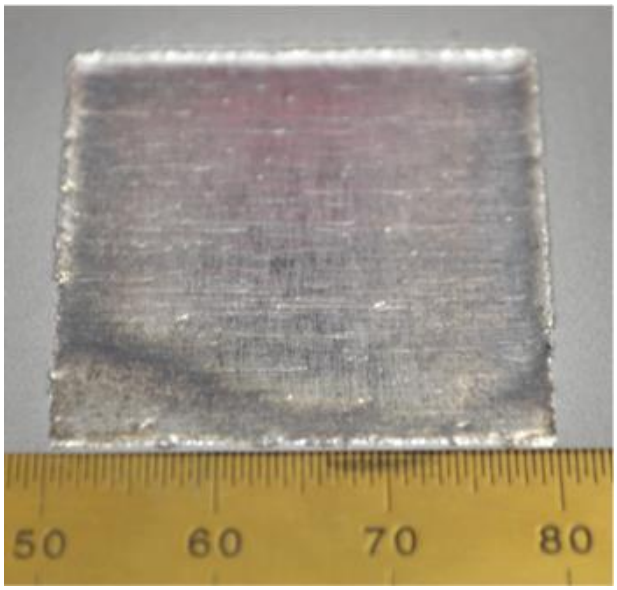

Figure 25. Melted tungsten powder incorporated into H-13 steel coupon

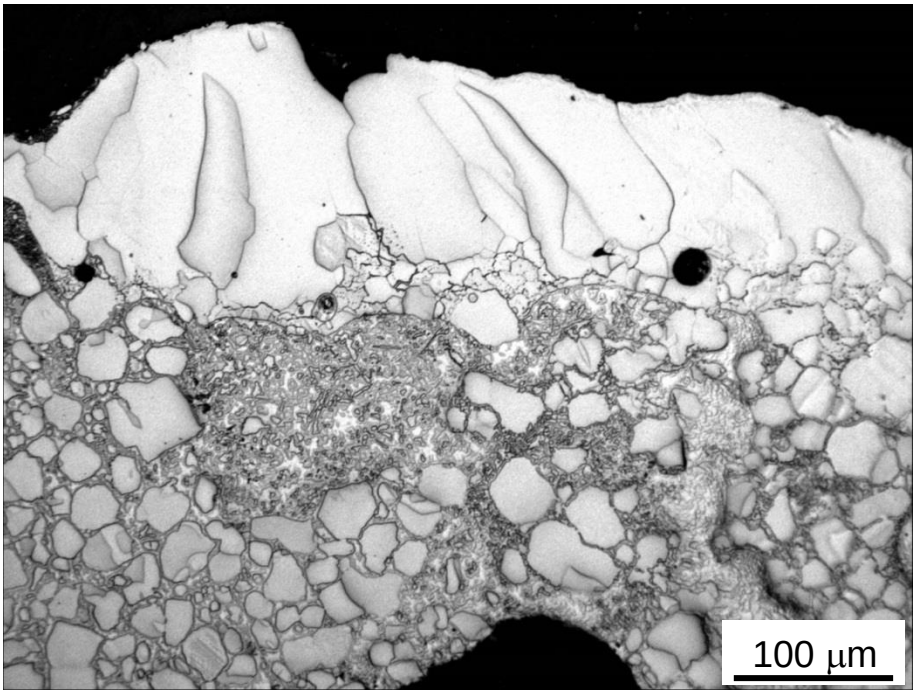

Figure 26. Cross-sectional view of melting with powder bed depth of 1.2 mm shows a local continuous fully melted layer of tungsten powder, at top, bonded to the steel substrate by an intermediate layer of tungsten particles (light contrast) infiltrated by steel (dark contrast.)

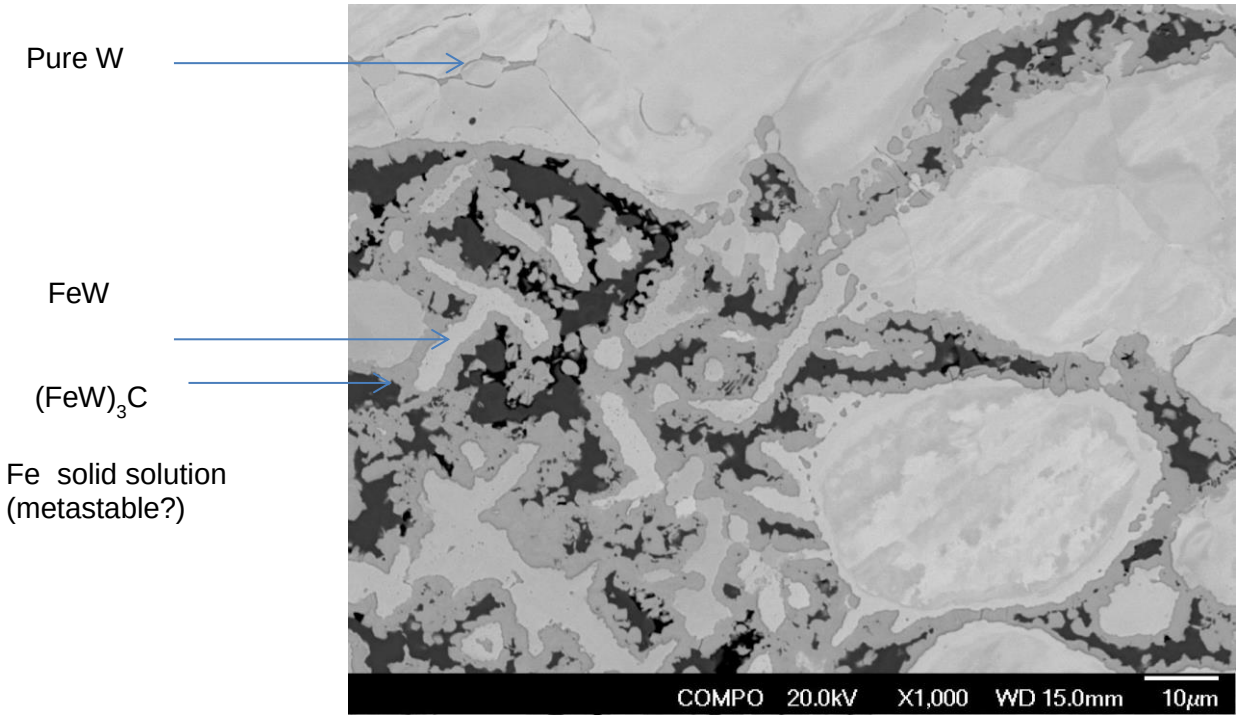

Figure 27. Back-scattered electron image of boundary region of Figure 2 showing phases present as identified by energy dispersive x-ray analysis.

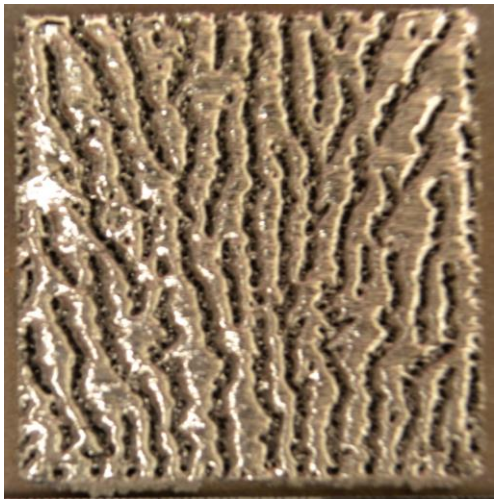

Figure 28. Surface view of melting with powder bed depth of 1.4 mm shows pattern of fully and partially melted areas associated with the pattern of beam deflection across the sample surface.

FUTURE EFFORTS

New experimental equipment has been installed and is now available for process experiments with tungsten. A graduate student has been begun working on this effort and is initially performing metallographic examination of fabricated coupons.

6.2 IRRADIATION EFFECTS ON MECHANICAL PROPERTIES OF TUNGSTEN

T.S. Byun (byunts@ornl.gov), W.D. Lewis, L.L. Snead

OBJECTIVE

The objective of this study is to understand the behavior of tungsten (W) and tungsten materials before and after irradiation and to provide feedback for developing plasma facing materials and components.

SUMMARY

Significant progress has been made in the post-irradiation evaluation (PIE) of the tungsten materials irradiated in HFIR rabbit capsules. Tensile testing and analysis for non-irradiated and low dose irradiated specimens (0.02 and 0.1×10^{25} n/m^2, E>0.1 MeV) were completed, and those for higher doses are underway. Significant radiation-induced hardening and slight reduction of ductility are observed even at the low doses.

PROGRESS

Tensile testing

Test materials include three tungsten materials: single crystal W with [100] orientation, single crystal W with [110] orientation, and 0.5 mm thick W/Cu laminate material. The tensile specimen used in the campaign was the SS-J2 type which has nominal gage section dimensions of 0.5 ×1.2 ×5 mm (4×16 mm outer profile). Tests were performed in a tensile machine at a crosshead speed of 0.05 mm/min by shoulder loading using the cradle grip shown in Figure 29.

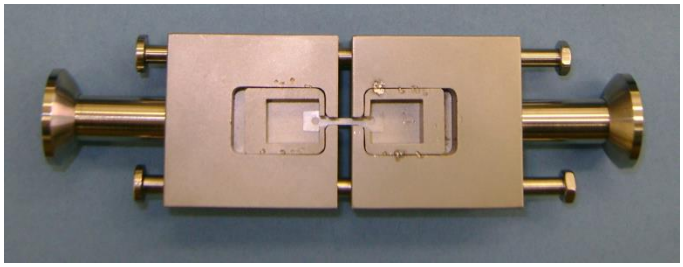

Figure 29. A SS-J2 tensile specimen loaded in the shoulder loading cradle type grip assembly

Baseline tensile tests for non-irradiated tungsten materials were completed: the SS-J2 tensile specimens of two single crystal tungsten materials with [110] and [100] orientations and W/Cu composite were tested at 22, 90, 300, 500, and/or 650 °C. These test temperatures were selected to match the irradiation temperatures. In this year tensile testing was completed for the irradiated specimens from the two lowest dose capsules PC1A and PC2A, for which the doses of W specimens were evaluated to be 0.006 and 0.03 dpa, respectively. Irradiation temperature was about 90 °C with the two PC capsules. Currently, testing is underway for higher dose specimens.

Temperature and dose dependence of tensile behavior

Only the two single crystal W materials were irradiated in the two low-dose capsules and tests were performed at 22, 90, and 300 °C. As seen in Figure 30, the single crystal W with [100] orientation experienced brittle failure at low temperature even without irradiation. This is because the [010] loading direction is unfavorable for dislocation slip. A transition to high ductility occurred between 300 and 500 °C, and the elongation increased to more than 30% at higher temperatures, 500 and 650 °C. In the single crystal W with [110] orientation, the transition to high ductility occurred at slightly lower temperature <300 °C, Figure 31.

Figures 30 and 31 show the effects of neutron irradiation on tensile curves in the [100] and [110] single crystal W. Overall, significant radiation-induced hardening and reduction of ductility are observed even at the low doses of <<1 dpa. Both the tungsten materials after irradiation experienced brittle failure in room and irradiation temperature tests. The specimens with [100] orientation showed a significant reduction of ductility at 300 °C, while those with [110] orientation retained most of its ductility.

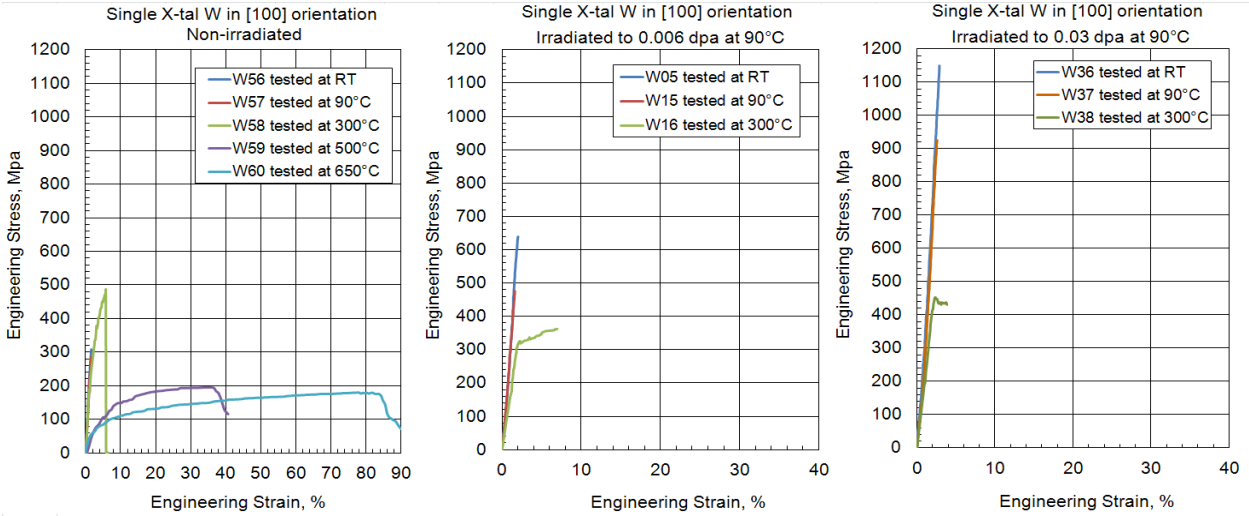

Figure 30. Engineering stress-strain curves for the single crystal W with [100] orientation before and after irradiation

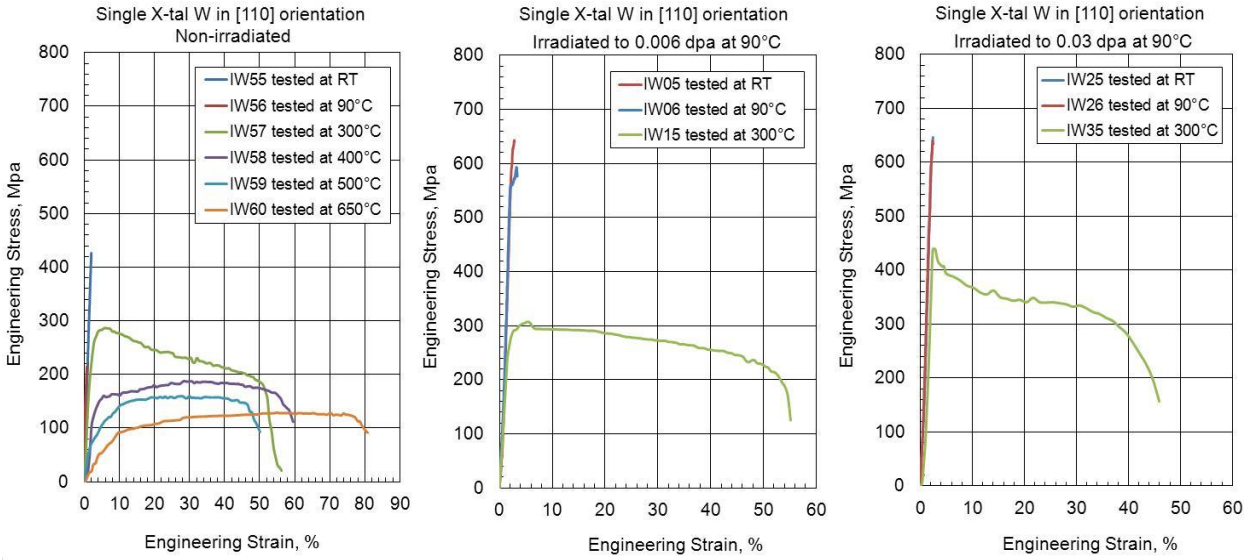

Figure 31. Engineering stress-strain curves for the single crystal W with [110] orientation before and after irradiation

FUTURE PLANS

So far, more than 50% of the tensile tests have been performed for the PIE campaign of the W material specimens from PC, TP, and TC capsules, and test data are being analyzed for those tested specimens. PIE will be continued in FY 2014 and the majority of tensile tests are expected to be completed during the year.

6.3 RADIATION EFFECT ON MICROSTRUCTURAL PROCESSES IN PURE TUNGSTEN

N.A.P. Kiran Kumar (nimishakavia@ornl.gov), T.S. Byun, L.L. Snead

OBJECTIVES AND BACKGROUND

Tungsten is a promising material for fusion application. Its high melting point, high thermal conductivity and high sputtering resistance make it a candidate for plasma facing armor component of fusion reactors. These armor materials are subjected to high level of neutron irradiation. The objective of this work is to understand the tungsten behavior under irradiation and to provide useful information for developing plasma facing materials and components with improved performance.

EXPERIMENTAL

Three kinds of tungsten, 1) single crystal, 2) annealed and 3) deformed (rolled), were selected for neutron irradiation study. The irradiations of these specimens have been completed or are underway in 22 HFIR rabbit capsules to achieve neutron fluences ranging from 0.02 to 20×10^{25} n/m^2 (E>0.1 MeV) at 80 – 100, 300, 500, and 650°C. A focused ion beam (FIB) system with Ga^+ ions beam was used to prepare TEM specimens. In order to minimize the unwanted damage caused by Ga^+ ions, very low energy (2 kV and 27 pA) was used on the TEM specimens during the final thinning process. Neutron irradiation damage on the three kinds of specimens was determined by comparison with the control specimens. Microstructural characterization using transmission electron microscopy (TEM) with an accelerating voltage of 200 kV was performed to evaluate the defects produced by irradiation.

RESULTS AND PROGRESS

Initial microstructural studies were performed on the specimens exposed to doses of a) 0.03 dpa and b) 0.64 dpa at an irradiation temperature of 80-100 °C. Overall structural characteristics with dark spots and dislocation loops were observed in all irradiated specimens (see Figure 1). An increase in damage level with the irradiation dose is noticeable. The loop diameter of the specimens exposed to a dose of 0.03 dpa ranged from 4.4 nm to 5.1 nm (see Table 1). However, in the higher dose (0.64 dpa) specimens, the mean loop size in the deformed sample is 8.1 nm, which is more than the mean loop size in annealed sample exposed to equal dose. The pre-existing dislocation network in the deformed specimens could be the reason for the increase in loop diameter. This observation is in agreement with previous studies which showed that the presence of a pre-existing low network dislocation density would decrease the loop density with a simultaneous increase in loop diameter

In addition, tungsten transmutes to an alloy of rhenium and osmium during exposure to high neutron doses. However, the current specimens are exposed to a dose <1 dpa where the transmutation of W to Re and then Os is negligibly small. EDS analysis confirmed that there was no detectable second phase.

FUTURE PLANS

The HFIR irradiation of higher dose sample will be completed by December 2013. Future efforts will focus on detailed characterization of the neutron irradiated specimens to evaluate the microstructure and correlate to the irradiation induced embrittlement of the tungsten specimens.

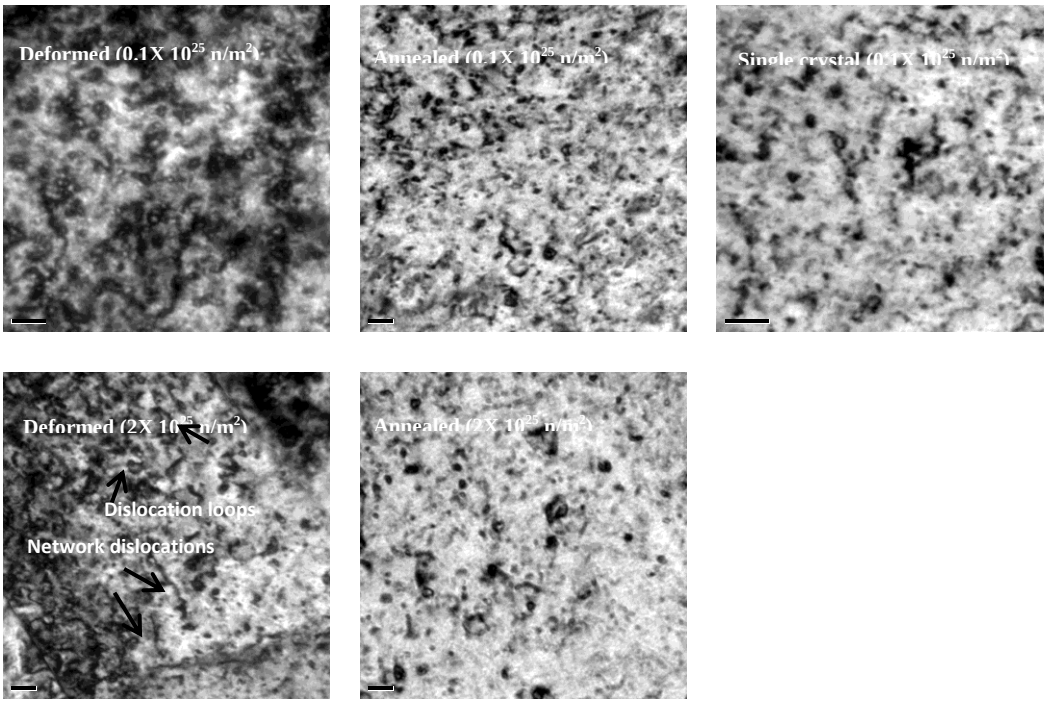

Figure 32: Bright-field (BF) TEM images showing dislocation loops

Table 6: Average loop size in irradiated specimens.

Material	Avg. loop size of the specimens exposed to a dose of 0.03 dpa (in nm)	Avg. loop size of the specimens exposed to a dose of 0.64 dpa (in nm)
Pure W- Deformed	5.07	8.08
Pure W- Annealed	4.38	4.45
Pure W- Single crystal	4.85	N/A

6.4 HIGH-HEAT FLUX TESTING OF IRRADIATED MATERIALS USING PLASMA ARC LAMPS

A.S. Sabau (sabaua@ornl.gov), E. Ohriner, J. Kiggans, Y. Katoh, T.S. Byun and L. Snead

OBJECTIVE

The objective of this work is high-heat flux testing of irradiated materials for plasma facing components and of mock-up divertor components using Plasma Arc Lamps (PAL). This will provide basic materials property information and constitutive equations for materials behavior in the harsh fusion environment.

SUMMARY

A neutron-irradiated tungsten specimen was successfully tested at ITER-relevant high-heat flux conditions using the Plasma Arc Lamp facility at ORNL on Aug. 14, 2013, without any contamination outside the testing box. This ensures the readiness of the new facility for irradiated samples. For thin specimens, as are often used for studies of neutron irradiation effects, one of the main challenges to the PAL systems is the measurement of the sample temperature.

PROGRESS AND STATUS FACILITY DESIGN

The FY13 efforts for enhancing the radiological safety during testing of irradiated specimens included:

- Installation of a water flow meter (0.2-2 gpm) to monitor the variation of coolant flow rate into the cooling rod,
- Installation of an automatic pressure controller – for Ar inlet and outlet - to regulate the pressure to approximately 4 psi in the test section during HHF testing to prevent the liftoff of the main quartz window and escape of radioactive gases.
- Installation of a pressure transducer to monitor the pressure in the test section during testing and identify accidental vacuum leaks during HHF testing.
- In-situ data on coolant flow rate and vacuum pressure in the test section will be acquired for all experiments.

The FY13 efforts for enhancing the temperature measurement during testing of irradiated specimens included:

- Assessment of pyrometer applicability in the actual PAL conditions,
- Use of a second generation molybdenum specimen holder, with four thermocouples
- Calibration experiments involving thermocouples welded to the back of the W specimen.

EXPERIMENTAL, COMPUTATIONAL PROCEDURES, AND RESULTS

First, a calibration run was conducted with a thermocouple welded to the back of a non-irradiated W specimen, providing direct measurement of specimen temperature. For this calibration run, the sample-reflector distance was 2 cm, the incident heat flux was about 3.2 MW/m^2, while the absorbed heat flux into the specimen was approximately 1.6 W/m^2 (50% of the incident heat flux). Two holes were drilled in the 2G Mo holder for inserting thermocouples close to the back surface of the specimen. The placement of thermocouple tips is shown in Figures 33(a) and 34. The pyrometer is aimed at the sample holder side (Figure 33b) at an angle of 34^o to the normal direction to the sample holder surface. The 2G Mo holder has a conical surface and a cutout in order to reduce the heat flux absorbed in the test fixture. The specimen temperature is shown by open circle symbols in Figure 33(b). This data shows an actual increase from room temperature to 1,000 ^oC in the first 2 s. The data shown in Figure 33 indicate the following:

1) The pyrometer data is affected by the infrared energy from the PAL during high-energy pulses. The proof this is an artifact is the sharp rise and drop in pyrometer temperature right at the onset and end of pulses. Further analysis on the pyrometer data at high temperature is needed.
2) The pyrometer data is not affected by the infrared energy during the idle period, after the end of high-energy pulses. The pyrometer temperature at idle shows similar temperature ranges as those measured by thermocouples inserted in the 1G Mo holder.
3) From the data shown in Figure 33b, it is inferred that there would be a temperature difference between that measured by the pyrometer and that by the welded thermocouple on the back of the W specimen of approximately 490 and 400°C, as estimated right when the pulse ended and 0.5 s after the pulse ended (to account for the pyrometer response time of 0.3 s), respectively. On the other hand, there would also be a temperature difference of approximately 553°C between the welded thermocouple and the thermocouple inserted in the open hole, but not welded to the specimen.

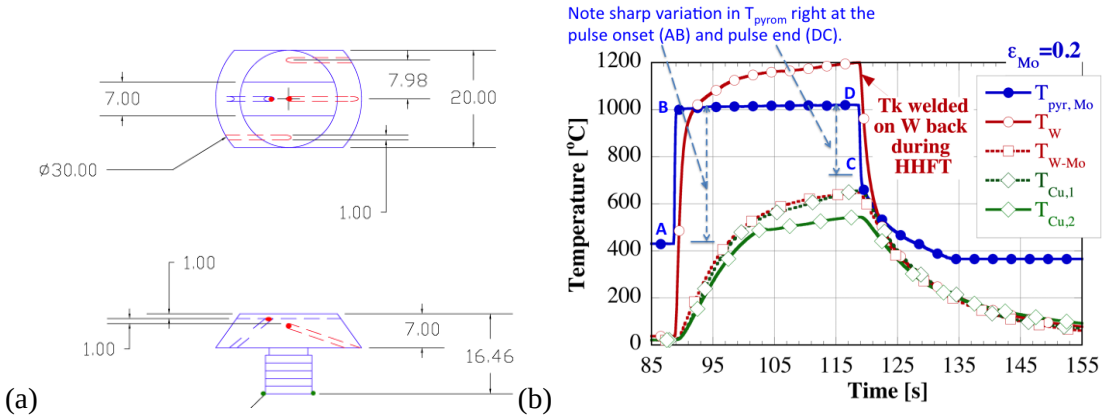

Figure 33. Data on HHFT of an non-irradiated specimen for calibration of sample temperature: (a) 2G Mo specimen holder dimensions (thermocouple tips close to the sample are shown with red dots) (b) Temperature measured by the pyrometer on the side surface of 2G Mo holder ($T_{pyr,Mo}$) thermocouple welded on W specimen back surface during HHFT (T_W), thermocouple between W specimen and Mo holder (T_{W-Mo}), and thermocouples in the cooling rod at the ends of Mo holder thread.

Neutron-irradiated tungsten specimens were successfully tested at ITER-relevant high-heat flux conditions using the Plasma Arc Lamp in August 2013 (Figure 35):

- One irradiated specimen was exposed to 81 pulses and the second one to 200 pulses at 3.3 MW/m^2 incident heat fluxes (1.65 MW/m^2 absorbed), 20 s duration, and 100 s dwell time between pulses.
- No contamination was recorded outside the test box.
- No radioactive gases leaked out of the testing box as the "negative" gauge pressure in the test enclosure was successfully maintained for the entire 4 h duration of the test.

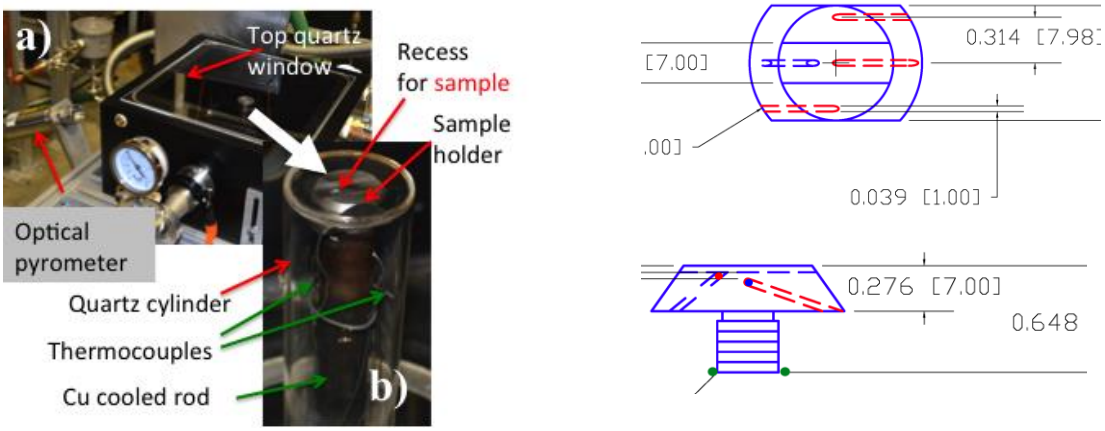

Figure 34. Experimental setup for: (a) the entire test section, (b) specimen holder and cooling rod, and (c) thermocouple placement within the sample holder.

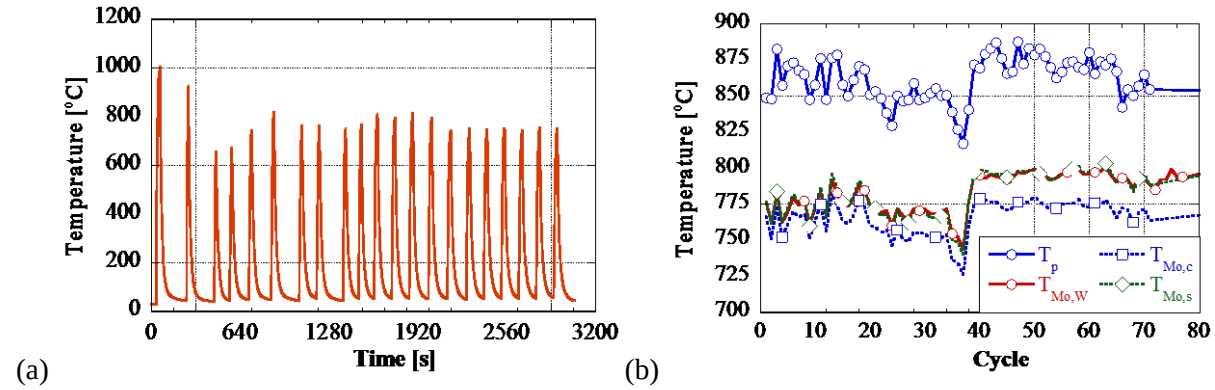

Figure 35. Measured temperatures (a) at W-Mo interface for the first 21 pulses for the first sample and (b) maximum temperature measured by the pyrometer on the side surface of Mo holder (T_p), thermocouple on back surface of W specimen in the open hole ($T_{Mo,W}$), thermocouple in the center of the sample holder ($T_{Mo,c}$), and thermocouple on the side of the sample holder ($T_{Mo,s}$).. Sample temperature was expected to be approximately 1200-1300 °C.

FUTURE EFFORTS

Efforts are now focused on enhancing: (1) safety during testing of irradiated specimens by reducing the footprint of the contaminated area and the level of contamination in the test section, (2) evaluation and control of the specimen temperature, (3) understanding the non-uniform temperature distribution in the sample and sample holder, and (4) extending the duration of high-heat flux test runs. A new cooling rod will be designed and fabricated and a booster pump will increase the water pressure in the cooling rod. The new cooling rod will enable a 3x increase in the coolant flow rate.

For thin samples, the surface temperature cannot be directly measured. Thus, the sample temperature will be evaluated based on a combined experimental/computational procedure involving the measured thermocouple temperatures within the sample holder during testing and pyrometer sample surface temperature during the cooling segment of a calibration run. A third generation Mo specimen holder will be designed with additional thermocouples that will be mounted in contact with the long side of the

specimens, without altering the thermal contact with the Mo holder. The temperatures of the specimen will be evaluated for each Mo holder, with individual holders designed and evaluated to reach and maintain appropriate temperature ranges. The current system pulse duration is limited to 30-40 s by the cooling available to the PAL. A 500 gallon chiller, which is adjacent to the PAL system, will be connected directly to the PAL to extend sustainable PAL pulses to 450 s.

7.0 SPECIAL PURPOSE MATERIALS

7.1 NEUTRON IRRADIATION OF DIELECTRIC MIRRORS

Keith J. Leonard (leonardk@ornl.gov), N.A.P. Kiran Kumar, Gerald E. Jellison Jr., and Lance L. Snead

OBJECTIVE

The goal of this work is to evaluate the upper neutron irradiation dose and temperature limits of two promising dielectric mirror systems. These mirrors are based on alternating high and low refractive index layers of Al_2O_3/SiO_2 and HfO_2/SiO_2 films. The effects of neutron irradiation on optical properties and stability of the film layers are examined along with correlation to microstructural changes.

PROGRESS

Fiscal year 2013 saw progress in establishing the upper neutron irradiation limits of Al_2O_3/SiO_2 and HfO_2/SiO_2 dielectric mirrors along with improved understanding of the failure mechanisms responsible for degradation of reflective properties associated with the neutron dose and post-irradiation annealing. Samples were irradiated at 448 K to 10^{21} and $4x10^{21}$ n/cm^2, E>0.1 MeV, corresponding to approximately 1 and 4 dpa, in HFIR cycle 444, ending on November 3, 2012. Included in the capsules were single layer films of SiO_2, Al_2O_3 and HfO_2 on the same sapphire substrates used for the mirrors. Following irradiation, capsules were transferred to the IMET Laboratory where the outer Rabbit housing was removed to retrieve the inner sample holder containing the mirrors. After a two-month decay period the holders were transferred to LAMDA Laboratory.

The mirrors were unloaded from the specially designed holders in LAMDA with care to minimize any possible damage to the surface of the samples. The mirror samples showed signs of delamination for both the 1 and 4 dpa irradiations, with more extensive damage in the higher dose set. Images of the 4 dpa mirrors are shown in Figure 36.

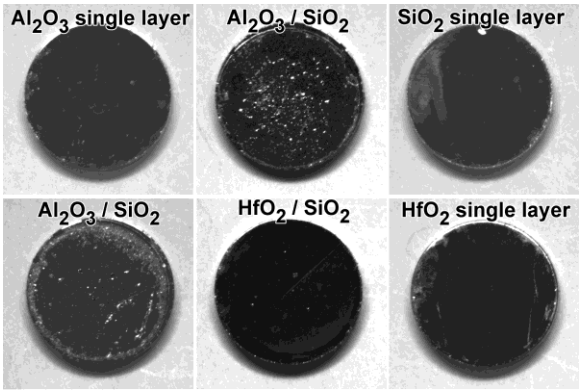

Figure 36. Grayscale images of Al_2O_3/SiO_2 and HfO_2/SiO_2 mirrors and single layer films deposited on sapphire substrates following neutron irradiation to 4 dpa at 448 K.

Post-irradiation optical testing included photospectrometry, ellipsometry and absolute reflectance. Specular reflectance versus wavelength of the 1 and 4 dpa irradiated mirrors was measured by photospectrometry. Due to the small size of the mirrors compared to the diameter and intensity distribution of the incident light source of the photospectrometry, the absolute reflectivity of the mirrors could not be measured accurately or with repeatability. Absolute reflectance measurements were performed using a 248 nm wavelength laser, which the mirrors were designed to reflect. However, since the time that post irradiation examination of the low dose (0.001 to 0.1 dpa) dielectric mirrors were performed, the KrF excimer laser (248 nm wavelength) had become unavailable for irradiated materials examinations. A new deep UV NeCu laser that utilizes similar coaxial gain medium and internal mirrors similar to the common HeNe laser was purchased at a fraction of the cost of the larger more complex excimer laser systems. The deep UV laser produces a wavelength of 248.6 nm with a longer pulse duration compared to the excimer laser, which was favorable for data acquisition. The testing of the new laser was performed during the summer, with the final optical testing of the mirrors performed at the end of FY13.

The photospectrometry reflectance data versus wavelength was normalized to the absolute reflectance data. The results are shown in Figure 37 for the two mirror types, along with select data from the earlier, lower irradiation dose experiments. Both the Al_2O_3/SiO_2 and HfO_2/SiO_2 mirrors showed complete loss in reflectance for the 4 dpa irradiation condition. The Al_2O_3/SiO_2 mirror showed a reduction in reflectance to near 95% at 248 nm. Additionally, the 1 dpa irradiated Al_2O_3/SiO_2 mirror response was much different than that of the lower dose irradiations (0.001 to 0.1 dpa) in that a reduced working range and shift to longer wavelengths was measured. The reflectance of the HfO_2/SiO_2 mirror for the 1 dpa irradiation dropped to below 20%, through little change in the working range or shift in its position were observed relative to the lower irradiation dose results. The shift of the Al_2O_3/SiO_2 mirror to longer wavelengths following 1 dpa may be the result of either the formation of secondary phases at the interfaces between the constituent film layers or the start of film layer crystallization. It was observed that significant Al/Si interdiffusion occurs with irradiation and thermal annealing between the amorphous layers, but both layers show no crystallite formation or secondary phase development in samples irradiated up to 0.1 dpa and in post irradiation annealing to 673 K. The cause of failure for the 1 and 4 dpa HfO_2/SiO_2 mirror are likely an extension of the failures observed in the post-irradiation annealed 0.1 dpa mirror that will be discussed briefly. Microstructural analysis of the higher dose, 1 and 4 dpa, mirrors will be conducted next year.

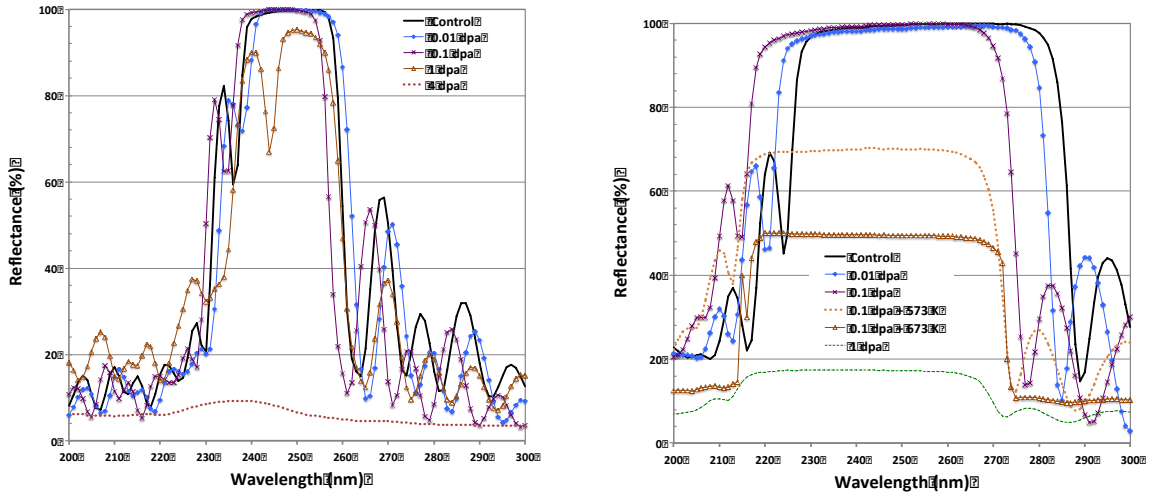

(a) (b)

Figure 37. Photospectrometry results for the (a) Al_2O_3/SiO_2 and (b) HfO_2/SiO_2 mirrors in the unirradiated and select irradiation and post-irradiation annealed conditions. The reflectivity data is normalized based on the absolute reflectivity measurements conducted through direct laser reflectance measurements.

The HfO_2/SiO_2 mirrors showed degradation following post irradiation annealing after 0.1 dpa irradiation, with the loss in reflectance increasing with post irradiation annealing temperature. Detailed examination was performed to determine the cause of reflectance loss and to examine changes in microstructure, with typical results shown in Fig. 38. Irradiation to 0.1 dpa resulted in the formation of a semi-amorphous layer within the sapphire at the interface with the first deposited HfO_2 layer. Its formation may have been aided by both the state of stress at the interface as well as the transfer of oxygen to the HfO_2 layer due to losses in the film as confirmed by the monoclinic to tetragonal transformations observed in the crystallography of the HfO_2 films. On annealing, the HfO_2 film adjacent to the sapphire buckled, with the Al-O amorphous material from the sapphire collecting in the space under the buckled HfO_2 film. This created defects along the length of the film/substrate interface that produces stresses in the film layers during thermal changes in the mirrors as a result of either irradiation at temperature or in post-irradiation annealing. As the defects were limited to first HfO_2 film layer and not enough to contribute to the loss in reflectance, it was the stress created by these defects during thermal changes that resulted in delamination of the film layers in that local region. It was calculated that a minimum critical flaw size of 370 nm was required to generate the delamination failure of the films. The higher degree of delamination, and thus reflectance loss, in the 673 K post-irradiation annealed mirror over that of the 573K annealed mirror was a result of both the increased defect development along the film/substrate interface as well as the larger change in temperature that increased the stress in the films. The amorphization of the interface becomes increasingly detrimental with increasing doses, and explains the film delamination observed in the as irradiated 1 and 4 dpa mirrors. At lower doses, delamination was only observed in the post-irradiation annealed mirror at 0.1 dpa and not at lower displacement doses.

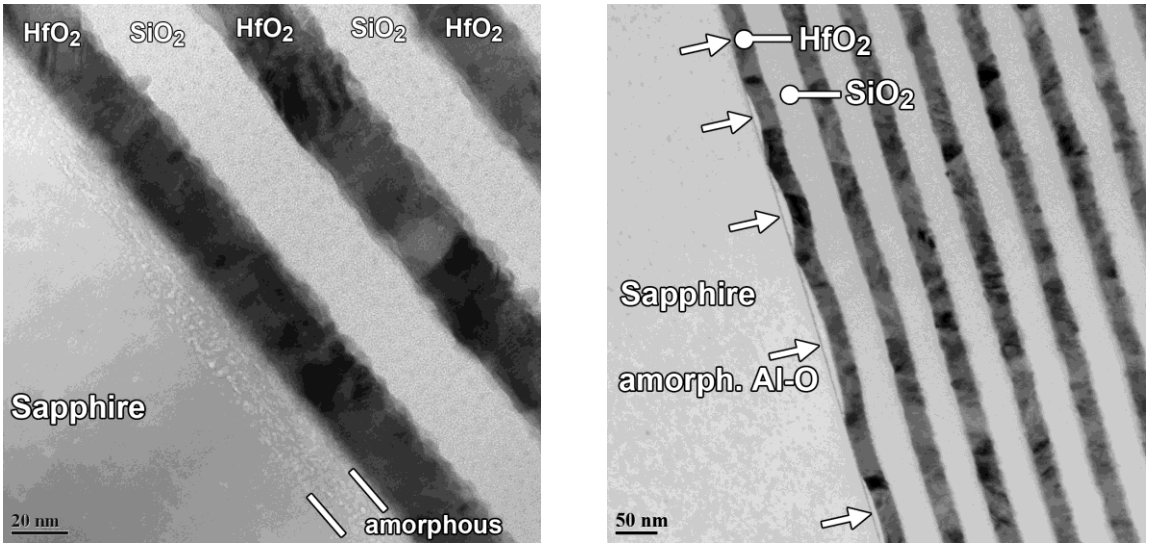

(a) (b)

Figure 38. TEM micrographs of the HfO_2/SiO_2 mirror following (a) 0.1 dpa irradiation at 448 K showing the development of a partially amorphous region within the sapphire substrate and the film interface, and (b) after post-irradiation annealing at 673 K for 1 hour. The annealed sample shows a buckled film layer with amorphous material filling in the space under the HfO_2 film buckle.

FUTURE PLANS

Continuing work will include completion of microstructural analysis of the 1 and 4 dpa mirrors to confirm the causes of delamination. Additional TEM studies will explore changes in Al-O and Si-O bonding in the amorphous film layers in the 0.1 and 1 dpa Al_2O_3/SiO_2 mirrors using electron energy loss spectroscopy in order to understand the limits to Al/Si interdiffusion driven by both irradiation and thermal exposures.

7.2 IRRADIATION RESPONSE OF NEXT GENERATION HIGH TEMPERATURE SUPERCONDUCTORS

Keith J. Leonard (leonardk@ornl.gov), Tolga Aytug, Fred A. List III, Yanwen Zhang (ORNL), Albert A. Gapud, Nathan T. Greenwood (University of South Alabama), Alejandro G. Perez Bergquist, William J. Weber (University of Tennessee), Victor A. Maroni (Argonne National Laboratory)

OBJECTIVE

The goal of this work is to evaluate the irradiation response of select high temperature superconducting (HTS) coated conductors representing different commercial methods of enhanced flux pinning for improved performance under externally applied magnetic fields. Ion beam irradiation was used to examine the effect of irradiation on the different pre-existing flux pinning defect structures, as well as to assess their influence on the superconductors' capability for use in fusion reactor systems.

PROGRESS

Base-line evaluation of the irradiation response of three advanced high temperature superconducting (HTS) tapes was performed. The HTS coated conductors consisted of biaxial textured films (0.74 to 1.45 μm thick) deposited by metal organic deposition techniques onto buffered Ni-alloy tapes. The materials include Zr-doped (Y,Gd)$Ba_2Cu_3O_{7-x}$ (Zr-YBCO) and $GdBa_2Cu_3O_{7-x}$ (GdBCO) films fabricated by SuperPower Inc. (SP), and (Dy,Y)$Ba_2Cu_3O_{7-x}$ (DyBCO) films processed by American Superconductor Corporation (AMSC). The Zr-YBCO and DyBCO conductors were in one meter lengths, with critical current (I_c) values in self-field of 239 and 525 A/cm-width, respectively. The samples were cut into smaller samples for testing. The GdBCO tape was received as pre-cut test samples of approximately 1 inch long. Patterned current bridges were laser scribed into the HTS test samples for electrical characterization to accommodate the high current samples in the available measurement equipment.

Ion irradiation of the HTS materials performed at the University of Tennessee Ion Beam Materials Laboratory with 5 MeV Ni and 25 MeV Au ions to simulate the effects of cascade damage during neutron irradiation. The dose and implantation depths were calculated by TRIM code prior to irradiation. Electron energy loss, S_e, of the Ni and Au ions was 1.8 and 6 keV/nm, respectively, below the 20 keV/nm threshold energy for columnar defect formation. Ion irradiation was conducted at room temperature in a direction parallel to the tape normal with fluences of 10^{11} to 10^{12} cm^{-2} for 25 MeV Au ions, producing 0.002 and 0.02 dpa, and with $5.5x10^{11}$ cm^{-2} for 5 MeV Ni ions producing 0.003 dpa. The ion implantation range in all cases was beyond the conductor and buffer layers into the Ni-alloy substrate.

The three HTS conductors have unique microstructures that resulted in distinct irradiation properties and responses. A summary of the HTS conductors and their unique features is provided in Table 7. Examples of the changes in microstructure for each of the three HTS materials after 25 MeV Au ion irradiation to 10^{12} i/cm^2 are shown in Figure 39. The Zr-YBCO and DyBCO conductors utilize secondary phase particles of $BaZrO_3$ (BZO) and $(Dy,Y)_2O_3$, respectively, as strong flux pinning centers in addition to commonly observed native defects such as dislocations, grain boundaries, stacking faults, and anti-phase boundaries. The BZO particles are oriented in the c-axis direction in the YBCO matrix that provides increased pinning for fields oriented parallel to the *c*-axis (H//c), while the random distribution of $(Dy,Y)_2O_3$ generally produces improved properties for H//ab. On the other hand, for the $Gd_2Ba_2Cu_3O_{7-x}$ (GdBCO) films, the primary source of pinning is planar intergrowths, along with the crystal basal-plane aligned, fluorite-like Gd_2O_3 precipitates.

Table 7. High temperature superconductors, substrate architecture (listed by company name from which tapes were fabricated) and the type of flux pinning created for improved use in magnetic field applications.

Material	Substrate	Features
$(Dy,Y)Ba_2Cu_3O_{7-x}$	American Superconductor	50% substitution of Y in $YBa_2Cu_3O_{7-x}$ chemistry. Development of $(Dy,Y)_2O_3$ nanoparticles, enhanced H//ab pinning. Increased stacking faults ($YBa_2Cu_4O_8$ intergrowths) in the film.
$GdBa_2Cu_3O_{7-x}$	SuperPower	Substitution of Gd for Y in the $YBa_2Cu_3O_{7-x}$ chemistry. High density stacking fault generation from mismatch in growth domains from buffer and Gd_2O_3 particles, yielding improvements in H//ab pinning.
Zr-doped $(Y,Gd)Ba_2Cu_3O_{7-x}$	SuperPower	Creation of $BaZrO_3$ nanodots aligned along the c-axis direction, producing enhanced H//c pinning.

A significant change in the size and distribution of the BZO particles was observed following irradiation of the Zr-YBCO conductor with 25 MeV Au ions to 10^{11} cm^2, in which the length of the c-axis oriented chains of BZO particles is dramatically reduced, by as much as 25% in the c-axis direction. The width of the BZO particles is relatively unchanged and averages 8 nm. Another immediately observed change is the increase in faults at the interface of the BZO particle, which are believed to be responsible for the increase in H//ab pinning up to 0.003 dpa (Figure 40a).

While no changes were measured in the size and distribution of the $(Dy,Y)_2O_3$ particles in the DyBCO conductor with irradiation up to 0.02 dpa, the microstructure did show the appearance of small defect structures in the conductor matrix. This was only observed in the high fluence, 10^{12} i/cm^2 (0.02 dpa), 25 MeV Au irradiations. The irradiation induced defects also appeared in the GdBCO conductor under the same conditions. These defects were only on the order of a couple of nanometers and consisted of localized lattice disorder in the atomic stacking sequence of the conductor. However, the strain within the GdBCO and DyBCO lattice from these defects produce lobe-type diffraction contrast that makes these defects easily visible at lower magnifications. The Gd_2O_3 particles in the GdBCO conductor also disappear following 25 MeV Au irradiation to 0.02 dpa.

Shown in Figure 40a is the field-orientation dependence of the critical current (I_c) at 1 Tesla and 77 K for the 5 MeV Ni and the 25 MeV Au irradiations conducted on the three HTS materials. For irradiation at lower dpa with Au and Ni ions, both the DyBCO and to a lesser extent GdBCO conductor showed a decrease in pinning in the H//ab condition, while an improvement in the ab-pinning is observed for the Zr-YBCO films. This is correlated to the changing size, distribution and type of intergrowths in the three conductors. The decreased H//ab values in the DyBCO conductor are offset by I_c increases over other angular directions resulting in substantially decreased anisotropy in I_c, a positive effect for conductor utilization in varying magnetic field orientations.

Irradiation of the HTS materials with 25 MeV Au ions to 10^{12} cm^{-2} produced a further suppression of the measured I_c values, with the least reduction in the Zr-YBCO conductor. The samples still remained superconducting and showed only modest reductions in T_c. Data for the 25 MeV Au irradiation of the DyBCO material to 0.02 dpa was from a second batch of material with slightly different unirradiated properties, but represents the decrease in transport properties with this level of irradiation.

While the dpa values are relatively low, all superconductors have a much lower exposure limit than do structural materials. However, in comparison of irradiation properties to earlier generation YBCO conductors as well as single crystal and bulk samples of those materials, the HTS materials of this study show improved resistance to irradiation induced changes in electrical properties.

The dependence of T_c on dpa illustrates the reduced sensitivity of the conductors to irradiation. The reduction in T_c has been identified as a consequence of displacement reactions changing the hole carrier concentration in the Cu-O chains of the HTS structure, which are the most unstable sites due to the lightly bound oxygen atoms. As oxygen-deficient and highly disordered regions are created with decreasing hole concentrations, degradation in T_c is observed. While increased recombination rates associated with room temperature irradiation may in part contribute to the measured stability, the reduction in T_c in this study is less than those of other room temperature irradiated HTS materials.

The increased defect mobility at higher irradiation temperatures may result in subsequent cascade collapse and less flux pinning in the conductor, which is observed in the transport data for the high dose 25 MeV Au ion irradiations. This may account for the appearance of the radiation-induced defect structures in the HTS materials, compared to the amorphous regions typically observed in neutron and ion irradiation studies on YBCO at lower temperatures.

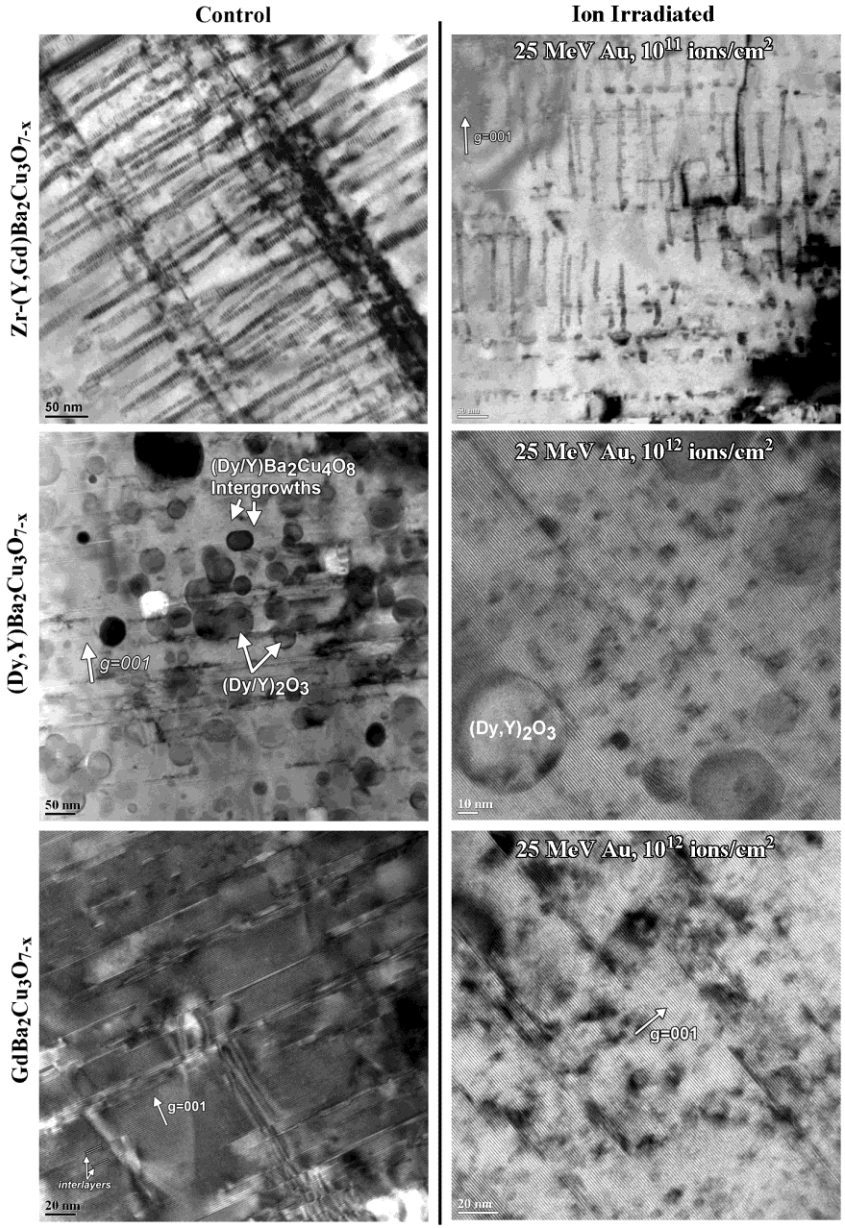

Figure 39. Comparison of the 25 MeV Au irradiated microstructures to that of the as-received condition.

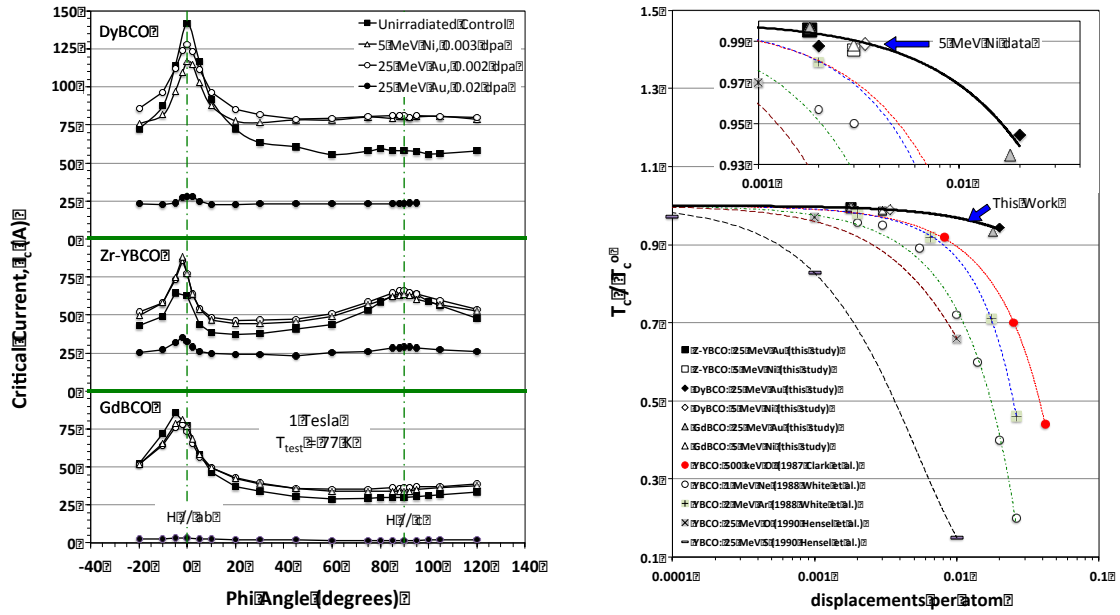

(a) (b)

Figure 40. (a) Changes in the angular field dependency of I_c at 1 Tesla and 77 K following 5 MeV Ni and 25MeV Au ion irradiations. (b) Change in T_c from initial values (T_c^o) as a function of displacement dose for ion irradiated HTS samples

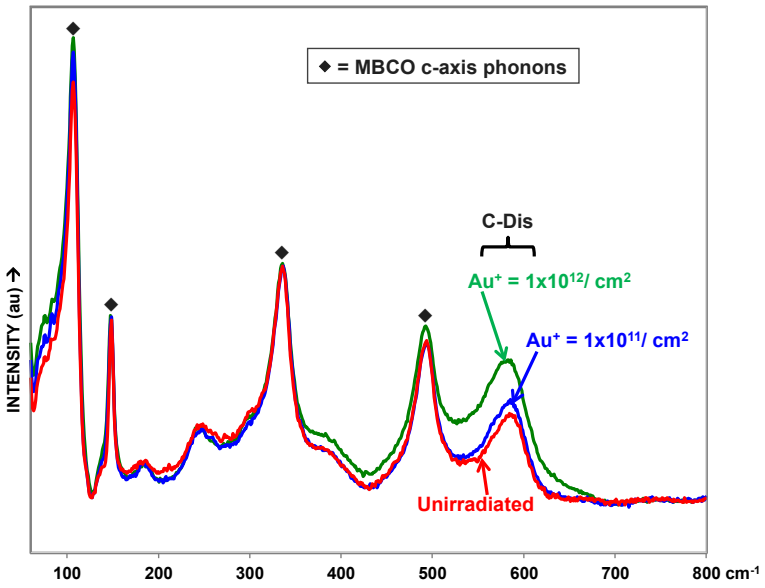

Figure 41. Averaged Raman spectra of 25 MeV Au irradiated samples. The spectra were extrapolated to a horizontal baseline and normalized to the 336 cm-1 band of MBCO c-axis phonon peak.

The most recent work performed in the last month of FY13 on the HTS conductors is characterization of the 25 MeV Au irradiated DyBCO samples by Raman spectroscopy. A comparison of the averaged Raman spectra taken from 30 spectra each of the control, 10^{11} and 10^{12} cm^{-2} 25 MeV Au irradiated samples using 633 nm excitation is show in Figure 41. The only difference observed is in the spectral region of the cation disorder mode. This mode increases slightly in intensity for the 10^{11} cm^{-2} irradiation compared to that of the control, but is increases considerably for the higher dose irradiation. This matches well with both the electrical properties that show a loss in I_c at these levels, and the appearance of both defect structures in the lattice as well as the changes in the type of the intergrowths in the material. For the latter this suggests changes in the Ba-Cu chemical ordering more than that of the Cu-O type, which is observed by TEM in the types of intergrowth present following irradiation. Furthermore, the cation disorder may also account for the reduced sensitivity of T_c, which is strongly linked to oxygen deficiency.

FUTURE PLANS

Continuing work will concentrate on examining the low temperature ion irradiation response of the HTS conductors through modification of the ion irradiation holder to allow basic *in situ* measurements of self-field properties during irradiation. Potential neutron irradiation testing may also be conducted to provide comparison to the characterized ion irradiated samples. Further characterization of the materials through Raman and advanced TEM techniques is also planned.

8.0 COMPUTATIONAL MATERIALS SCIENCE

8.1 STRENGTHENING DUE TO HARD OBSTACLES IN FE AND FERRITIC ALLOYS

Yury Osetskiy (osetskiyyn@ornl.gov) and Roger E. Stoller

The objective of this research is to investigate the primary features of strengthening mechanisms associated with ODS materials. Due to the lack of interatomic interaction potentials for an ODS alloy, we approximate the oxide particles as inclusions with a very high shear modulus. This simulates a very hard obstacle. An extensive modeling program using molecular dynamics simulations is in progress. The aim is to fully characterize the mechanisms involved in dislocation – obstacle interactions; a few qualitative results have been obtained during FY 2013.

A wide range of environmental and microstructural parameters was investigated. In particular, we simulated rigid obstacles from 1 to 6 nm in diameter over the temperature range from 100 to 600 K interacting with an edge dislocation moving at speed from ~1 m/s to 100 m/s under the applied strain rate from 10^6 s^{-1} to 10^8 s^{-1}. An example of the simulation model is presented in Figure 42, which also illustrates the differences in particle morphology (i.e. aspect ratio) that are being examined. A box of ~7 to$10x10^6$ Fe atoms in bcc lattice contains an edge dislocation ½<111(110) and a spherical or elongated inclusion. An inclusion consists of Fe atoms coherent with the surrounding matrix and interacting with matrix atoms by the same interatomic potential as matrix-matrix atoms, however atoms inside the inclusion do not move relatively to each other. This represents an absolutely rigid precipitate which however can move inside matrix as a super-atom of the corresponding mass and it is included in the total system of motion equations for the whole crystal.

First, we have emphasized the role of edge dislocations in strengthening materials with nanosized obstacles such as ODS materials. It is known that plasticity of the majority of bcc metals and alloys is controlled by screw dislocations. The reason of this is a huge difference in the value of the Peierls stress, σ_P, for screw and edge dislocations. For example, in Fe σ_P ~30-80 MPa for an edge dislocation while that for a screw is ~2000 MPa. Therefore during deformation edge dislocations are usually removed from the bulk in the initial stages and most of the plasticity is controlled by screw dislocations. However, depending on the inclusion density and size distribution, the opposite case can occur in particular alloys. Thus in materials with a high concentration of small hard obstacles such as ODS alloys, the edge dislocations should be strongly pinned by rigid obstacles while screw dislocations can overcome them by cross-slip. In this case, plastic deformation is controlled by the inclusion interaction with edge dislocations.

The most important result we have obtained is the dependence of the interaction mechanisms on the rigid obstacle size. Very small rigid inclusions, ≤ 1 nm, are very weak obstacles for edge dislocations. It is interesting that a rigid obstacle of this size is weaker than the equivalent void or equilibrium He-bubble. On the contrary, large obstacles, ≥4-5 nm, are the strongest and the interaction mechanism is the classical Orowan mechanism, which provides the maximum possible obstacle strength. The subsequent interaction between the Orowan shear loops (left after the first dislocation passes) and additional dislocations may also affect the total strengthening and this is currently under investigation. An intermediate mechanism for inclusions of sizes between 1 and 4 nm was found to be strongly dependent on the position of the dislocation slip plane and the obstacle equator. This interaction is no longer symmetric with respect to the equator as was found earlier for many other obstacles such as voids, bubbles and soft precipitates. If the slip plane is above the equator the rigid obstacle strength decreases significantly while in the opposite case the rigid obstacle strength is increased. Atomic-scale details of all these mechanisms were studied within the modeling program.

Currently we are working on a modification of the dispersed barrier hardening model where we will include not only obstacle size and density but also their size dependent strengthening mechanisms. This will allow a better understanding and predicting of mechanical property changes in systems where the obstacle size distribution and type are known. In the near future this also can be combined with our results on the effects of temperature on interaction mechanisms and strength.

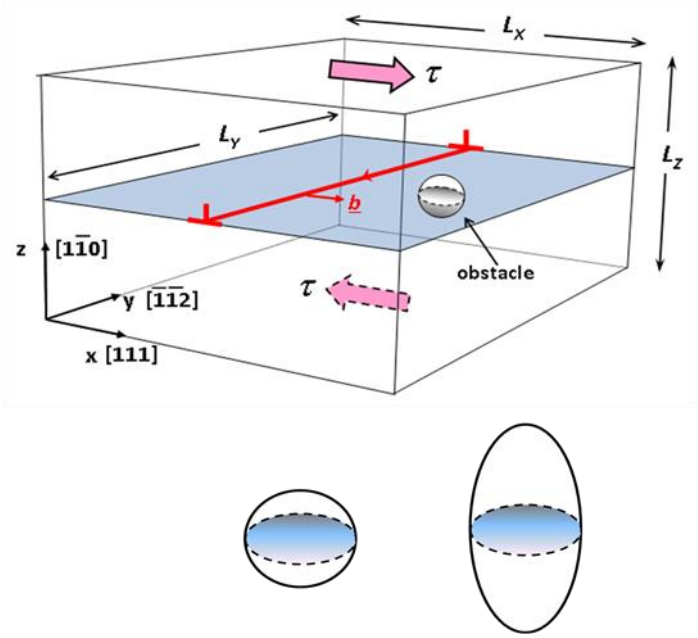

Figure 42. Schematic setup of the simulation system used to model dislocation-inclusion interactions; both spherical and elongated particles with different radii are included.

8.2 MOLECULAR DYNAMICS STUDY OF HE-BUBBLE EQUATION OF STATE

Yury Osetskiy (osetskiyyn@ornl.gov) and Roger E. Stoller

The objective of this research is to investigate the behavior of helium in radiation-induced bubbles, with the goal of obtaining an improved He equation of state. Such bubbles have a significant impact on the evolution of microstructures and mechanical properties under irradiation.

An extensive program of molecular dynamics simulations nearing completion has been investigating He-filled bubbles to determine the pressure-volume relationship (equation of state) for He inside bubbles. This is absolutely necessary for predicting radiation damage evolution in fusion materials where He is generated due to transmutation reactions. The presence of He influences all microstructural processes since the evolution of He-filled bubbles can dramatically change the balance of point defect reactions and their kinetics.

We are studying bubbles with radii from 0.25 to 5.0 nm with He-to-vacancy ratios from 0.1 to 2.0 over the temperature range 300-1000 K. The three-body angular dependent He-Fe interatomic potential developed earlier at ORNL was used in this study. A special study was made to define the equilibrium state of gas-filled bubbles. We recently have adopted a criterion which is based on estimation of the average pressure in the matrix system: we define a bubble as being in equilibrium if the volume is the same as the original volume of the corresponding number of vacancies defined in the perfect lattice and therefore does not produce additional pressure on the matrix. Calculation of the total pressure in the system is fast and the average value converges well because of the large number of atoms used in practical modeling.

A particular problem in this kind of study is related to small bubbles, <0.5 nm, due to limitations in the statistical definition of thermodynamic parameters such as gas temperature and pressure in small systems with few atoms. The smallest bubble we studied may contain as few as one He atom and estimation of He temperature inside such a bubble becomes an unsolvable problem. A 0.25 nm bubble occupies only 9 lattice sites and with the equilibrium He-to-vacancy ratio $r_0 \sim 2$ at 300 K contains only 18 He-atoms. Accumulation of enough collisions between He atoms inside the bubble and Fe atoms on the interface become a real statistical problem. On the contrary, a 5 nm bubble occupies 44,399 lattice sites and at r_0 ~0.35 at 300 K contains 15,540 He atoms. See Fig. 43a and b for a comparison of the smallest and largest bubbles studied at the lowest and highest applied temperatures. Statistical variations lead to a quite strong dependence of the accuracy in estimating the equilibrium pressure inside He-bubbles of different sizes, He content and temperature. We have carried out extensive modeling to identify where the molecular dynamics results are accurate enough. So far we equilibrated large bubbles (>0.5 nm) over 6×10^5 time steps and small ones (<0.5 nm) over a million steps at each particular set of conditions. This is equivalent to the physical time equal to 0.3 and 0.5 ns, respectively. Examples of the equilibration process, showing the variation of He pressure inside the bubbles as a function of time, are presented in the Figs. 43a and b for small and large bubbles at the low and high temperatures, respectively. It can be seen that pressure in the large bubble equilibrates smoothly although even 0.3 ns appears to be too short a time to reach complete equilibrium. In contrast, pressure in the small bubble shows very large fluctuations and does not demonstrate convergence to the equilibrium state.

We concluded that even the maximum time used so far for modeling, 0.5 ns, is not enough for the smallest bubble studied, 0.25 nm. Systematic modeling of many cases with longer time is too computational time consuming. We therefore expect to estimate parameters as close as possible to equilibrium and run them for as long as possible time to get results with adequate accuracy.

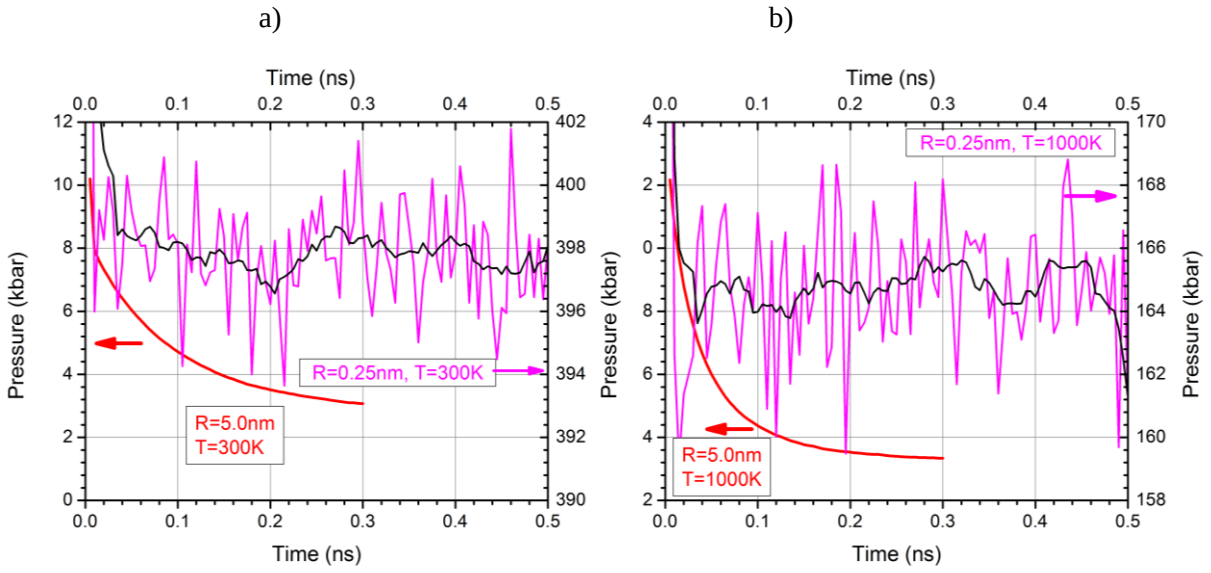

Figure 43. Dependence of He pressure inside 0.25 and 5.0 nm bubbles during equilibration at a) 300 K and b) 1000 K. Red and pink lines connect points averaged over 5 ps while the black line is for 50 ps.

8.3 MOLECULAR DYNAMICS MODELING OF ATOMIC DISPLACEMENT CASCADES IN 3C-SIC

G. D. Samolyuk (samolyukgd@ornl.gov), Y. N. Osetskiy and R. E. Stoller

The purpose of this work is to develop a basic understanding of defect formation and evolution in SiC. We have shown that the popular SiC interatomic potentials, Tersoff, and modified embedded atom method (MEAM), significantly overestimate the barrier for vacancy-interstitial recombination. In order to demonstrate the impact of the recombination barrier value on cascade defect formation, we are carrying out cascade simulations with the newer Gao-Weber (GW) potential.

The GW potential code was introduced in the LAMMS molecular dynamics (MD) package, and good agreement was found between MD and first-principles calculated formation energies of the twelve most typical defects. We joined the GW potential with the well-established Ziegler, Biersack and Littmark (ZBL) potential at 0.95 Å to stiffen the pair repulsion at small atomic separation distances.

Simulations with 10 keV Si primary knock on atoms have been executed. The simulation cell contains 80x80x80 unit cells (409,600 atoms). Point defects in SiC consist of interstitials (I) and vacancies (V) of both carbon and silicon, as well as antisite defects of C on a Si site (C_{Si}) and Si on a C site (Si_C). The carbon defects predominate as shown by the green and purple symbols in Fig. 43.This result is qualitatively similar to that obtained with Tersoff potential (Fig. 44a). However, in contrast to the simulations with the Tersoff potential, the GW potential (Fig. 44b) produces almost twice as many C vacancies and interstitials at the time of maximum disorder (~0.2 ps) but only about 25% more stable defects at the end of the simulation. As a result the ratio of peak-to-stable defects is much higher for the GW potential. This result is more similar to that observed in metals and oxides. Only about 20% of the carbon defects produced with the Tersoff potential recombine during the in-cascade annealing phase, while about 50% recombine with the GW potential.

On the basis of these result we can conclude that the more accurate recombination barrier in the GW potential gives a much more realistic description of cascade dynamics in SiC and we will use this potential in our continuing work. The results for cluster size distribution at the end of simulation for both potential are presented in Fig. 45. In our analysis we defined a group of point defects as a linked cluster if any of them are connected by the distance less than the lattice parameter. Both simulations produce a significant amount of pair clusters and ~ 75 % of these clusters correspond to the same atom type I-V pair. However if in the case of Tersoff potential all I-V pair clusters correspond to carbon atoms, in the case of GW potential a significant part of these clusters corresponds to silicon. Another difference corresponds to large size cluster distributions. Thus in the case of the Tersoff potential (Fig. 45a) there are only two relatively large clusters containing 19 and 21 defects, in the case of the GW potential there are four clusters of size 21, 30, 35 and 51 defects. These large size clusters could be discussed as potential candidates for forming an amorphisation region. One of these clusters containing 51 defects is presented in Fig. 46, where carbon defects predominate as shown by the green and purple symbols. The full analysis of the cluster structure is in progress.

In the next three months we are planning to increase the statistics of the simulations of cascades in SiC using the GW potential and different temperatures and pka energies in order to further assess the impact of the recombination barrier on stable defect formation. This will provide greater insight that can be used to correct the current generation of interatomic potentials for SiC.

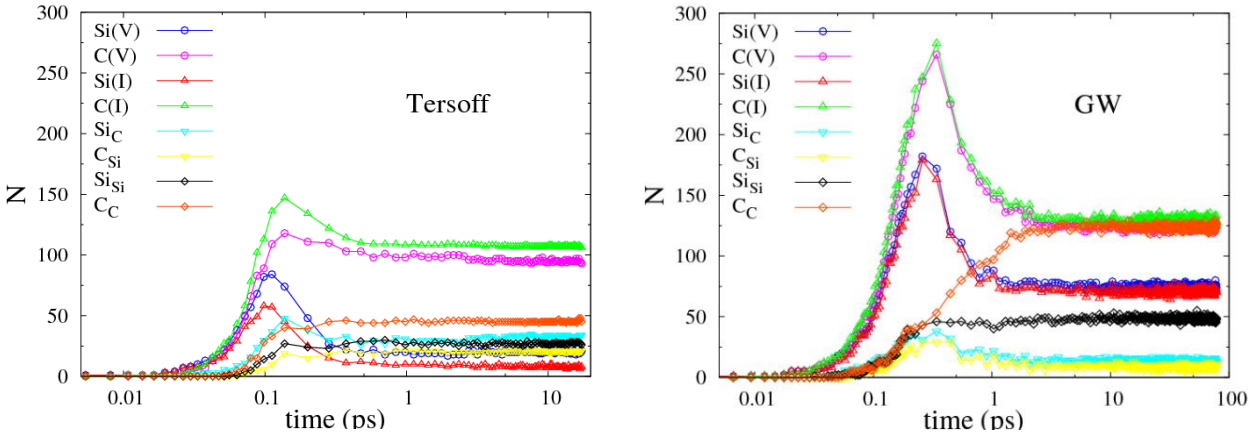

Figure 44. Time dependence of the number of point defects observed in MD displacement cascade simulations 10 keV pka at 300 K: (a) Tersoff potential, (b) GW potential.

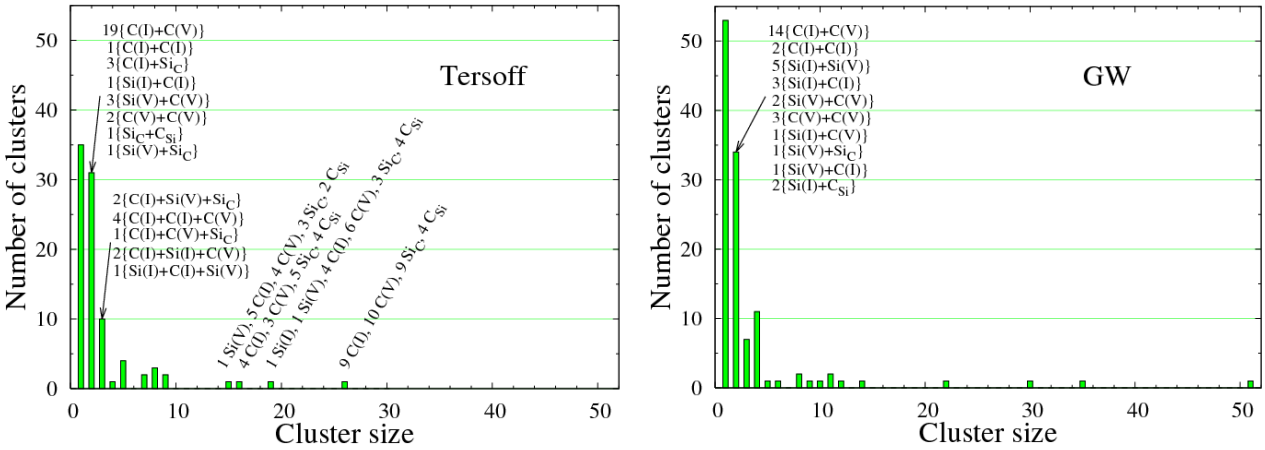

Figure 45. Cluster size distribution at the end of 10 keV Si recoil event in SiC at 300 K: (a) Tersoff potential, (b) GW potential.

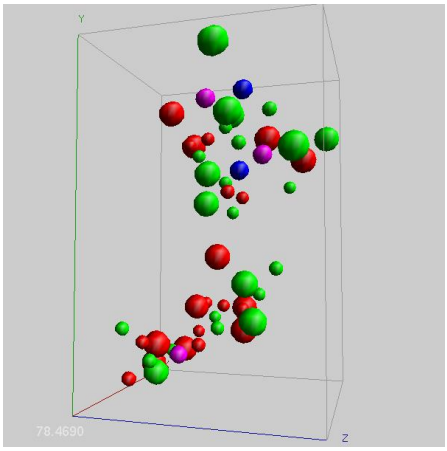

Figure 46. Carbon (green) and silicon (red) interstitials (large spheres) and vacancies (small spheres) at the end of 10 keV Si recoil event in SiC. Blue and purples spheres correspond to Si_C and C_{Si} antisites, respectively.

9.0 - TITAN AND PHENIX COLLABORATIONS WITH JAPAN

Y. Katoh (katohy@ornl.gov), L.L. Snead

SUMMARY

ORNL participates in two major, long-running collaborations with Japan and several less formal collaborations. The collaboration projects with the National Institute for Fusion Science (NIFS) and the participating universities in Japan and the Japan Atomic Energy Agency continued to be the primary international collaboration programs involving the ORNL fusion materials program. The TITAN (Tritium, Irradiation and Thermofluid for America and Nippon) project involving scientists at NIFS and Japanese Universities completed its six-year performance period in March 2013. The succeeding PHENIX (Technological Assessment of Plasma Facing Components for DEMO Reactors) project started in April 2013 with a new focus on tungsten-based divertor components. Activities and achievements of the TITAN and PHENIX collaborations are briefly summarized below. Progress in the collaboration with JAEA is included in section 4.3. Since these activities are integrated with other elements of ORNL programs, the details of meetings, capsule irradiations, etc. are reported in other sections, and are not always identified as related to the collaborations.

PROGRESS AND STATUS

TITAN Project

The objective of the TITAN Project was to obtain the fundamental understanding needed for establishing tritium and thermofluid control in fusion systems, based on experiments under simulated fusion conditions. The results will be applied through the integrated modeling to advancement of design for tritium and thermal energy control in magnetic and inertial fusion energy systems. The project consisted of three tasks: 1 - Transport Phenomena, 2 - Irradiation Synergism, and 3 - System Integration Modeling. Task 1 involved Idaho National Laboratory (INL), University of California, Los Angeles (UCLA), and University of California, San Diego (UCSD) as the U.S. participating organizations. Task 2 was led by ORNL with limited contribution from INL. Task 3 conducted at Sandia National Laboratory (SNL). ORNL played leading roles in Task 2-2, Joining and Coating Integrity, Task 2-3, Dynamic Deformation of Fusion Materials, and a supporting role in Task 2-1, Irradiation-Tritium Synergism.

The objective of Task 2-2 was to develop and examine irradiation performance of joints and coatings of fusion materials. In FY 2013, ORNL successfully completed irradiation of a large number of rabbit capsules containing test specimens of tungsten-coated steels, welded steels, tungsten, and laminated

tungsten composites in HFIR. The tungsten and its composite test specimens will be utilized in the succeeding PHENIX project. Silicon carbide ceramic joints were also developed and evaluated, demonstrating the first radiation-tolerant joining technologies for SiC.

The goal of Task 2-3 on Dynamic Deformation was to acquire fundamental understanding of the dynamic behavior of blanket materials under stress in fusion-relevant conditions. Completion of the Phase-I (low dose stress-relaxation) experimental program of stress effects on dimensional stability of fusion materials, Phase-II program to experimentally determine the irradiation creep behavior of SiC ceramics beyond the initial transient regime and the Phase-III program to develop a bellows-loaded tensile creep rabbit vehicle successfully achieved the initial objectives.

A series of articles reviewing the outcomes of the TITAN project had been prepared and published in a special issue of the journal Materials Transactions, (Volume 54, Issue 4, March 25, 2013).

PHENIX Collaboration

The PHENIX collaboration, or the US – Japan Fusion Research Collaboration / Joint Project on Technological Assessment of Plasma Facing Components for DEMO Reactors, started in April 2013 and is planned to end in March 2019. The goal is to clarify the engineering and science issues for plasma-facing components (PFCs) under fusion divertor conditions, including: a) heat transfer, b) mechanical properties, c) neutron irradiation effects, and d) tritium retention and permeation. Advancement of understanding of these issues is essential for the timely design of PFCs for a DEMO reactor.

In the PHENIX project, the technical focus is on the helium gas-cooled divertor with tungsten-based material armor because of various attractive features of the concept, including safety. The main research subjects are (1) heat transfer in He-cooled systems, improvement of cooling efficiency, and possibly including heat transfer in liquid metal cooling systems (LiPb) as an advanced concept, (2) the response of tungsten layered materials and advanced tungsten materials under complex (steady-state and pulsed) heat loads, (3) thermo-mechanical properties of tungsten, layered tungsten composites, and other advanced tungsten materials after neutron irradiation at high temperatures relevant to divertor conditions, (4) effects of high flux plasma exposure on tritium transfer in neutron-irradiated advanced tungsten-based materials, and (5) feasibility (under ~10 MW/m^2 heat load with irradiation with plasma and neutrons) and safety (tritium retention and permeation) in PFCs and clarification of critical issues for DEMO divertor design.

To reach these goals, research will be conducted in three technical tasks: Task 1 – Heat flow response in PFCs, Task 2 – Material properties and neutron irradiation effects, and Task 3 - Tritium behavior in tungsten at high temperatures. The key experimental facilities to be used for the three tasks are 1 - Plasma Arc Lamp (PAL) high heat flux test facility at ORNL, 2 - HFIR at ORNL, and 3 - Tritium Plasma Experiment (TPE) at INL. The roles of the three technical tasks in advancing divertor technology are illustrated in Figure 47.

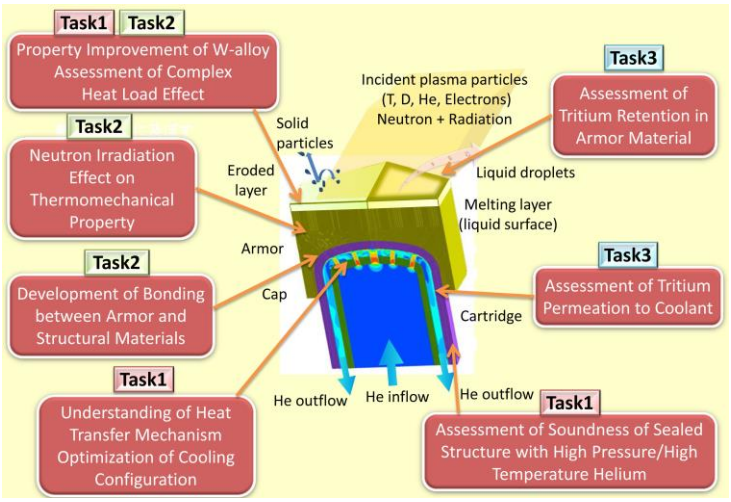

Figure 47. Roles of three PHENIX technical tasks in advancing the helium-cooled, tungsten-based divertor technology for fusion DEMO devices.

The outline of the six-year research plans for individual tasks, more detailed technical plans for the first project year including the schedules for personnel exchanges and technical workshops were agreed to at the First PHENIX Steering Committee Meeting, held at ORNL in February 2013. Follow-up planning workshops for Task 1 at Georgia Institute of Technology (March 2013) and for all tasks at ORNL (July 2013) more completely defined the technical plans.

FUTURE PLANS

Increased technical activities are anticipated after the transfer of initial Japanese research funding for PHENIX in early FY14. This will include the high heat flux testing of neutron-irradiated tungsten test specimens at the ORNL PAL high heat flux facility and conceptual design activity for the new HFIR vehicle for the proposed new neutron irradiation experiment.

10. MATERIALS ENGINEERING IN SUPPORT OF THE ARIES PROGRAM

Arthur Rowcliffe (art.rowcliffe@gmail.com), Lance Snead, Steve Zinkle and Bill Wiffen

10.1 MATERIALS FOR THE VACUUM VESSEL

The vacuum vessel is a safety-class component designed to confine tritium and radioactivity and limit public/worker radiation exposure during accidents while providing a high level vacuum environment for the lifetime of the plant. As conceived in the present study, the vacuum vessel is a robust double- walled ribbed structure which is helium cooled and operates in the 400-500^{o}C regime. (Fig. 48) It is not required to provide mechanical support for other components neither is it required to provide shielding for the magnets. The vacuum vessel is designed to operate in the 400-500^{o}C temperature regime in order to, a) avoid the issues related to radiation hardening-induced changes in fracture toughness and DBTT shifts and b) minimize problems with tritium inventory.

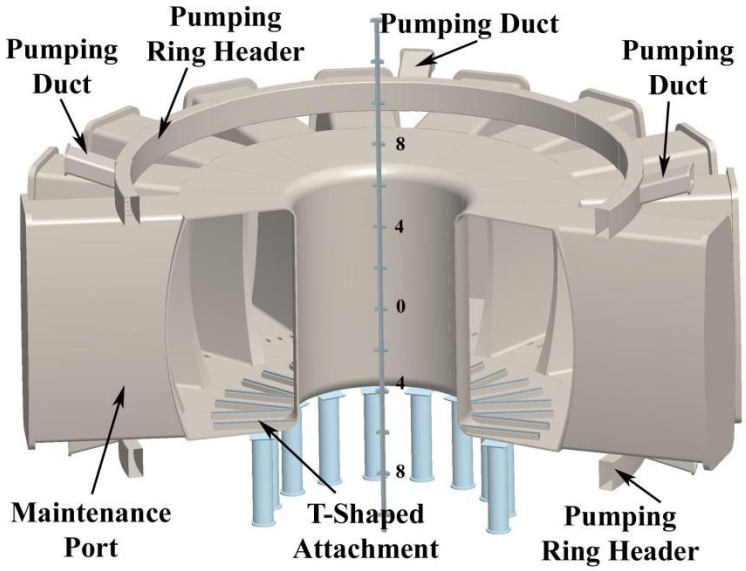

Figure 48. Schematic view of the ARIES-ACT1 vacuum vessel showing location of maintenance ports for removal of power core segments. Centerline dimensions are in meters.

The design challenges and activation requirements for the ARIES-ACT1 vacuum vessel primary structural material may be summarized as follows; a) generates only low level radioactive waste, preferably Class A to reduce disposal cost, b) generates low levels of decay heat to ensure the vessel's effectiveness as a heat sink during LOCA/LOFA events, c) develops a fracture–resistant microstructure with adequate strength and ductility during fabrication, d) maintains adequate fracture toughness, strength and uniform strain properties and creep resistance during the vessel lifetime of ~40 FPY, e) exhibits high-quality weld properties without the need for a well-controlled post-weld heat treatment (PWHT). These requirements are more stringent than those pertaining to current fission reactor containment vessels or to the ITER vacuum vessel and necessitate a fresh look at potential structural materials.

An assessment of potential candidate alloys based on activation characteristics and mechanical properties identified the 8-9% Cr RAFS, low- alloy ferritic steels (such as Type 430), Mn-substituted austenitic stainless steels and the 2-3%Cr bainitic steels. It was concluded that the greatest potential to meet these requirements resided in the new class of 3Cr-3WV bainitic steels. For the candidate steels to meet the requirements for classification as Class C low-level waste after 40 FPY of operation, they must meet the set of seventeen stringent impurity levels identified by Klueh et al [*Met.Trans.* ***28A*** *(1997) 335-345*]

based on careful chemical analysis of the lowest levels that have ever been achieved in large scale melting and fabrication processing of a variety of reduced activation and commercial steels. On this basis, the 3Cr-3WV bainitic steels were the only option which met the waste disposal criteria without presenting serious concerns regarding decay heat requirements. These steels easily meet the general strength requirements in terms of S_m, combined with excellent creep rupture properties in the 400-500^{o}C operating temperature range.

Materials in this class were studied by the US Fusion Materials Program during the 1990's as alternatives to the 8-9Cr RAFS for first wall and blanket applications. The subsequent realization of the potential applications for the 3Cr-3WVsteels within the petroleum and chemical processing industries subsequently motivated the development and the production of 50-ton heats of several 3Cr-WV alloys as higher strength replacements for the traditional 2¼ Cr- 1Mo steel (ASME T22). A significant outcome of this program was the approval of an ASME Code Case for one of the alloys, Grade 351, which contained 1.7 wt.% W and 0.7 wt.% Mo. Earlier work in Japan on W-substituted low Cr alloy steels such as HCM2S resulted in the development of a code-qualified bainitic steel T23 (2.25 %Cr-0.25Mo-1.6W) and its subsequent commercialization and large-scale deployment in the chemical processing industry. The Mo-free, low- activation 3Cr-3WV steel developed superior stress rupture properties compared to the commercial alloys T22 and T23 and even compared favorably with values of the 9Cr-1Mo ferritic-martensitic steel T91. Another important finding of these programs was that the thermodynamics and kinetics of the bainite transformation in both the low activation and conventional versions of the 3Cr bainitic alloys enable high toughness microstructures to develop in the weld zone and heat affected zone without the need for a post weld heat treatment.

In summary, the 3Cr-3WV class of bainitic steels represents a new class of low activation structural alloys with potential applications for fusion energy systems. The promising range of properties include, fabrication and tonnage-scale production by conventional metallurgical processing, good tensile strength, ductility and facture toughness, superior creep resistance and excellent welding behavior. Most importantly, with currently achievable levels of impurity control, they meet the requirements for Class C low-level waste while generating low decay heat. However, at present there is very little known regarding microstructural stability over projected plant lifetimes in the 400-500^{o}C range or of the response of these steels to moderate levels of radiation damage at any temperatures in a degraded 14 MeV fusion neutron spectrum typical for a vacuum vessel.

10.2 MATERIALS FOR THE STRUCTURAL RING AND DIVERTOR CARTRIDGE

The structural ring (SR) is a large helium–cooled double walled component measuring ~4 meters wide and ~10 m high and ~30 cm overall thickness, identified in the segment drawing shown in Fig. 49. Its primary functions are to secure the inboard and outboard blanket and divertor segments in position and to operate at a sufficiently high temperature to contribute heat to the power cycle. The current assumption is to operate with helium inlet and outlet temperatures of 650 and 680^{o}C respectively which would result in steel operating temperatures of 675- 700^{o}C. If necessary to ease materials requirements the operating temperature could be lowered to ~650^{o}C max. with a resulting loss of ~1% in the overall cycle efficiency.

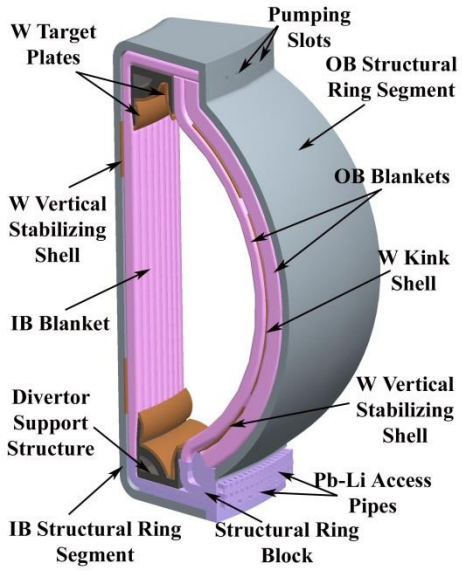

Figure 49. Power core segment for ARIES-ACT1 design showing location of structural ring relative to the blanket and divertor segments.

Although each segment of the SR is removed as an integral part of the power core for a blanket and divertor replacement every five years, it is anticipated that the SR, being in a lower flux region, could be re-used and only replaced once if necessary during the machine lifetime. Essentially it is regarded as a plant lifetime component.

The calculated neutron doses and helium generation levels in the SR are determined by the requirement for periodic segment replacement, requiring assembly gaps which tend to close partially during operation, so that neutron streaming through the gaps contributes to the overall neutron dose. For example, with an operating gap of 1cm between power core segments, the inboard section of the ring would sustain a 40 FPY lifetime dose of ~200 dpa combined with ~400 appm helium whereas for the outboard section these numbers are reduced to ~10 dpa and ~ 5 appm helium.

The requirement for prolonged operation at temperatures > 600^{o}C essentially eliminates the current set of reduced activation ferritic-martensitic (RAFM) steels F82H, EUROFER97, CLAM etc. so it is necessary to consider alternative structural alloys. In anticipation of the requirements for higher component operating temperatures in fusion energy systems beyond ITER, several international programs are pursuing the development of alternative materials such as ferritic-martensitic (FM) steels capable of operation in the range 600-650^{o}C and nano-structured steels capable of operating at temperatures up to 750-800^{o}C.

Driven by the needs of the fossil energy power generating industry to improve boiler efficiencies and to operate at increasingly higher water temperatures, global developments in the composition and microstructures of ferritic-martensitic steels coupled with advances in fabrication technologies have resulted in incremental improvements in high temperature operating capabilities. The current set of RAFMs for fusion applications are considered to be intermediate between the Gen1 and Gen2 materials. The possibility of applying the alloying principles embodied in the development of the Gen 3-4 alloys to the development of a comparable set of reduced activation alloys which could be manufactured via conventional processing technologies, has been discussed by R.L. Klueh [J. Nucl.Mater. 378 (2008) 159-

166] ,who outlined a developmental approach based on a reduced activation FM steel (9Cr-1.0W-0.25V-0.1Ta-0.10C) with systematic variations in B^{11} and N concentrations within specific ranges derived from an analysis of the compositions of the Gen4 FM steels. These ideas have been subsequently expanded with a focus on controlling microstructures by means of compositional adjustment guided by computational thermodynamics and optimization of thermo-mechanical treatments. Initial results (Chapter 4.0) have demonstrated that reduced activation alloys with tensile strength and high temperature creep properties exceeding those of the Gen3 alloys are attainable via this approach.

A second group of materials with attractive properties for SR applications are the oxide-dispersion-strengthened (ODS) alloys and the nano-structured ferritic alloys (NFAs) produced via mechanical alloying and consolidation by high temperature extrusion or HIPping. The incorporation of nano-scale oxide particles such as Y_2O_3 into the 9-11%Cr ferritic-martensitic steels leads to improved high temperature creep properties and a capacity for long–term operation at~650^{o}C. In the RAFMs the ferrite-austenite transformation can be manipulated during processing to improve both strength and fracture toughness properties. However the existence of the structural transformation limits the maximum temperature that could be sustained during a severe off-normal event (LOFA/LOCA) to ~800^{o}C.

Increasing the Cr concentration into the 12-14 wt.% range has led to the development of a revolutionary set of new alloys designated as nanostructured ferritic alloys (NFAs). Precise control of impurity pick-up during mechanical alloying and refinements to the mechanical alloying and consolidation processes have led to the development of a transformation-free ferrite matrix containing ultra-high concentrations of Y-Ti-O rich nano-features coupled with a nano -scale grain structure. This unique combination imparts high tensile and creep strengths, combined with good toughness, outstanding thermal stability and the potential to mitigate radiation effects phenomena, including the damaging effects of helium at high temperatures. These materials open up the possibility for components operating temperatures up to ~ 800^{o}C. Major impediments to the rapid development and deployment of these materials are the lack of manufacturing facilities capable of processing ~1000 kg quantities of mechanically–alloyed materials with sufficient homogeneity and reproducibility and the challenging issues related to the development of joining technologies.

For the divertor cartridge in the ARIE ACT-1 design, the helium inlet temperature needs to be ~700^{o}C to ensure that the bonded tungsten sections operate above ~800^{o}C to avoid radiation hardening-induced embrittlement of the tungsten. There is no surface heating in the cartridge and volumetric heating should be fairly uniform and therefore thermal stresses should be low. Given the low pressure drop in the jets (0.3 MPa) the pressure stresses in the cartridge are also expected to be very low.

Currently, the only credible reduced activation materials option for operation in the 700-800^{o}C regime is a nanostructured ferritic alloy such as 14YWT. The NFAs have outstanding high temperature strength and creep properties in this temperature range. Other important characteristics of the NFAs are a) the absence of a ferrite to austenite phase change thus ensuring that during off-normal temperature excursions >800^{o}C the alloy will remain in the ferrite phase field and b) the exceptional thermal stability of the dispersion of the nano-features. The only radiation effects issue is related to helium generation since all parts of the cartridge are operating well above the temperature range of radiation effects stemming from point defect generation, defect clustering and radiation-enhanced diffusion. The stress levels in the cartridge may be too low to trigger significant helium embrittlement phenomena related to stress-induced bubble growth. Increased Cr levels or alloying with Al are options for further alloy development if it becomes necessary to increase oxidation resistance, depending on helium impurity control.

For all of the ferritic-martensitic and ferritic structural materials, creep, creep rupture and microstructural stability phenomena are primarily driven by thermal effects at operating temperatures >600^{o}C. In this situation the most significant radiation effects phenomena will stem from the

accumulation of transmutation-induced helium and the possible effects of grain boundary helium bubbles on creep rupture life. This is a regime that has received very little attention from fusion materials programs and clearly there will be a need for detailed thermal/structural analysis of specific components and development of a greatly expanded data base on the effects of long-term service at high temperatures on microstructural stability and critical properties such as strength, ductility, fracture toughness, and also on the time –dependent properties such as creep and fatigue. Design of such an experimental program must be underpinned by microstructural modeling of the behavior of helium in the high temperature regime and its impact on fracture and on creep cavity formation.

11.0 IRRADIATION EXPERIMENTS

11.1 NEW RABBIT CAPSULES FOR HFIR IRRADAITION OF FUSION MATERIALS

J. McDuffee (mcduffeej@ornl.gov), N. Cetiner, R. Howard

SUMMARY

Four new series of rabbit capsules were designed and fabricated for HFIR irradiation of fusion materials in 2013, leading to a total of 41 capsules built for the program.

Tensile Creep Rabbits

A set of 20 rabbit capsules were designed in 2012 to apply a tensile stress on specimens during irradiation at temperature. Program test materials were F82H steel and SiC composites; specimens of V-4Cr4Ti and graphite were included to validate the techniques, based on the known irradiation creep of these meaterials. These rabbits were assembled and irradiated in 2013, although three of the capsules were not completed due to broken specimens or frames. A stainless steel bellows was placed inside each assembly and pressurized to provide the desired tensile load on the specimen located at the bottom of the stack. Each capsule also contains two unstressed reference specimens of the same material. Figure 50 shows the parts for one of the creep capsules and Figure 51 shows a partial assembly.

Figure 50. Parts for Tensile Creep Capsule T11-05J. The largest part, the sleeve, is about 10 mm diameter by 50 mm long. The specimen, in this case a SiC composite, is the hour glass shaped piece second from the bottom. It is flanked by two reference specimens that will be unloaded during irradiation.

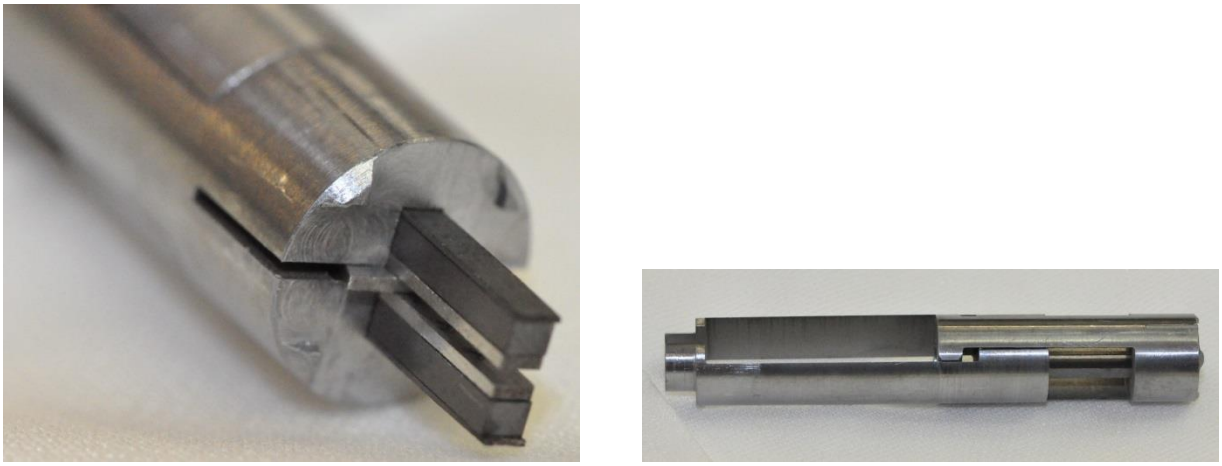

Figure 51. Partial Internal Assembly of a Tensile Creep Capsule.

After assembly, each bellows was individually pressurized to achieve the required specimen force and the bellows then sealed. The capsules were then placed in a load frame and the exposed bellows cap was pressed down until it unseated from the frame. The results from the J12-02 capsule are shown in Figure 52. The applied force on the specimen at ambient temperature is measured by projecting the unseated force line to zero.

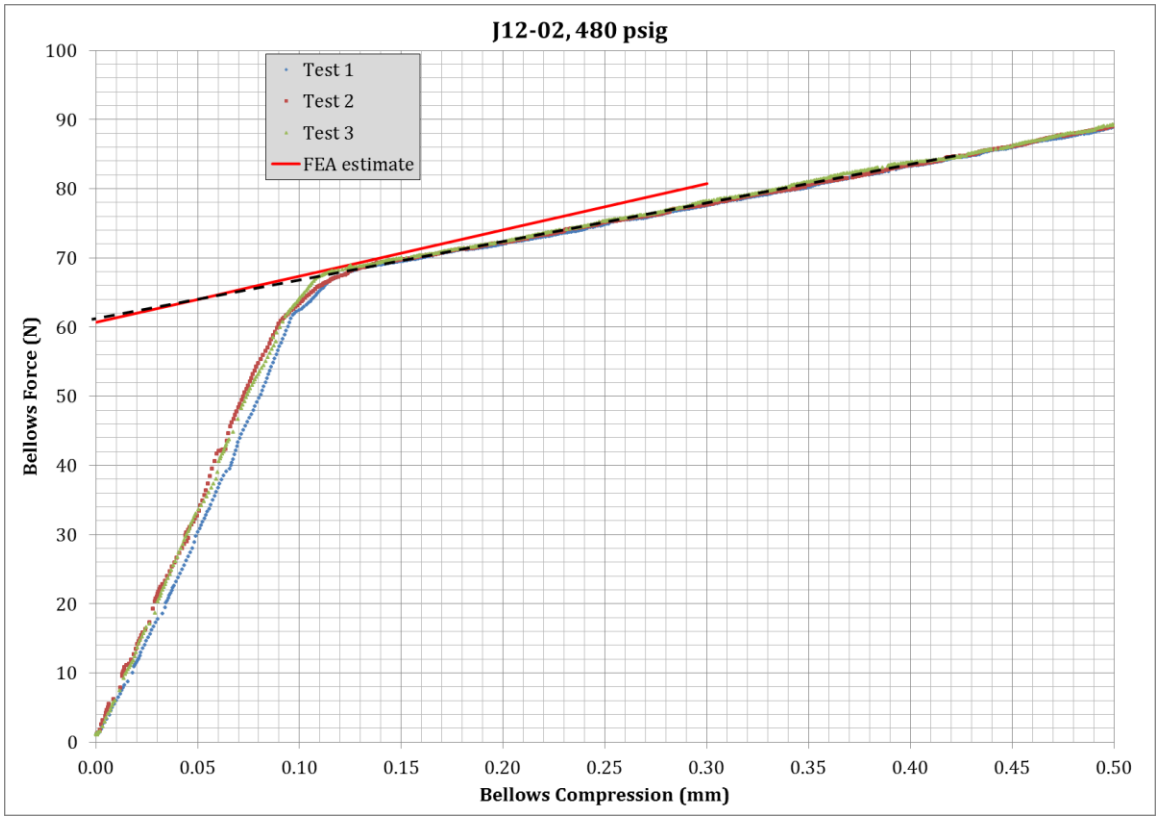

Figure 52. Post-assembly Bellows Force Measurement.

Compact Composite Flexure Experiments

The Compact Composite Flexure (CCF) experiments include SiC specimens for materials testing to be used for fusion applications. Eight rabbit capsules were designed to irradiate silicon carbide specimens in the flux trap of HFIR at 950±50°C. Each capsule contains 20 composite flexure specimens, 4 passive temperature monitors, and various other supporting parts (liners, springs etc.). The physical layout of the capsule and representative temperatures are shown in Fig. 53. Note that the capsule layout imposes 180° symmetry.

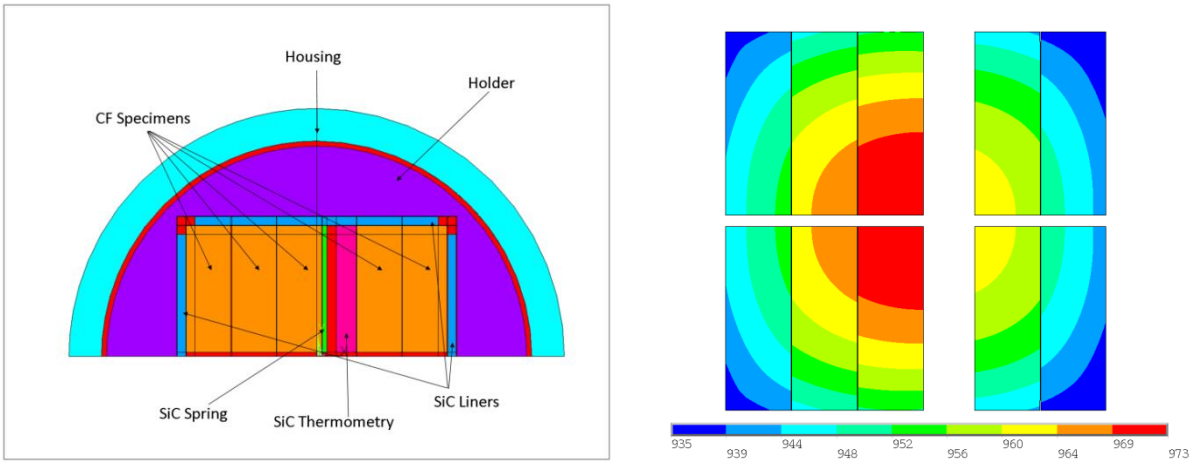

Figure 53. Schematic diagram of the capsule showing specimen loading configuration (left) and the calculated temperature distribution during irradiation (right), temperatures in °C. The outer diameter of the capsule is approximately 9 mm.

Mini-composite Rabbits

The Mini-Composite (MC) rabbit capsules are designed to irradiate SiC composite specimens in the flux trap of the HFIR. The experiment includes four similar capsules. The objective of these experiments is to examine the high-dose and high-temperature neutron irradiation effects on the SiC/SiC composite and the fiber/matrix (F/M) interface and microstructural change of the pyrolytic carbon (PyC) F/M interphase. The capsule design contains nine MC specimens, four high-resistivity Chemical Vapor Deposited Silicon Carbide (CVD-SiC) equi-biaxial flexure (BF) specimens, and two CVD-SiC thermometry (TM) specimens. These specimens are contained within molybdenum holders. Four SiC liners and several SiC springs are used to hold the parts in place and to help maintain good thermal contact. Design temperature was 950°C. Mini-composite specimens are fiber bundles with various diameters that vary between 1.0 and 2.0 mm. In consideration of the fragile structure of the bundles, the total number of the MC specimens is adjusted to fit the available space during fabrication. For the thermal analysis, it is assumed that there are five MC specimens and the available space is occupied by one solid piece with weighed density representing the specimens. Figures 54-56 show details of this capsule type.

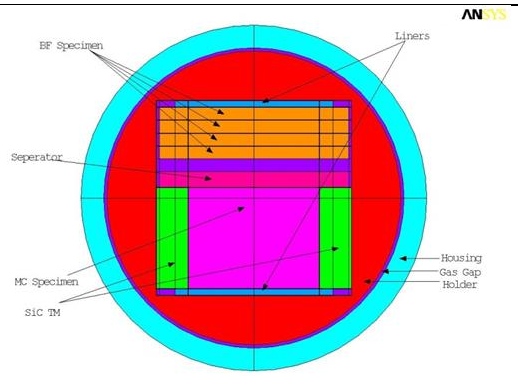

Figure 54. Component layout for the ~9 mm diameter MC Rabbit capsule.

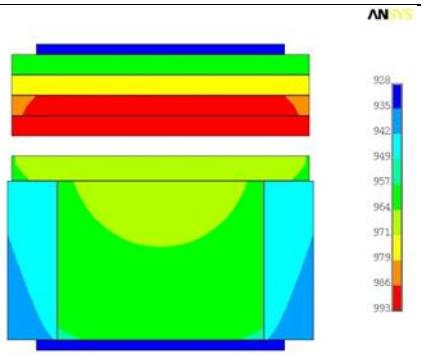

Figure 55. Contour temperature plot (ºC) for the specimens in JCR11-09 Rabbit.

Figure 56. Capsule Parts for the JCR11-12 Rabbit capsule.

MAX-PHASE Rabbits

Max-Phase Rabbit Irradiations are designed to use a total of 9 rabbit capsules to generate a set of data on fundamental irradiation effects for a unique class of emerging materials. Rabbits are designed for three different temperatures: 400, 700 and 1000°C. Planned irradiations will be to 2, 6, or 10 dpa. The specimens are of various shapes and the specimen materials are Ti_3SiC_2, Ti_2AlC, SiC and Si single crystal. Four of the 9 rabbit designs also include NITE type SiC specimens. Loading of a typical capsule is shown in Fig. 57. All these rabbit capsules started irradiation in HFIR cycle 449.

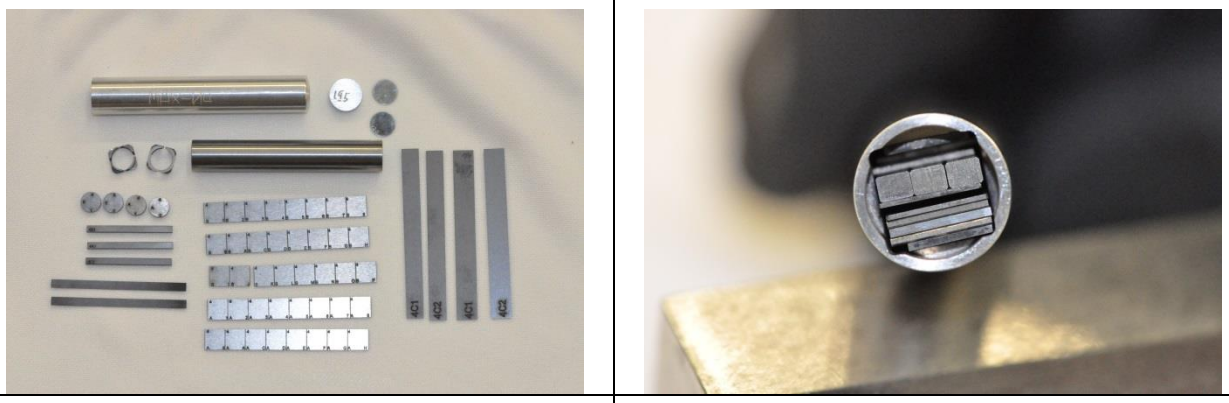

Figure 57. Specimen types (left) and end view of loaded specimen holder (right) for a MAX phase HFIR rabbit irradiation capsule. The diameter of the specimen holder is approximately 9 mm.

CONCLUSIONS

Four new rabbit capsule designs and 41 total rabbits were developed to support fusion materials irradiations in FY2013. This represents a significant accomplishment in design and fabrication, and these capsules occupied a large fraction of the available space in the HFIR flux trap during the year.

11.2 HFIR IRRADIATION PROGRAM

Y. Katoh (katohy@ornl.gov), M.A. Snead, J.L. McDuffee, C. Bryan

SUMMARY

Neutron irradiation experiments were performed in support of the research and development of fusion reactor materials using various materials irradiation facilities in the High Flux Isotope Reactor (HFIR).

During FY-2013, 4 full length target zone capsules and 49 target zone rabbit capsules completed HFIR irradiation, achieving the target neutron fluences. Those capsules are listed in Table 8 along with supplemental information regarding material, specimen type, temperature, fluence, and period of irradiation. At the end of FY-2013, 20 target zone rabbit capsules were continuing irradiation in HFIR toward their target neutron fluences. Those capsules are listed in Tables 9 and 10 along with the information on material and irradiation conditions.

Table 8. Fusion Materials Program capsules that completed HFIR irradiation in FY-2013.

Experiment Designation	Primary Materials	Specimen Types*	Irradiation Temperature (°C)	Max Exposure (dpa)	Number of Reactor Cycles	Irradiation Period From – To (month/year)		
Target zone full-length capsules (DOE-JAEA)								
JP-28	Steels	SSJ, FT	300,400,500	80	~50	4/05	–	7/13
JP-29	Steels	SSJ, FT	300,400,500	80	~50	1/05	–	7/13
JP-30	Steels	SSJ, FT	300,400,650	20	~10	11/11	–	8/13
JP-31	Steels	SSJ, FT	300,400,650	20	~10	11/11	–	8/13
Target zone rabbit capsules (TITAN)								
MTTN01	Steels	SSJ, MC	300	14	8	1/12	–	6/13
T9G-12	Steels, W	SSJ, MC	300	10	6	5/12	–	2/13
T9C-8	Steels, W	SSJ, MC	500	10	6	5/12	–	2/13
T9C-22	Steels, W	SSJ, MC	500	10	6	5/12	–	2/13
T9C-16	Steels, W	SSJ, MC	500	10	6	5/12	–	2/13
T9C-10	Steels, W	SSJ, MC	650	10	6	5/12	–	2/13
T9C-18	Steels, W	SSJ, MC	650	10	6	5/12	–	2/13
T9G-6	Steels, W	SSJ, MC	300	6	4	7/12	–	2/13
T9C-21	Steels, W	SSJ, MC	500	1.2	3	1/13	–	7/13
T9G-11	Steels, W	SSJ, MC	300	1.2	2	7/12	–	11/12
T9C-15	Steels, W	SSJ, MC	500	10	6	7/12	–	7/13
T9C-5	Steels, W	SSJ, MC	650	1.2	3	1/13	–	7/13
TB-300-4	Steels, W	SSJ, MC	300	6	5	7/12	–	6/13
TB-500-3	Steels, W	SSJ, MC	500	6	6	7/12	–	2/13
TB-650-3	Steels, W	SSJ, MC	650	6	5	7/12	–	6/13
TTN03	SiC	BSR	300	30	16	2/11	–	8/13
TTN05	SiC	BSR	500	30	15	5/11	–	8/13
TTN07	SiC	BSR	800	30	15	5/11	–	8/13
TTN18	SiC	BSR	500	30	13	8/11	–	8/13
TTN20	SiC	BSR	1200	10	5	3/12	–	11/12

Target zone rabbit capsules (DOE-JAEA)								
F8A1	Steels	SSJ, MC	300	50	29	2/09	–	7/13
F8A2	Steels	SSJ, MC		50	29	2/09	–	7/13
F8B1	Steels	SSJ, MC		50	29	2/09	–	7/13
F8B2	Steels	SSJ, MC		50	29	2/09	–	7/13
F11A3	Steels	SSJ, MC		20	11	5/11	–	2/13
F11A4	Steels	SSJ, MC		20	11	5/11	–	2/13
F11B3	Steels	SSJ, MC		20	11	5/11	–	2/13
JCR11-02	SiC	BB	950	10	6	10/12	–	8/13
JCR11-06	SiC	BB	950	10	5	10/12	–	7/13
Target zone rabbit capsules (DOE-JAEA-TITAN)								
T11-01J	V-Cr-Ti	T Creep	425	1.5	1	11/12	–	12/12
T11-02J	V-Cr-Ti	T Creep	425	4.5	3	1/13	–	7/13
T11-03J	V-Cr-Ti	T Creep	425	1.5	1	11/12	–	12/12
T11-04J	V-Cr-Ti	T Creep	425	4.5	3	1/13	–	7/13
T11-05J	SiC	T Creep	600	2	1	11/12	–	12/12
T11-06J	SiC	T Creep	600	6	3	1/13	–	7/13
T11-08J	SiC	T Creep	600	6	3	1/13	–	7/13
T11-09J	SiC	T Creep	600	2	1	11/12	–	12/12
T11-11J	SiC	T Creep	600	2	1	11/12	–	12/12
T11-13J	Graphite	T Creep	600	1.5	1	11/12	–	12/12
T11-14J	Graphite	T Creep	600	4.5	3	1/13	–	7/13
J12-01	Steels	T Creep	300	1.2	1	1/13	–	2/13
J12-02	Steels	T Creep	300	4.8	3	5/13	–	8/13
J12-03	Steels	T Creep	300	1.2	1	5/13	–	6/13
J12-04	Steels	T Creep	300	4.8	3	1/13	–	7/13
J12-05	Steels	T Creep	300	1.2	1	1/13	–	2/13
J12-06	Steels	T Creep	300	4.8	3	5/13	–	8/13
Target zone rabbit capsules (ORNL)								
MAX-01	Ti-Si-C	MC	400	2	1	7/13	–	8/13
MAX-04	Ti-Si-C	MC	700	2	1	7/13	–	8/13
MAX-07	Ti-Si-C	MC	1000	2	1	7/13	–	8/13

*T/SSJ = Tensile, MC = Multipurpose Coupon, BB = Bend Bar, BSR = Bend Stress Relaxation Creep. Some experiments also contain TEM disks, other special purpose specimens, and monitors occupying small spaces.

Table 9. HFIR Fusion Materials Program capsules that are continuing irradiation beyond FY-2013.

Experiment Designation	Primary Materials	Specimen Types*	Irradiation Temperature (°C)	Max Exposure (dpa)	Number of Reactor Cycles	Irradiation Period From – To (month/year)		
Target zone rabbit capsules (DOE-JAEA)								
JCR11-01	SiC	BB	950	50	25	11/12	–	
JCR11-03	SiC	BB	950	30	15	5/13	–	
JCR11-04	SiC	BB	950	30	15	5/13	–	
JCR11-05	SiC	BB	950	50	24	10/12	–	
JCR11-07	SiC	BB	950	100	50	10/12	–	
JCR11-08	SiC	BB	950	100	50	10/12	–	
JCR11-09	SiC	STC	950	4	3	6/13	–	11/13
JCR11-10	SiC	STC	950	10	8	6/13	–	2014
JCR11-11	SiC	STC	950	30	14	6/13	–	
JCR11-12	SiC	STC	950	100	50	6/13	–	
Target zone rabbit capsules (ORNL)								
T9G-13	Steels, W	SSJ, MC	300	12	9	7/12	–	1/14
T9C-24	Steels, W	SSJ, MC	650	12	8	7/12	–	11/13
PC5X	W	SSJ, MC	80/100	20	9	6/12	–	11/13
TB-650-4	Steels, W	SSJ, MC	650	20	11	7/12	–	2014
MAX-02	Ti-Si-C	MC	400	6	4	7/13	–	2014
MAX-03	Ti-Si-C	MC	400	10	6	7/13	–	2014
MAX-05	Ti-Si-C	MC	700	6	3	7/13	–	1/14
MAX-06	Ti-Si-C	MC	700	10	5	7/13	–	2014
MAX-08	Ti-Si-C	MC	1000	6	3	7/13	–	1/14
MAX-09	Ti-Si-C	MC	1000	10	5	7/13	–	2014

*T/SSJ = Tensile, MC = Multipurpose Coupon, BB = Bend Bar, STC = Single Tow Composite. Some experiments also contain TEM disks, other special purpose specimens, and monitors occupying small spaces.

Table 10: Additional HFIR Fusion Materials Program capsules that are continuing irradiation beyond FY-2013.

Experiment Designation	Primary Materials	Specimen Types[##]	Irradiation Temperature (°C)	Max Exposure (dpa)	Number of Reactor Cycles	Irradiation Period From – To (month/year)		
Target zone rabbit capsules (TITAN)								
MTTN01	Steels	T, MC	300	4.8	4	1/12	–	
300-HD-1	Steels	SSJ, MC	300	12	6	5/12	–	
500-HD-1	Steels	SSJ, MC	500	12	6	5/12	–	
500-HD-2	Steels	SSJ, MC	500	12	6	5/12	–	
500-HD-3	Steels	SSJ, MC	500	12	6	5/12	–	
650-HD-1	Steels	SSJ, MC	650	12	6	5/12	–	
650-HD-2	Steels	SSJ, MC	650	12	6	5/12	–	
300-MD-1	Steels, W	SSJ, MC	300	7	4	7/12	–	
500-LD-2	Steels, W	SSJ, MC	500	2	2	10/12	–	
300-LD-3	Steels, W	SSJ, MC	300	2	2	7/12	–	
300-HD-2	Steels, W	SSJ, MC	300	12	8	7/12	–	
500-HD-4	Steels, W	SSJ, MC	500	12	6	7/12	–	
650-LD-3	Steels, W	SSJ, MC	650	2	2	10/12	–	
650-HD-3	Steels, W	SSJ, MC	650	12	8	7/12	–	
PC5	Various	SSJ, MC	80/100	20	9	6/12	–	
TB-300-4	Steels, W	SSJ, MC	300	7	5	7/12	–	
TB-500-3	Steels, W	SSJ, MC	500	7	4	7/12	–	
TB-650-3	Steels, W	SSJ, MC	650	7	5	7/12	–	
TB-650-4	Steels, W	SSJ, MC	650	20	11	7/12	–	
TTN03	SiC	BSR	300	20	11	2/11	–	
TTN05	SiC	BSR	500	20	11	5/11	–	
TTN07	SiC	BSR	800	20	11	5/11	–	
TTN18	SiC	Fiber BSR	500	20	11	8/11	–	
TTN20	SiC	Fiber BSR	1200	10	6	3/12	–	

[##]T/SSJ = Tensile, FT = Fracture Toughness, MC = Multipurpose Coupon, BB = Bend Bar, BSR = Bend Stress Relaxation Creep. Most experiments also contain TEM disks, other special purpose specimens, and monitors occupying small spaces.

12.0 PUBLICATION RECORD

Papers Submitted:

"Principles and Practices of Irradiation Creep Experiment using Pressurized Mini-Bellows", *Thak Sang Byun, Meimei Li (ANL), Lance L. Snead, Yutai Katoh, Timothy D. Burchell, Joel L. McDuffee,* submitted to the Journal of Nuclear Materials.

"Multimodal Options for Materials Research to Advance the Basis for Fusion Energy in the ITER Era", *S.J. Zinkle, A. Möslang, T. Muroga and H. Tanigawa,* submitted to Nuclear Fusion.

"Retention of Hydrogen Isotopes in Neutron Irradiated Tungsten", *Y. Hatano, M. Shimada, Y. Oya, G. Cao, M. Kobayashi, M. Hara, B.J. Merrill, K. Okuno, M.A. Sokolov, Y. Katoh*, submitted to Materials Transactions.

"Deuterium Trapping at Defects Created with Neutron- and Ion-Irradiation in Tungsten", *Y. Hatano, M. Shimada, Y. Oya, V.K. Alimov, M. Hara, J. Shi, M. Kobayashi, T. Oda, G. Cao, K. Okuno, T. Tanaka, K. Sugiyama, J. Roth, B. Tyburska-Püschel, J. Dorner, N. Yoshida, N. Futagami, H. Watanabe, M. Sokolov, Y. Katoh,* submitted to Nuclear Fusion.

"Review of Silicon Carbide and Silicon Carbide Composites for Fusion Reactor Application", *T. Hinoki, Y. Katoh, L.L. Snead, H.C. Jung, K. Ozawa, H. Katsui, Z.H. Zhong, S. Kondo, Y.H. Park, C. Shih, C.M. Parish, R.A. Meisner, A. Hasegawa, C.H. Henager,* submitted to Materials Transactions.

"Novel Ceramics for Emerging Opportunities in Energy, Environment, and Transportation", *S.K. Sundaram, P. Colombo, and Y. Katoh,* submitted to International Journal of Applied Ceramic Technology, Invited.

"The Role of Microstructure on the Optical Performance of Neutron Irradiated Dielectric Mirrors",*K.J. Leonard, G.E. Jellison Jr., N.A.P.K. Kumar and L.L. Snead*, submitted to the Journal of Nuclear Materials.

"Stability of the strengthening nanoprecipitates in reduced activation ferritic steels under Fe^{2+} ion irradiation", *L. Tan, Y. Katoh, L.L. Snead,* submitted to the Journal of Nuclear Materials. (2013).

"Fusion Materials Irradiation Test Station (FMITS) at SNS", *ORNL Staff* Prepared in response to the FESAC Subcommittee on Future Facilities, (February 2013.)

Papers Published:

"The Influence of Transition Metal Solutes on the Dislocation Core Structure and Values of the Peierls Stress and Barrier in Tungsten", *G. D. Samolyuk, Y. N. Osetsky and R. E. Stoller,* J. Phys.: Condens. Matter 25 (2013) 025403

"Fusion Material Irradiation Test Facility (FMITS) at SNS", *M. Wendel, M. Dayton, W. Lu, T. McManamy, P. Rosenblad, R. E. Stoller,* Proc. IAEA Fusion Energy Conference, Paper FTP/P1-27, San Diego, USA, 8-13 October 2012.

"Multimodal Options for Materials Research to Advance the Basis for Fusion Energy in the ITER Era", *S.J. Zinkle, A. Möslang, T. Muroga and H. Tanigawa,* abridged 12 page manuscript as Paper OV/5-4 in Proc. IAEA Fusion Energy Conference, San Diego, CA, Oct. 8-13, 2012.

"Effects of alloying elements and thermomechanical treatment on 9Cr reduced activation ferritic-martensitic (RAFM) steels", *L. Tan, Y. Yang, J.T. Busby*, Journal of Nuclear Materials 442 (2013) S13-S17.

"Recent progress of R&D activities on reduced activation ferritic/martensitic steels", *Q. Huang, N. Baluc, Y. Dai, S. Jitsukawa, A. Kimura, J. Konys, R.J. Kurtz, R. Lindau, T. Muroga, G.R. Odette, B. Raj, R.E. Stoller, L. Tan, H. Tanigawa, A.-A.F. Tavassoli, T. Yamamoto, F. Wan, Y. Wu*, Journal of Nuclear Materials 442 (2013) S2-S8.

"Design Challenges and Activation Concerns for the ARIES Vacuum Vessel," *L.El-Guebaly, T. Huhn, A.F. Rowcliffe, S.Malang*, Fus.Sci.Tech. 64 93) (2013) 449-454

"On the Use of SRIM for Computing Radiation Damage Exposure," *R. E. Stoller, M. M. Toloczko, G. S. Was, A. G. Certain, S. Dwaraknath, and F. A. Garner,* Nuclear Instruments and Methods in Physics Research B 310 (2013) 75-80.

"Molecular Dynamics Simulation of Cascade-Induced Ballistic Helium Resolutioning from Bubbles in Iron," *R. E. Stoller,* Journal of Nuclear Materials 442 (2013) S674-S679.

"Irradiation Response in Weldment and HIP Joint of Reduced Activation Ferritic/Martensitic Steel, F82H," *T. Hirose, M. A. Sokolov, M. Ando, H. Tanigawa, K. Shiba, R. E. Stoller, G. R. Odette,* Journal of Nuclear Materials 442 (2013) S557-561.

"PIE at ORNL, Post Irradiation Examination Capabilities for Structural and Non-Fuel Materials at Oak Ridge National Laboratory", *J. P. Robertson,* ORNL/TM-2013/40, February 2013.

"Retention of Hydrogen Isotopes in Neutron Irradiated Tungsten,*" Hatano, Y., M. Shimada, Y. Oya, G. Cao, M. Kobayashi, M. Hara, B. J. Merrill, K. Okuno, M. A. Sokolov and Y. Katoh,* Materials Transactions 54(4): (2013)437-441.

"Silicon Carbide and Silicon Carbide Composites for Fusion Reactor Application," *Hinoki, T., Y. Katoh, L. L. Snead, H. C. Jung, K. Ozawa, H. Katsui, Z. H. Zhong, S. Kondo, Y. H. Park, C. Shih, C. M. Parish, R. A. Meisner, A. Hasegawa and C. H. Henager,* Materials Transactions 54(4): (2013) 472-476.

"The effect of neutron irradiation on the mechanical properties of C/SiC composites," *C. Shih, Y. Katoh, L. L. Snead and J. Steinbeck*, Journal of Nuclear Materials **439**(1): (2013) 192-201.

"Determination of Interfacial Mechanical Properties of Ceramic Composites by the Compression of Micro-pillar Test Specimens," *C. Shih, Y. Katoh, K. J. Leonard, H. Bei and E. Lara-Curzio*, Journal of Materials Science **48**(15): (2013) 5219-5224.

Talks Presented:

FMITS at SNS Design Study System Description, *M. W. Wendel*, SNS – JSNS Collaboration Meeting on Target Systems & Neutronics, Oak Ridge, TN, November, 2012

Mechanical Properties of Advanced Reduced Activation Ferritic-Martensitic Steels, (invited), *L. Tan , T.S. Byun, J.T. Busby, L.L. Snead*, NuMat 2012 – The Nuclear Materials Conference, Osaka, Japan, October 22-25, 2012.

Helium Bubbles in Iron: Stability, Equilibrium and Effect on Strengthening, *Yu. N. Osetskiy and R. E. Stoller*, at MRS, Boston, November 2012

A New Equation of State for Helium Based on Atomistic Simulations, *R. E. Stoller and Yu. N. Osetskiy*, at NuMat, Osaka, Japan, October 2012

Atomistic Aspects of Strengthening due to Nanoscale Obstacles in Irradiated Iron, *Yu. N. Osetskiy and R. E. Stoller*, at NuMat, Osaka, Japan, October 2012

Multimodal Options for Materials Research to Advance the Basis for Fusion Energy in the ITER Era (invited overview lecture), *S.J. Zinkle, A. Möslang, T. Muroga and H. Tanigawa,* IAEA Fusion Energy Conference, San Diego, CA, Oct. 8-13, 2012,

Impact of Materials on the Future of Nuclear Energy (invited), *S.J. Zinkle,* Birnbaum Memorial lecture, Materials Science & Engineering Department Colloquium, University of Illinois at Urbana-Champaign, Oct. 29, 2012.

Materials for Advanced Fission and Fusion Reactors (invited), *S.J. Zinkle,* Symposium on the Future of Nuclear Energy, Georgia Tech School of Nuclear Engineering 50th Anniversary Celebration, Nov. 1-2, 2012.

Pathways for Development of Advanced Materials for Nuclear Energy Systems (invited), *S.J. Zinkle, M.P. Brady, B.A. Pint, L.L. Snead, L. Tan, K.A. Terrani, Y. Yamamoto,* Symp. HH on Advances in Materials for Nuclear Energy, 2012 Materials Research Society Fall Meeting, Boston, MA, Nov. 26-30, 2012.

Opportunities and Challenges for Materials Innovation in Nuclear Energy (keynote invited lecture), *S.J. Zinkle,* Workshop on Materials Innovation for Nuclear Optimized Systems, CEA-Saclay, France, Dec. 5-7, 2012.

Research on Tritium/Heat Transfer and Irradiation Synergism for First Wall and Blanket in the TITAN Project, *T. Muroga, D.K. Sze, K. Okuno, T. Terai, A. Kimura, R.J. Kurtz, A. Sagara, R. Nygren, Y. Ueda, R.P. Doerner, B.J. Merrill, T. Kunugi, S. Smolentsev, Y. Hatano, M.A. Sokolov, T. Yamamoto, A. Hasegawa, Y. Katoh,* at: 24th IAEA Fusion Energy Conference, San Diego, October 2012.

Hydrogen Isotope Trapping at Defects Created with Neutron and Ion-Irradiation in Tungsten, *Y. Hatano, M. Shimada, Y. Oya, V.K. Alimov, M. Hara, J. Shi, T. Nozaki, M. Kobayashi, T. Oda, G. Cao, K. Okuno, T. Tanaka, N. Yoshida, N. Futagami, K. Sugiyama, J. Roth, B. Tyburska-Püschel, J. Dorner, I. Takagi, M. Hatakeyama, H. Kurishita, M. Sokolov, Y. Katoh,* at: 24th IAEA Fusion Energy Conference, San Diego, October 2012.

Research and Development Status of Reduced Activation Ferritic/Martensitic Steels Corresponding to DEMO Design Requirement, *H. Tanigawa, H. Tanigawa, M. Ando, S. Nogami, T. Hirose, D. Hamaguchi, T. Nakata, H. Sakasegawa, M. Enoeda, Y. Someya, H. Utoh, K. Tobita, K. Ochiai, C. Konno, R. Kasada, A. Möslang, E. Diegele, M.A. Sokolov, L.L. Snead, Y. Katoh, R.E. Stoller, S.J. Zinkle,* in: 24th IAEA Fusion Energy Conference, San Diego, October 2012.

Glass-Ceramics as Joining Materials for Nuclear Applications, *V. Casalegno, M. Ferraris, M. Salvo, S. Rizzo, A. Ventrella, D. Blagoeva, T. Hinoki, Y. Katoh,* at NuMat 2012 Nuclear Materials Conference, Osaka, October 2012.

Irradiation-Resistant Joining for Silicon Carbide Ceramics and Composites, *Y. Katoh, L.L. Snead, C. Shih, T. Hinoki, T. Koyanagi, M. Ferraris, C.H. Henager, Jr.,* at NuMat 2012 Nuclear Materials Conference, Osaka, October 2012.

Effect of Neutron Irradiation on Carbon Fiber Reinforced SiC Matrix Composite, *C. Shih and Y. Katoh,* American Nuclear Society 2012 Winter Meeting, San Diego, November 2012.

Design Concept for the FMITS facility. *M. Wendel,* SNS - JSNS (Japan Spallation Neutron Source) Collaboration Meeting on Neutron Source Development, Nov. 27-29, 2012.

Recent Progress in Development of Irradiation Tolerant Nanostructured Ferritic Alloys, *D.T. Hoelzer*, 6th GETMAT Technical Meeting at the Karlsruhe Institute of Technology, Karlsruhe, Germany, January 22-24, 2013.

Microstructures of heavily neutron-irradiated SiC/SiC composites, *Y. Katoh, A.G. Perez-Bergquist, K. Leonard, P. Dou, and L.L. Snead,* TMS 2013 Annual Meeting, San Antonio, TX, March 3-7, 2013.

Radiation Stability of Silicon Carbide Joints Made by Various Bonding Methods, *Y. Katoh, T. Hinoki, (Kyoto University), M. Ferraris, (Politecnico di Torino), C. H. Henager, (PNNL),* 37th International Conference and Exposition on Advanced Ceramics and Composites, Daytona Beach, Florida, January 27-February 1, 2013.

C. Shih, Y. Katoh, J. Steinbeck, (Physical Sciences Inc.) "Dimensional changes and flexural behavior of neutron irradiated 2D carbon fiber reinforced SiC matrix composite"

K. Ozawa, T. Nozawa, H. Tanigawa, (JAEA), Y. Katoh, L. L. Snead, "Tensile and Interfacial Properties of Unidirectional Advanced SiC/SiC Minicomposites"

Cascade Defect Evolution: Comparison of Kinetic Monte Carlo Methods, *Roger E. Stoller*, 2013 IEA Fusion Modeling Workshop, Sede Ciudad de Alicante, Universidad de Alicante, Spain, May 16-18, 2013.

Hardening Mechanisms Due to Radiation Induced Obstacles in Iron and Ferritic, Alloys: An Atomic-Scale View, *Yuri Osetsky*, 2013 IEA Fusion Modeling Workshop, Sede Ciudad de Alicante, Universidad de Alicante, Spain, May 16-18, 2013.

A New Atomistic-based Equation of State for Helium in Iron, *Roger E. Stoller*, 2013 IEA Fusion Modeling Workshop, Sede Ciudad de Alicante, Universidad de Alicante, Spain, May 16-18, 2013.

Use of dpa and recommendations for using SRIM to compute dpa, *R. E. Stoller*, OECD Nuclear Energy Agency Workshop and 9th Meeting of the Working Party on Multiscale Modelling of Materials, NEA HQ, Issy-les-Moulineaux, France,May 13-15, 2013.

Facility for high heat flux testing of irradiated fusion materials and components using infrared plasma arc lamps, *A.S. Sabau, E.K. Ohriner, J. Kiggans, D.C. Harper, L.L. Snead,* 14th International Conference on Plasma-Facing Materials and Components for Fusion Applications, Forschungszentrum Juelich, Germany,May 13-17, 2013.

The Role of Microstructure on the Optical Performance of Neutron Irradiated Dielectric Mirrors, *K.J. Leonard, G.E. Jellison Jr., N.A.P.K. Kumar, L.L. Snead,* 17h International Conference on Radiation Effects in Insulators, University of Helsinki, Finland, June 30 through July 5, 2013.

Development and Evaluation of Joining Methods for Silicon Carbide for Nuclear Applications, *Y. Katoh, L.L. Snead, T. Cheng, J. Kiggans, C. Shih, M. Ferraris, A. Ventrella, T. Hinoki, T. Koyanagi, C.H. Henager, Jr., R.J. Shinavski,*10th Pacific Rim Conference on Ceramics and Glass Technology, San Diego, CA, June 2-6, 2013.

Investigation of Interfacial Mechanical Properties of Ceramic Composites with Micro-pillar Samples, *C. Shih, Y. Katoh, K.J. Leonard, H. Bei, E. Lara-Curzion,* 10th Pacific Rim Conference on Ceramics and Glass Technology, San Diego, CA, June 2-6, 2013.

Development and Progress in SiC Composite Integration Technology for Fusion Energy, *Y. Katoh, L.L. Snead, C.H. Henager, Jr., T. Hinoki, M. Ferraris,* 25th Symposium on Fusion Engineering, San Francisco, CA, June 10-13, 2013.